



TECHNISCHE
UNIVERSITÄT
WIEN
Vienna | Austria

DISSERTATION

**Distribution of Zinc and other Trace Elements in
Pathological Human Bone and in Histological Transition
Zones - An Approach with Micro and Nano Resolution
Elemental Imaging by Synchrotron XRF**

ausgeführt zum Zwecke der Erlangung des akademischen Grades einer
Doktorin der technischen Wissenschaften

unter der Leitung von
Ao.Univ.Prof. Dipl.-Ing. Dr.techn. Christina Strelt
E141 - Atominstitut

eingereicht an der Technischen Universität Wien
Fakultät für Physik

von
Dipl.-Ing. Mirjam Rauwolf, BSc.

Matrikelnummer: 0626259
Schönburgstraße 33, 1040 Wien

Ort, Datum

M. Rauwolf

Kurzfassung

Um geeignete Messanordnungen für synchrotronstrahlungsinduzierte (SR) Röntgenfluoreszenzanalyse (XRF) von Spurenelementen in Knochen zu finden, wurden, im Rahmen dieser Dissertationsschrift, unterschiedliche Messaufbauten getestet. Es zeigte sich, dass für Messungen mit einer Auflösung im Bereich von etwa 15 μm ein konfokaler Aufbau (FLUO Beamline, ANKA) besser geeignet ist als eine Vollbildanordnung (BAMline, BESSY II). Für Auflösungen unterhalb von einem Mikrometer erwies sich der XRF-Aufbau an der B16 Bending Magnet Test Beamline an der Diamond Synchrotronstrahlungsquelle als eine gute Wahl.

Im Rahmen dieser Arbeit wurden drei unterschiedliche Knochenprobensets gemessen. In den Proben von Patienten mit einem Osteosarkom, einem primär bösartigen Knochentumor, wurden im mineralisierten Tumorgewebe höhere Zinkwerte als im umliegenden, gesunden, mineralisierten Gewebe festgestellt.

Bei Untersuchungen von aus kalzifizieren und nicht kalzifizieren Gelenkknorpel bestehenden Proben konnten in der dünnen Grenzlinie zwischen den beiden Gebieten (der sogenannten Tidemark) erhöhte Zink- und Bleiwerte festgestellt werden. Diese Grenzlinie war für Zink 3 bis 11 μm und für Blei 3,5 bis 14,5 μm dick.

In Proben von Patienten mit Osteomalazie, einer unzureichende Mineralisierung der Knochensubstanz, schienen sich die Zink- und Strontiumwerte klar von denen der gesunden Kontrollproben zu unterscheiden. Jedoch konnte kein eindeutiger Trend festgestellt werden.

Abstract

In the scope of this thesis, different synchrotron radiation (SR) induced X-ray fluorescence (XRF) setups were tested to find suitable arrangements for the detection of trace elements in bone. It was shown that a confocal SR- μ XRF (FLUO beamline, ANKA) is preferable to detect trace elements in the tens of micrometer range compared to a full-field setup (BAMline, BESSY II). For sub-micrometer resolution, the XRF setup at the B16 bending magnet test beamline at the Diamond light source proved to be a good fit.

Three different bone sample sets were analyzed during the course of this work.

In the samples of patients with osteosarcoma, a primary malignant bone tumor, a higher Zn content was discovered in the mineralized tumor compared to the adjacent healthy mineralized bone tissue.

The investigation of thin samples containing non-calcified and calcified articular cartilage with a sub-micrometer resolution showed higher Zn and Pb content in thin structure interjacent those two tissues, the tidemark region. The thickness of the found tidemarks ranged from about 3 to 11 μm for Zn and 3.5 to 14.5 μm for Pb. In samples from patients with osteomalacia, a condition defined by inadequate bone mineralization, the Zn and Sr levels appeared to be different compared to the Zn and Sr content in the also measured healthy controls. However, no clear trend was identified.

Only work directly related to this thesis is listed here. For a complete list of publications and conference contributions produced during the pursuit of my PhD, see the end of this thesis.

Parts of this work have been published in the following peer-reviewed publications:

1. **M. Rauwolf**, A. Turyanskaya, D. Ingerle, N. Szoboszlai, I. Pape, A.W. Mandain, O.J.L. Fox, L. Hahn, K.J.S. Sawhney and C. Streli: *Characterization of a submicro-XRF setup on the B16 beamline at the Diamond Light Source*, J. Synchrotron Rad. 25, 2018, doi: 10.1107/S1600577518006203
2. **M. Rauwolf**, A. Turyanskaya, A. Roschger, J. Prost, R. Simon, O. Scharf, M. Radtke, T. Schoonjans, A. Guilherme Buzanich, K. Klaushofer, P. Wobrauschek, J. G. Hofstaetter, P. Roschger and C. Streli: *Synchrotron radiation micro X-ray fluorescence spectroscopy of thin structures in bone samples: comparison of confocal and color X-ray camera setups*, J. Synchrotron Rad., 24, 2017, p. 307-311, doi: 10.1107/S1600577516017057
3. **M. Rauwolf**, B. Pemmer, A. Roschger, A. Turyanskaya, S. Smolek, A. Maderitsch, P. Hischenhuber, M. Foelser, R. Simon, S. Lang, S.E. Puchner, R. Windhager, K. Klaushofer, P. Wobrauschek, J.G. Hofstaetter, P. Roschger and C. Streli: *Increased zinc accumulation in mineralized osteosarcoma tissue measured by confocal synchrotron radiation micro X-ray fluorescence analysis*, X-ray Spectrometry, 46(1), 2017, p. 56-62, doi: 10.1002/xrs.2727

Conference contributions related to parts of this work have been presented:

Talks:

1. **M. Rauwolf**, B. Pemmer, A. Roschger, A. Turyanskaya, S. Smolek, A. Maderitsch, P. Hischenhuber, R. Simon, S. Lang, S. E. Puchner, R. Windhager, K. Klaushofer, J. G. Hofstaetter, P. Roschger and C. Streli: *Synchrotron Radiation Micro XRF Analysis of Zinc in Osteosarcoma Tissue*, Jahrestagung

FG Nuklearchemie, GDCh Scientific Forum Chemistry 2017, Berlin, Germany, 2017, **invited** talk.

2. **M. Rauwolf**, A. Turyanskaya, A. Roschger, I. Pape, K. Sawhney, P. Wobrauschek, P. Roschger, J.G. Hofstaetter and C. Streli: *Zinc (Zn) and Lead (Pb) Accumulation in the Tidemark of Articular Cartilage with High-resolution micro-XRF*, 66th Annual Denver X-ray Conference 2017, Big Sky, USA, 2017, talk.
3. C. Streli, **M. Rauwolf**, A. Turyanskaya, B. Pemmer, D. Ingerle, P. Roschger, A. Roschger, J. Hofstätter and N. Szoboszlai: *Hard X-ray Spectroscopy of Biological Material using Synchrotron Radiation*, NESY winterschool (2017), Altaussee, Austria, **invited** talk.
4. **M. Rauwolf**, B. Pemmer, A. Roschger, A. Turyanskaya, S. Smolek, A. Maderitsch, P. Hischenhuber, R. Simon, S. Lang, S. E. Puchner, R. Windhager, K. Klaushofer, J. G. Hofstaetter, P. Roschger and C. Streli: *Synchrotron radiation micro XRF analysis of zinc in osteosarcoma tissue*, 26th Seminar Activation Analysis and Gamma Spectroscopy, Vienna, Austria, 2017, talk.
5. P. Wobrauschek, **M. Rauwolf**, A. Turyanskaya, J. Prost and C. Streli: *X-ray spectrometry with Synchrotron radiation*, Symposium: "Future Possible Use of Neutron and Synchrotron Sources by the Austrian User Community", Graz, Austria, 2016, talk.
6. **M. Rauwolf**, B. Pemmer, A. Roschger, A. Turyanskaya, S. Smolek, A. Maderitsch, P. Hischenhuber, C. Weixelbaumer, M. Foelser, R. Simon, S. Lang, S. E. Puchner, R. Windhager, K. Klaushofer, J. G. Hofstaetter, P. Roschger and C. Streli: *Zinc accumulation in mineralized osteosarcoma tissue determined with confocal SR- μ XRF*, European Conference on X-ray Spectrometry (EXRS2016), Gothenburg, Sweden, 2016, talk.
7. **M. Rauwolf**, B. Pemmer, A. Roschger, A. Turyanskaya, R. Simon, R. Windhager, K. Klaushofer, J. G. Hofstaetter, P. Roschger and C. Streli: *Distribution of Zinc in human high-grade osteosarcoma and healthy tissue determined with confocal synchrotron radiation micro X-ray Fluorescence analysis*, International

Conference on Progress in Bone and Mineral Research 2015 and the Annual Autumn Conference of the Austrian Society for Bone and Mineral Research, Vienna, Austria, 2015, talk.

8. C. Streli, P. Wobrauschek, D. Ingerle, J. Prost, **M. Rauwolf** and A. Turyanskaya: *Synchrotron Radiation Induced X-ray spectrometry - special techniques and applications*, IAEA Technical Meeting on Developments in Instrumentation and Novel Techniques for X-Ray Spectrometry Applications (F1-TM-47480), IAEA Head Quarter, Vienna, 2015, **invited** talk.
9. B. Pemmer, S. Smolek, C. Weixelbaumer, M. Fölser, **M. Rauwolf**, A. Maderitsch, P. Wobrauschek, C. Streli, A. Roschger, P. Roschger, K. Klaushofer, R. Simon, R. Windhager, S. Lang and J. Hofstätter: *Differential accumulation of S, Ca, Fe and Zn in human osteosarcoma tissue*, ICXOM 2013, Hamburg, Germany, 2013, talk.
10. B. Pemmer, S. Smolek, C. Weixelbaumer, M. Fölser, **M. Rauwolf**, A. Maderitsch, P. Wobrauschek, C. Streli, A. Roschger, P. Roschger, K. Klaushofer, R. Simon, R. Windhager, S. Lang and J. Hofstätter: *Distribution of S, Ca, Fe And Zn in Human Osteosarcoma Tissue Determined with Synchrotron and Laboratory μ XRF Analysis*, 8th European NESY Winter-School, Planneralp, Austria, 2013, talk.

Posters:

1. **M. Rauwolf**, A. Turyanskaya, D. Ingerle, N. Szoboszlai, I. Pape, A. W. Malandain, O.J.L. Fox, L. Hahn, K. Sawhney, and C. Streli: *The submicro-X-ray fluorescence setup on the B16 beamline at Diamond Light Source*, 67th Annual Denver X-ray Conference 2018, Westminster, Colorado, USA, 2018.
2. **M. Rauwolf**, A. Turyanskaya, A. Roschger, I. Pape, K. Sawhney, P. Wobrauschek, P. Roschger, J.G Hofstaetter, and C. Streli: *Micro-XRF analysis of zinc and lead accumulation in the tidemark of articular cartilage*, European Conference on X-Ray Spectrometry, Ljubljana, Slovenia, 2018.
3. **M. Rauwolf**, A. Turyanskaya, A. Roschger, P. Wobrauschek, P. Roschger, J. G. Hofstaetter and C. Streli: *Novel Clustering Approach for the Segmenta-*

tion of Elemental Distributions in Human Bone, 66th Annual Denver X-ray Conference 2017, Big Sky, USA, 2017.

4. **M. Rauwolf**, B. Pemmer, A. Roschger, A. Turyanskaya, S. Smolek, A. Maderitsch, P. Hischenhuber, M. Foelser, R. Simon, S. Lang, S. E. Puchner, R. Windhager, K. Klaushofer, J. G. Hofstaetter, P. Roschger and C. Streli: *Confocal SR- μ XRF measurements of increased Zinc accumulation in mineralized osteosarcoma*, 66th Yearly Meeting of the Austrian Physical Society, Vienna, Austria, 2016.
5. **M. Rauwolf**, A. Turyanskaya, A. Roschger, J. Prost, R. Simon, I. Pape, M. Radtke, O. Scharf, T. Schoonjans, A. Guilherme Buzanich, K. Sawhney, P. Wobrauschek, P. Roschger, J.G. Hofstaetter and C. Streli: *Zinc distribution in human bone: SR-micro X-ray fluorescence imaging of osteoporotic samples*, X-Ray Microscopy Conference (XRM2016), Oxford, UK, 2016.
6. **M. Rauwolf**, B. Pemmer, A. Roschger, A. Turyanskaya, R. Simon, R. Windhager, K. Klaushofer, J. G. Hofstaetter, P. Roschger and C. Streli: *Increased Zinc accumulation in mineralized osteosarcoma tissue measured by SR- μ XRF analysis*, 65th Annual Denver X-ray Conference 2016, Chicago, USA, 2016.
7. **M. Rauwolf**, A. Turyanskaya, A. Roschger, B. Pemmer, J. Prost, R. Simon, I. Pape, K. Klaushofer, P. Wobrauschek, P. Roschger, J.G. Hofstaetter and C. Streli: *Zn distribution in healing osteoporotic fractures measured by SR- μ XRF analysis*, 65th Annual Denver X-ray Conference 2016, Chicago, USA, 2016.
8. **M. Rauwolf**, A. Turyanskaya, A. Roschger, B. Pemmer, J. Prost, R. Simon, I. Pape, K. Sawhney, P. Wobrauschek, P. Roschger, J.G. Hofstaetter and C. Streli: *SR- μ XRF analysis of the zinc distribution in healing osteoporotic fractures*, European Conference on X-ray Spectrometry (EXRS2016), Gothenburg, Sweden, 2016.
9. **M. Rauwolf**, B. Pemmer, A. Roschger, A. Turyanskaya, R. Simon, R. Windhager, K. Klaushofer, J. G. Hofstaetter, P. Roschger and C. Streli: *Increased Zinc accumulation in mineralized osteosarcoma tissue*, 43rd Annual European Calcified Tissue Society Congress, Rom, Italy, 2016.

-
10. **M. Rauwolf**, A. Turyanskaya, A. Roschger, B. Pemmer, J. Prost, R. Simon, M. Radtke, T. Schoonjans, O. Scharf, A. Guilherme, P. Roschger, J.G. Hofstaetter, R. Windhager, K. Klaushofer, P. Wobrauschek and C. Streli: *SR- μ XRF of bone samples - a comparison of a confocal and a CXC setup*, 64th Annual Denver X-Ray Conference 2015, Westminster, USA, 2015.
 11. B. Pemmer, S. Smolek, C. Weixelbaumer, M. Fölser, **M. Rauwolf**, A. Maderitsch, P. Wobrauschek, C. Streli, A. Roschger, P. Roschger, K. Klaushofer, R. Simon, R. Windhager, S. Lang and J. Hofstätter: *Distribution of S, Ca, Fe and Zn in human osteosarcoma tissue determined with synchrotron and laboratory μ -XRF Analysis*, 62nd Annual Denver X-Ray Conference 2013, Westminster, CO, USA, 2013.

Acknowledgments

I would like to express my sincere gratitude to Dr. Christina Streli, my thesis supervisor, for all of the opportunities I was given to conduct my research, her patient guidance and encouragement.

I would like to thank my fellow labmate Anna Turyanskaya, with whom I spent numerous days and nights working on various beamlines. Working side by side with her pushed me to achieve greater accomplishments.

I would like to thank Peter Wobrauschek and the whole X-ray group of the Atominsti-tut for the interesting discussions and for all the fun and cake we had in the last years.

I would also like to extend my thanks to my cooperation partners – Jochen Hofstätter and Paul Roschger for discussion of the data and critical review of the publications.

Many thanks to Rolf Simon (ANKA), Ana Guilherme Buzanich, Martin Ratke and Ivo Zizak (all BESSY-II) as well as Ian Pape (Diamond) for their support during beamtimes.

Last but not the least, I want to express my gratitude to my partner Clemens and my family for providing me with unfailing support and continuous encouragement throughout my years of study and through the process of researching and writing this thesis. This accomplishment would not have been possible without them. Thank you.

The research leading to these results has received funding from the Austrian Science Fund (FWF, project number: P27715).

Contents

Kurzfassung	I
Abstract	II
Acknowledgments	VIII
1 Motivation	1
2 X-ray Fluorescence Analysis	3
2.1 X-ray Sources	3
2.1.1 Synchrotron radiation	4
2.2 Energy Dispersive X-ray Detectors	14
2.2.1 Si(Li) detector	14
2.2.2 SDD	15
2.2.3 Energy dispersive pnCCD detector	16
2.3 X-ray Optics	17
2.3.1 Multilayer monochromator	18
2.3.2 Kirkpatrick-Baez mirrors	18
2.3.3 Polycapillary	18
2.4 Sources of possible errors	20
2.4.1 Detector artefacts	21
2.4.2 Spectrum fitting	21
2.4.3 Information depth	22
3 Beamlines and experimental setups	24
3.1 SR-XRF	24
3.1.1 Confocal SR- μ XRF	24
3.1.2 Full-field SR- μ XRF	27

3.1.3	SR-submicro XRF	29
4	Quantitative backscattered electron imaging (qBEI)	33
5	Comparison of a confocal and a CXC setup	35
5.1	Materials and methods	35
5.1.1	Samples	35
5.1.2	SR- μ XRF	36
5.2	Results	37
5.3	Conclusion	41
6	Characterization of a submicro-XRF setup on the B16 beamline	42
6.1	Scanned Samples – Results	45
6.1.1	Gold test structure	45
6.1.2	Human bone biopsy sample	46
6.1.3	Cancer Cell	48
6.2	Conclusion	50
7	Zinc and other trace elements in mineralized osteosarcoma and healthy tissue	51
7.1	Materials and methods	52
7.1.1	Patients	52
7.1.2	Sample preparation	52
7.1.3	Micro XRF measurements	54
7.1.4	qBEI	55
7.1.5	Data evaluation	55
7.1.6	Statistical analysis	57
7.2	Results	58
7.2.1	Zinc	58
7.2.2	Iron and Strontium	65
7.3	Discussion	68
7.4	Conclusion	70

8	Trace elements in the tidemark	71
8.1	Materials and methods	71
8.1.1	Patients	71
8.1.2	Submicro XRF measurements	72
8.2	Data evaluation	74
8.2.1	Identifying the tidemark	74
8.2.2	Kaplan-Meier Estimation	77
8.3	Results	79
8.4	Conclusion	85
9	Trace elements in bone tissue of patients with diagnosed osteomalacia	86
9.1	Materials and methods	86
9.1.1	Patients	86
9.1.2	Micro XRF measurements	87
9.2	Data evaluation	87
9.3	Results	88
9.4	Discussion and Outlook	97
10	Concluding remarks and Outlook	98
10.1	Outlook	99
	Bibliography	100
	Curriculum Vitæ	113
	Publications	115
	Conference contributions	117

1 Motivation

The influence of many trace elements on human tissue is insufficiently understood. While some trace elements are essential to human health, there is also a growing body of literature on their role in the development of numerous diseases.

Studies on different minor and trace elements in various cancer types – breast cancer, prostatic carcinoma – reported significant changes in the levels of these elements in cancer tissue [1, 2]. However, very little is known about trace element levels and distributions in mineralized bone tissue, cartilage and bone tumor.

The element of the most interest in the scope of this thesis was zinc (Zn). Twenty-eight percent of the total body zinc are stored in the bone [3]. Although the influence of Zn on bone metabolism is still unknown it seems to have a stimulatory effect on bone formation [4]. Animal studies have shown that dietary zinc deficiency results in growth retardation as well as abnormal bone formation [5, 6]. Positive effects of zinc on skeletal strength were shown on growing rats [7].

Urinary zinc excretion of osteoporotic postmenopausal women was reported to be significantly higher than for non-osteoporotic postmenopausal women, while the plasma zinc levels did not differ between those groups [8]. A recent paper [9] linked an increase in Zn, in the chondrocytes cells of the cartilage, with the activation of a cartilage degrading enzyme and osteoarthritis.

The other trace elements this thesis focuses on are lead (Pb) and strontium (Sr). Ninety-four percent of the Pb body burden in adults is stored in bone (over 70% is in dense bone) [10]. A study on rats has shown that a Pb treatment significantly decreases body mass as well as the density of dry mass of bones [11]. Pb is considered as a potential risk factor in osteoarthritis [12] and osteoporosis [13, 14].

As Sr is chemically similar to Ca (both are from the second group of the periodic table), it can be found in the mineralized bone matrix as it is able to replace Ca. Sr is said to promote bone formation and inhibits bone absorption [15].

Bone is a heterogeneous material, which is constantly remodeling. On a macro-scale level it consists of a harder outer layer, the cortical bone, and a softer inner structure, the trabecular bone. The cortical bone is composed of osteons, cylindrical compact bone structures of about 200 μm in diameter that surround a haversian canal. Osteons are separated by the so-called cement lines (thickness in the micrometer range). The trabecular bone tissue is porous and made of thin rods and plates of bone, the trabeculae.

As bone consists of different micro-structures, a space-resolved measurement technique is needed. Considering that human bone samples are hard to get, a non-destructive method is strongly preferred. Synchrotron radiation induced X-ray fluorescence analysis (see section 3.1) allows for non-destructive analysis of elemental distribution in the micrometer and sub-micrometer range. It is therefore uniquely qualified to investigate trace elements in bone samples.

2 X-ray Fluorescence Analysis

X-ray Fluorescence Analysis (XRF) is a method for qualitative and quantitative determination of chemical elements in samples. For this technique, a sample is irradiated by a primary X-ray beam. The atoms in the sample are excited via the photoeffect and will emit X-ray fluorescence radiation and Auger electrons. Due to correlation between energy (or wavelength) and atomic number, it is possible to determine the elemental composition of the sample by measuring the spectrum of its emitted characteristic X-rays.

As the intensity of the fluorescence radiation is proportional to the concentration it is possible to quantify the elemental content of samples (under certain conditions). Although, XRF is usually a non-destructive analytic method the irradiation can sometimes lead to short-term or even permanent radiation damage.

The technique needs no or hardly any sample preparation. Elements from sodium to uranium can be easily analyzed. With some adaption of the setup (addition of a vacuum chamber and detector with an ultra-thin window) the range can be extended to the light elements down to carbon.

The measurement of an X-ray spectrum can be done either via the wavelength (wavelength dispersive XRF) or the energy (energy dispersive XRF). Only energy dispersive X-ray fluorescence analysis (EDXRF) methods were used in the scope of this thesis.

2.1 X-ray Sources

For X-ray analytical measurements four different types of X-ray sources are usually used:

- X-ray tubes
- Radio isotopes

- Synchrotron radiation
- Free electron laser

They differ from each other in the spectral distribution of the emitted radiation and in the brilliance (number of photons). A comparison of the brilliance of various X-ray sources can be seen in Fig. 2.1.

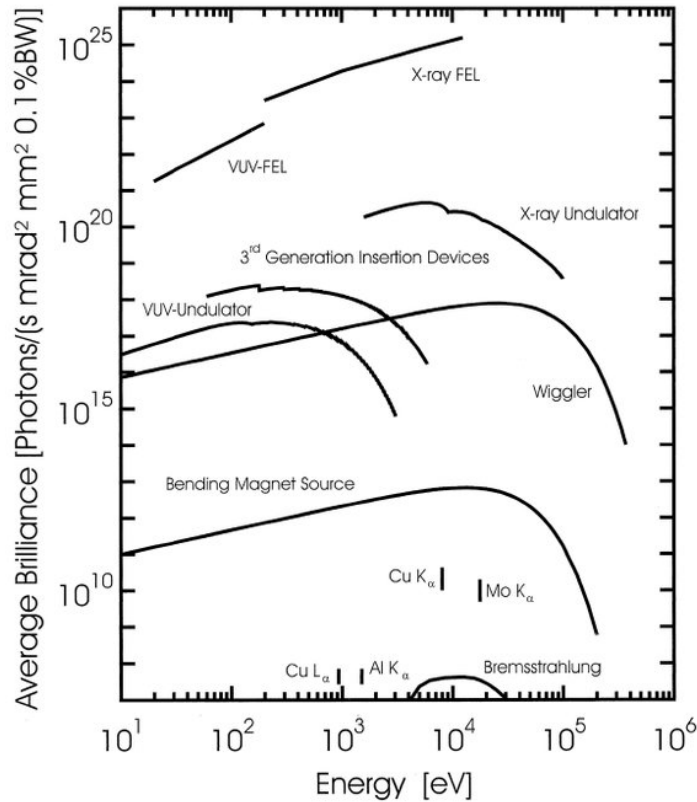


Figure 2.1: Comparison of the average brilliance of different X-ray sources. Image from [16].

Within the framework of this thesis, synchrotron radiation (see section 2.1.1) was the only X-ray source used.

2.1.1 Synchrotron radiation

The electromagnetic radiation which is emitted tangential to the direction of motion of a charged particle moving with relativistic velocity which is forced from its straight

path is called synchrotron radiation. It is produced in storage rings (a type of circular particle accelerator) where a continuous or pulsed beam of charged particles (usually electrons or positrons with a kinetic energy in the gigaelectronvolt (GeV) range) is kept in orbit for hours.

As a first step, the free electrons are generated by an electron gun. Those electrons are accelerated by a linear accelerator (LINAC). After leaving the LINAC, a booster synchrotron (or sometimes multiple) will collect the electrons (to reach the desired ring current) and bring them to their final energy (of several GeV). Afterwards, the electrons are transferred to the storage ring (injection), where they will be kept on a circular orbit and at a constant energy for a longer period of time. Due to the interaction of the electrons with the residual gas the ring current constantly decreases. When the current gets too low, the electron beam is dumped and the storage ring will be refilled. For example, at the ANKA light source the ring is injected twice a day. As the ring current is constantly changing, all measured data needs to be corrected for the ring current.

Newer storage rings such as Diamond light source and Bessy-II are operated slightly differently in the so-called top-up mode. Instead of dumping a decreasing beam and restarting the filling process, those storage rings are constantly refilled (topped up) with electrons. For measurements performed in the top-up mode, data usually does not need to be corrected for the ring current decrease.

To force electrons on a circular orbit and to produce synchrotron radiation, electromagnets the so-called **bending magnets**, which create a magnetic dipole field, are used. As the electron beam loses energy due to the synchrotron radiation, there is a constant need to replace this energy. This is done by adding straight sections with **radio frequency (RF) cavities** into the storage ring. To focus and stabilize the electron beam **quadruple and sextupole magnets** (magnetic lenses) are used.

The properties of synchrotron radiation are:

- small radiation source size
- high collimation (angular divergence of the beam in mrad range)

- wide wavelength range (energies from eV to several hundred of keV)
- high flux
- well defined time structure
- high level of polarization (linear in the orbit plane and elliptical or circular polarization above and below the orbit plane)
- the emitted spectrum is fully calculable (can be used as standard source for the calibration of detectors and other radiation sources)

Synchrotron radiation sources are characterized by the following parameters.

- The **intensity** $I(\mathbf{E})$ is the number of photons produced per second.

$$I = \frac{\text{photons}}{s} \quad (2.1)$$

- The number of photons per time and 0.1% energy bandwidth is called **spectral flux** $\phi(\mathbf{E})$. This unit takes the spectral "purity" into account.

$$\phi(E) = \frac{I(E)}{0.1\% \text{ energy bandwidth}} = \frac{\text{photons}}{s \cdot 0.1\% \cdot \frac{\Delta E}{E}} \quad (2.2)$$

- The **brightness** $\phi(\mathbf{E}, \psi, \theta)$ is defined as spectral flux per divergence (in both angular directions ψ and θ) of the photons.

$$\phi(E, \psi, \theta) = \frac{\phi(E)}{\text{beam divergence}} = \frac{\text{photons}}{s \cdot 0.1\% \cdot \frac{\Delta E}{E} \cdot \text{mrad}^2} \quad (2.3)$$

- A common unit to compare different sources is the **brilliance** $\phi(\mathbf{E}, \psi, \theta, \mathbf{x}, \mathbf{z})$ which in addition to all the parameters considered in the brightness also includes the size of the source (x and z are the horizontal and vertical coordinates of the source).

$$\phi(E, \psi, \theta, x, z) = \frac{\phi(E, \psi, \theta)}{\text{source size}} = \frac{\text{photons}}{s \cdot 0.1\% \cdot \frac{\Delta E}{E} \cdot \text{mrad}^2 \cdot \text{mm}^2} \quad (2.4)$$

Radiated power

According to classical electrodynamics, charged particles emit electromagnetic radiation when they are accelerated. The power per unit angle irradiated from such a particle (or charge) at momentum change $\frac{dp}{dt}$ can be given as

$$\frac{dP}{d\Omega} = \frac{e^2 \left| \frac{dp}{dt} \right|^2 \sin^2 \theta}{16 \cdot \pi^2 m_0^2 \epsilon_0 c^3} \quad (2.5)$$

where e is the charge of the particle, θ is the angle between the direction of acceleration and the direction of the emitted radiation, ϵ_0 is the vacuum permittivity and m_0 is the rest mass of the particle. This gives the classical torus shape angular distribution as shown in Fig. 2.2. The intensity is zero along the acceleration direction and reaches a maximum in the direction perpendicular to it.

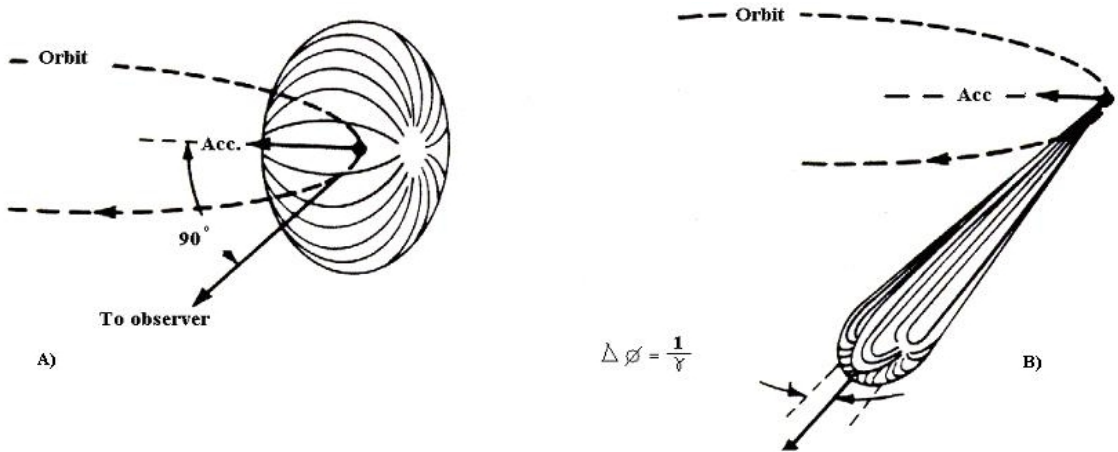


Figure 2.2: Radiation pattern of the accelerated particle moving at non-relativistic (on the left) and a relativistic speed (on the right). Image from [17].

By integrating over the full solid angle, the total power emitted from an accelerating charge can be written as

$$P = \frac{e^2 \left| \frac{dp}{dt} \right|^2}{6 \cdot \pi m_0^2 \epsilon_0 c^3} \quad (2.6)$$

However, the expression in equation 2.6 does not consider the time dilation and therefore underestimates the total power.

$$dt = \gamma \cdot d\tau \quad \text{with} \quad \gamma = \frac{1}{\sqrt{1 - \frac{v^2}{c^2}}} = \frac{E}{m_0 c^2} \quad (2.7)$$

As the time intervals in the lab system (dt) correspond to much smaller time intervals ($d\tau$) in the particle system, equation 2.6 changes to

$$P = \frac{e^2 \left| \frac{dp}{dt} \right|^2 \cdot \gamma^2}{6 \cdot \pi m_0^2 \epsilon_0 c^3} \quad (2.8)$$

For high energies the rest energy can be neglected.

$$E = \sqrt{(pc)^2 + (m_0 c^2)^2} \approx pc \quad (2.9)$$

The centripetal force on an object moving at tangential speed v along a path with radius of R is

$$F = \frac{dp}{dt} = \frac{mv^2}{R} = \frac{pv}{R} \approx \frac{Ev}{Rc} \quad (2.10)$$

By inserting equation 2.10 in equation 2.8 and assuming that $v \approx c$ we get the following expression for the radiated power

$$P \approx \frac{e^2 \cdot \gamma^2}{6 \cdot \pi m_0^2 \epsilon_0 c^3} \left| \frac{Ev}{Rc} \right|^2 \approx \frac{e^2 \cdot \gamma^2}{6 \cdot \pi \epsilon_0 \cdot R^2} \cdot \frac{E^2}{m_0^2 c^3} \approx \frac{e^2 \cdot \gamma^4 c}{6 \cdot \pi \epsilon_0 \cdot R^2} \quad (2.11)$$

Equation 2.11 shows that the radiated power is proportional to the fourth power of the particle energy (compared to the energy square in the classical case).

As the power is defined as

$$P = \frac{\Delta E}{\Delta t} \quad (2.12)$$

As the particle needs the time $\Delta t = \frac{2\pi R}{c}$ to travel once around its circular path with a speed of c , energy ΔE for one orbit is

$$\Delta E = P \cdot \Delta t = \frac{P(E, R) \cdot 2\pi R}{c} \approx \frac{e^2 \cdot \gamma^4}{3\epsilon_0 \cdot R} \quad (2.13)$$

For electrons (with $m_0c^2 = 0.511MeV$) this can be written in convenient units as

$$\Delta E[MeV] = 0.0885 \cdot \frac{E^4[GeV]}{R[m]} \quad (2.14)$$

The average power emitted by a storage ring, with a beam current I , is therefore

$$P[kW] = 0.0885 \cdot \frac{E^4[GeV]}{R[m]} \cdot I[mA] \quad (2.15)$$

Angular distribution

The angular dependence of the X-ray intensity from an accelerating charge is given by equation 2.5. This distribution must be transformed from the rest frame of the electron to the lab system (see Fig 2.2 on the right). As one can see, the distribution shows that almost all radiation is emitted in a narrow cone in the forward direction. In the special case where a photon is emitted perpendicular to the direction of the electron, the electron is moving in the x-direction with speed $v \approx c$, sending out radiation in the y-direction with the velocity $u'_y = c$. Considering the Lorentz transformation provides the velocities in the lab system:

$$u_x = \frac{u'_x + v}{1 + \frac{vu'_x}{c^2}} = v \approx c \quad (2.16)$$

$$u_y = \frac{1}{\gamma} \frac{1}{1 + \frac{vu'_x}{c^2}} \cdot u'_y = \frac{c}{\gamma} \quad (2.17)$$

Using the Taylor series, the angle of the radiation in the lab system can be given as

$$\theta \approx \frac{u_y}{u_x} \approx \frac{1}{\gamma} \quad (2.18)$$

This means all radiation with forward components will be folded into a cone with this maximum angle.

Energy distribution

A stationary observer sees from a single circling electron per revolution only a short light spot (sweeping searchlight). The observer starts to detect photons when the electron is at position A and will stop detecting photons when the electron passes

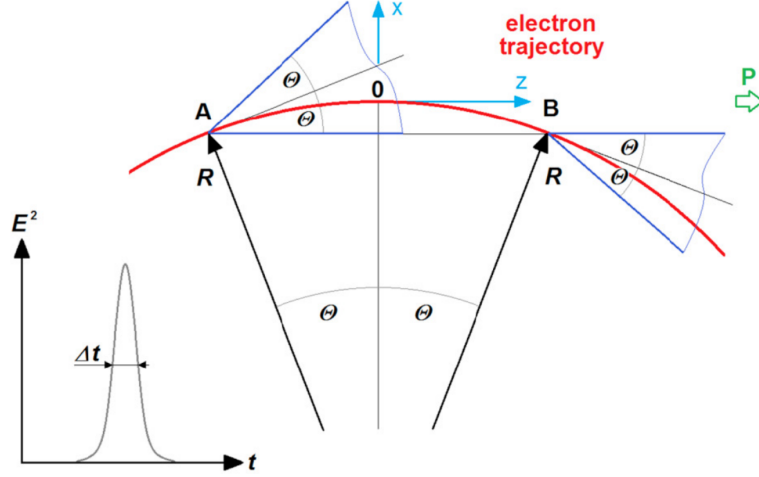


Figure 2.3: The difference between the time of flight of the photon and the single electron. Image from [18].

position B (see Fig 2.3.). The length of this time interval is given as the difference between the time of flight of the photon and the electron both traveling from A to B. Using the following approximations $\theta \approx \frac{1}{\gamma}$ and $\sin \theta \approx \theta - \frac{\theta^3}{3!} + \dots$, the time interval can be written as

$$\Delta t = t_e - t_p = \frac{2R\theta}{v} - \frac{2R \sin \theta}{c} = \frac{2R\theta}{\beta c} - \frac{2R \sin \theta}{c} \approx \frac{2R}{\gamma \beta c} \left(1 - \beta + \frac{\beta}{6\gamma^2}\right) \quad (2.19)$$

As $\frac{1}{(1+\beta)} \approx \frac{1}{2}$ for $\beta \approx 1$, γ^2 can be expressed as

$$\gamma^2 = \frac{1}{1 - \beta^2} = \frac{1}{(1 - \beta) \cdot (1 + \beta)} \approx \frac{1}{2(1 - \beta)} \quad (2.20)$$

With $(1 - \beta) \approx \frac{1}{2\gamma^2}$ the time interval can be expressed as

$$\Delta t \approx \frac{2R}{\gamma \beta c} \left(\frac{1}{2\gamma^2} + \frac{\beta}{6\gamma^2}\right) \approx \frac{4R}{3\gamma^3 c} \quad (2.21)$$

Using Heisenberg's uncertainty principle $\Delta E \cdot \Delta t \geq \frac{\hbar}{2}$ and the expression for the Lorentz force $\frac{\gamma m_0 v^2}{R} = evB$ (again using that $v \approx c$) one can express the energy spread related to the magnetic field:

$$\Delta E \geq \frac{3e\hbar B \gamma^2}{8m_0} \quad (2.22)$$

An exact expression for the intensity distribution over photon energies and emission angle involving Bessel functions can be derived. An important parameter is the critical energy E_c . At this energy, the spectrum is divided into two parts of the equal power (see Fig. 2.4).

$$E_c = \frac{3e\hbar B\gamma^2}{2m_0} \quad \text{or} \quad E_c[\text{keV}] = 0.665 E^2[\text{GeV}] B[\text{T}] \quad (2.23)$$

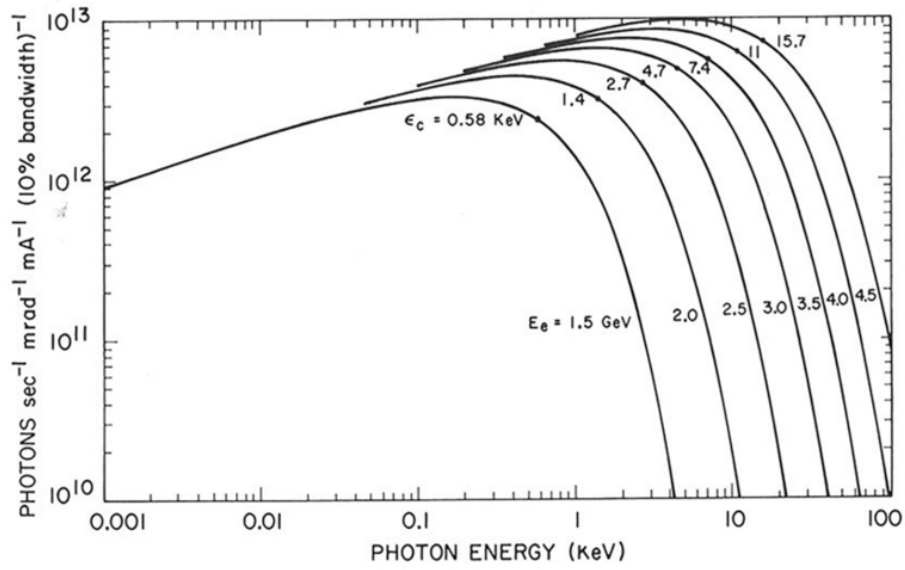


Figure 2.4: Spectral distribution of synchrotron radiation as a function of the value of critical energy (ϵ_c) of the storage ring. Image from [19].

Insertion Devices

Newer generations of synchrotron light sources have additional straight sections with alternating magnetic structures (the so-called insertion devices) to modify the spectral distribution of the synchrotron radiation.

Wavelength shifters are used to shift the spectral distribution to higher photon energies (and shorter wavelengths). Such devices consist of three superconducting dipole magnets with alternating field directions. The central magnet has the high

field and is used as the radiation source. While the other two are needed to compensate the beam deflection from the central pole (see Fig. 2.5).

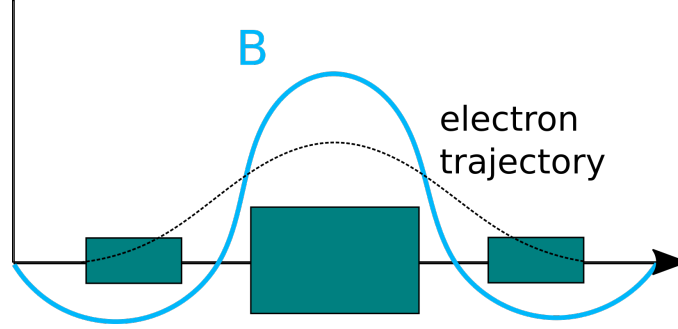


Figure 2.5: Magnet field distribution for a wavelength shifter

A **Wiggler** consists of an array of N equal dipole magnets with alternating field directions and two end poles. The end poles have a different magnetic field to make the total wiggler neutral to the beam path. Compared to the single bending magnet, each of the poles produces a fan of radiation in forward direction. The photons superimpose incoherently resulting in a continuous spectrum and a total photon flux which is N times higher than for a bending magnet.

The important quantity to characterize Wigglers (as well as Undulators) is the parameter K :

$$K = \frac{eB_0\lambda_u}{2\pi mc} = 0.934 \cdot B_0[T] \cdot \lambda_u[cm] \quad (2.24)$$

It contains the period length λ_u , the length after which the magnetic field reaches its initial value. The parameter K describes the strength of the deflection of the electrons. If K is known the maximal deflection angle of the produced beam can be expressed as $\frac{K}{\gamma}$. For a wiggler K is always greater than 1.

An **Undulator** (see Fig. 2.6) has a very similar structure to the one of a Wiggler. The biggest difference is that the magnetic field of each of the single poles is smaller than for the poles in the wiggler. This leads to a smaller deflection of the electrons and a smaller opening angle of the produced radiation. And this in turn leads to a coherent superimposition of all radiation lobes and a spectrum with sharp peaks of higher brilliance. The parameter K for an Undulator is always less than or equal to 1 ($K \leq 1$).

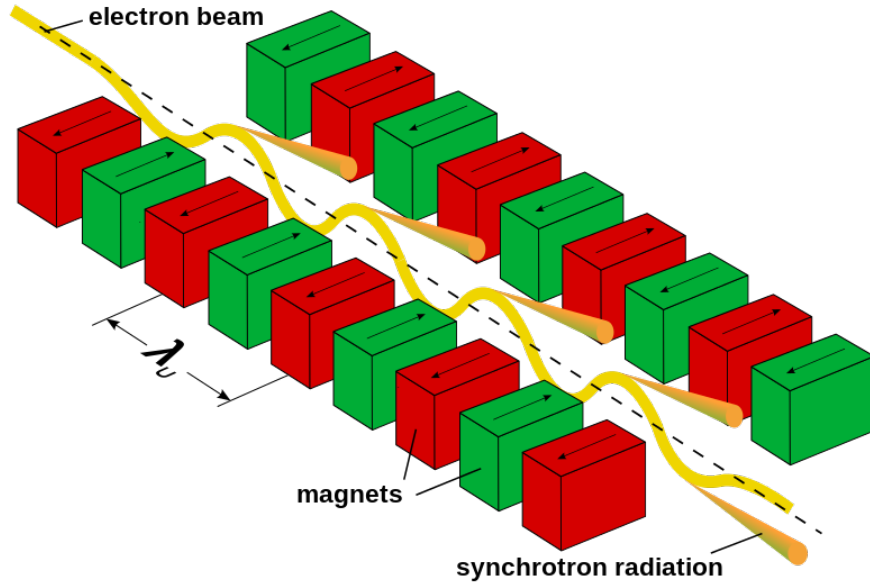


Figure 2.6: Schematic sketch of the working principle of a Wiggler or Undulator.
Image from [20]

The discrete wavelength of the sharp peaks in the Undulator spectrum can be given by:

$$\lambda = \frac{\lambda_u}{2j\gamma^2} \left(1 + \frac{K^2}{2} + \gamma^2 \theta^2 \right) \quad \text{with} \quad j = 1, 2, 3, \dots \quad (2.25)$$

with θ being the angle between the z-axis and the direction of observation.

A comparison of the brilliance over the photon energy for bending magnets, wigglers and undulators can be seen in Fig. 2.7.

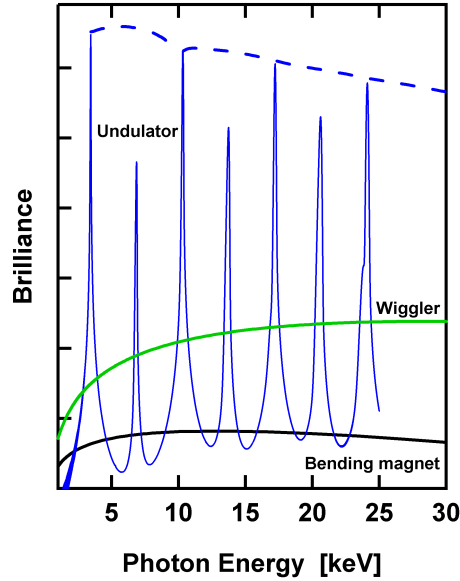


Figure 2.7: Comparison of the spectra of bending magnets, wigglers and undulators.
Image from [21]

2.2 Energy Dispersive X-ray Detectors

For EDXRF analysis, the energies of the X-ray radiation are measured with semiconductor detectors. The most common types of semiconductor detectors or EDXRF are: lithium drifted silicon detectors (Si(Li) detectors), silicon drift detectors (SDD) as well as energy dispersive pnCCD detectors.

2.2.1 Si(Li) detector

The base of an Si(Li) detector is PIN diode which is a diode with an undoped intrinsic, radiation sensitive region between the p-doped (with elements of the third main group - extra holes) and the n-doped (with elements of the fifth main group - extra electrons) region. This PIN structure can be created from a p-doped silicon (Si) crystal by diffusing lithium (Li) atoms into it. By applying high voltage to this crystal a big intrinsic depletion zone is formed. On the backside of this region, a domain with higher Li content (n-doped) is created. The p-doped region is the remaining, not Li compensated, crystal.

The n-side of the PIN diode is coated with about 20 nm gold. On the p-side a metal

layer (often also gold) and the p-doped region form the so-called Schottky barrier contact. High voltage is applied between the two contacts (see Fig. 2.8). In the

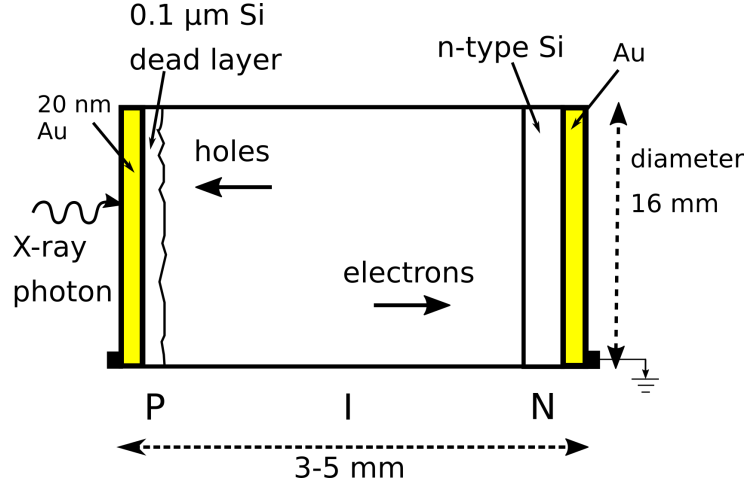


Figure 2.8: Schematic sketch of a Si(Li) detector

intrinsic region an X-ray photon produces electron-hole pairs. The amount of the electron-hole pairs is proportional to the energy of the X-ray photon. An energy of 3.7 eV is needed to produce one electron-hole pair.

To reach the intrinsic region photons need to get through the gold contact and the uncompensated p-region (Si dead layer). This limits the detection of low photon energies as they might be absorbed before they reach the radiation sensitive region of the detector.

Photons interacting in the dead layer will be measured with a low pulse height, leading to a peak distortion at the low energy side due to incomplete charge collection. This effect is called low energy tailing.

To reduce dark current and the noise of the pre-amplifier, the detector is cooled with liquid nitrogen (about 77K).

2.2.2 SDD

The SDD is based on a PSN diode with a weakly doped region (S) between the p- and n-doped region. It is made from a Si wafer and has a thickness of about 450 μm and a large area contact on the entrance side facing the incoming X-rays. On the opposite side there is a number of concentric drift electrodes. In the center

of these rings the collecting anode is placed. By applying a negative bias voltage the disc is fully depleted. The p-doped rings are used to create a cone-shaped, gradient, electric field which drifts the electrons, to the anode.

Advantages of an SDD are the smaller design and cheaper operation costs (cooling

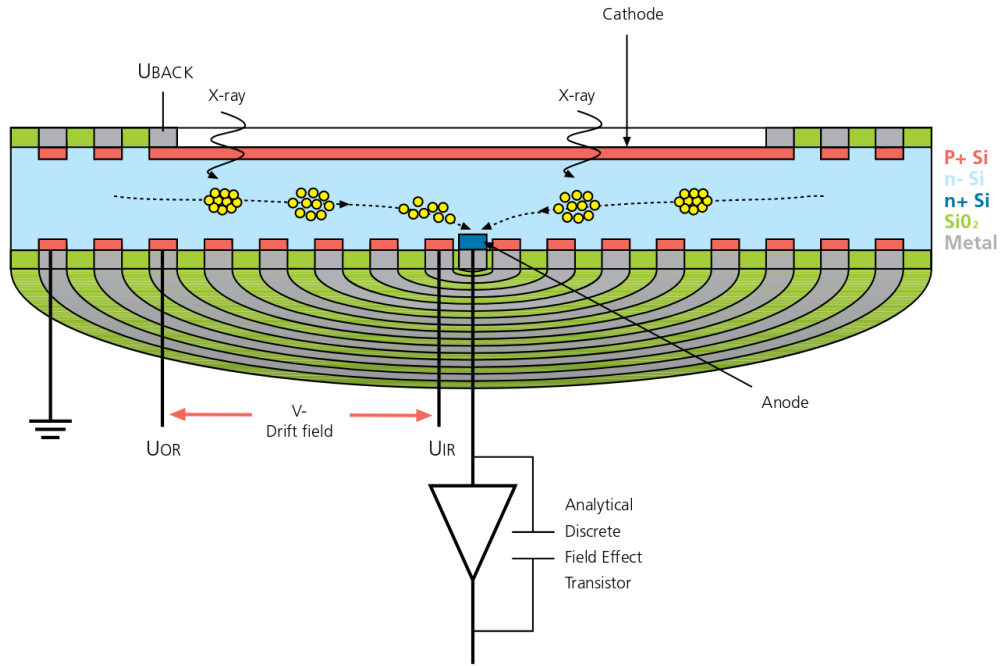


Figure 2.9: Schematic sketch of an SDD. Image from [22]

by Peltier element instead of liquid nitrogen). It can process higher count rates due to the drift field. As its anode is a lot smaller than the anode of the Si(Li) detector the SDD has very low capacitance and therefore also less noise and a better energy resolution.

The SDD is a lot thinner than the Si(Li) detector, therefore it has a worse efficiency for higher photon energies.

2.2.3 Energy dispersive pnCCD detector

A pnCCD detector is an energy dispersive array detector for X-rays. In combination with an X-ray optic such as a pin hole or a polycapillary half lens this type of detector samples in full-field mode (which means it is recorded like a photograph instead of measured pixel by pixel).

Similar to the SDD, the pnCCD is produced from a 450 μm thick fully depleted Si chip. It is implanted with of highly doped p-structures on both sides of a Si

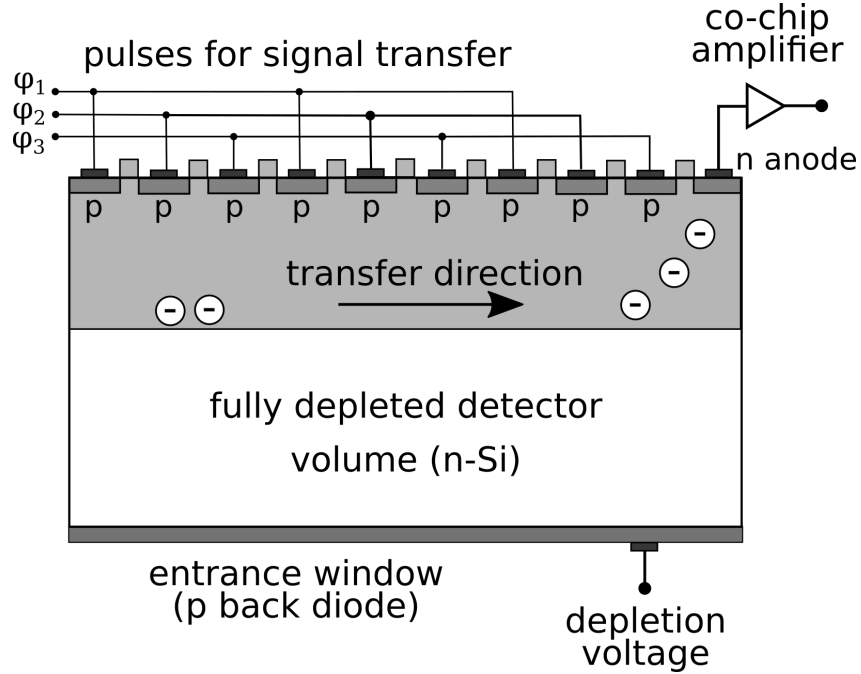


Figure 2.10: Schematic sketch of an pnCCD. Image modeled after [23]

n-substrate (see Fig. 2.10). By applying a voltage, depletion over the whole detector volume can be achieved. The entrance side of the detector consists of a homogeneous thin p-implant. An X-ray photon creates electron-hole pairs in the radiation sensitive volume. Electrons are collected in the potential minima of the single pixels. During read-out, electrons are transported to the neighboring pixel in their CCD line. The last pixel in each line transfers the charges to an amplifier.

2.3 X-ray Optics

The X-ray optics can be used to manipulate either the X-ray spectrum or to focus the X-ray beam. In the scope of this thesis, multilayer structures were used to monochromatize the exciting beams. For focusing the X-ray beams, polycapillary lenses and Kirkpatrick-Baez mirrors were used. A short description of those three X-ray optics is given below.

2.3.1 Multilayer monochromator

A multilayer monochromator consists of a periodic layer structure of an element with high atomic number (high Z element) followed by a low Z element. The thickness of two consecutive layers (the period of the multilayer d) is constant. X-rays are reflected in the transition border of low Z element layer (spacer) to high absorbing material. For photons hitting the multilayer monochromator under an incident angle of θ only those with a wavelength λ which satisfies the Bragg's law (equation 2.26) will interfere with each other constructively.

$$n\lambda = 2d \sin \theta \quad n=1,2,3,\dots \quad (2.26)$$

In synchrotron setups, two identical multilayer monochromators are used in a special geometry configuration to create a fixed-exit-geometry. The energy bandwidth $\frac{\Delta E}{E}$ for multilayer monochromators is about 10^{-2} .

2.3.2 Kirkpatrick-Baez mirrors

Kirkpatrick-Baez (KB) focusing optics consists of two total reflection elliptical mirrors, which are perpendicularly aligned (see Fig. 2.11). X-rays are directed to a focal point vertically by reflection from the first mirror and horizontally by a second mirror. Focused beam size of less than 50 nm have been achieved with KB mirror optics [24].

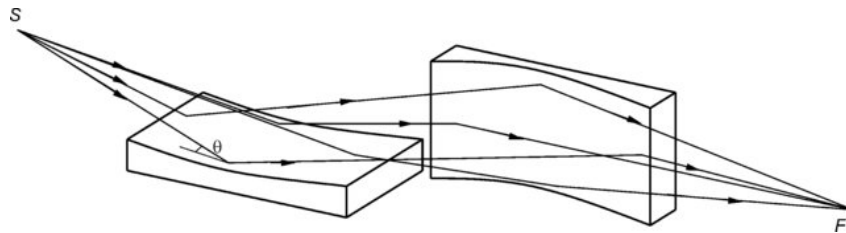


Figure 2.11: Schematic sketch of a Kirkpatrick–Baez-mirror system. Image from [25]

2.3.3 Polycapillary

Polycapillary lenses are made out of a large number of glass capillaries with very smooth inner surfaces. When X-rays enter one of those capillaries with a very small

glancing angle, smaller than the critical angle for total reflection θ_c , total reflection occurs at the glass walls. The X-rays are propagated within the capillary with hardly any intensity loss. All the mono glass capillaries in the polycapillary lens are aiming at the same focal spot. By using polycapillary lenses as focusing devices significantly higher X-ray intensities can be obtained compared to non-reflecting collimators. The intensity gain factor I_g (equation 2.27) is given as the ratio between the effective solid angle $\Delta \Omega_{eff}$ seen by the X-ray source (corresponding to the critical angle) and the solid angle when no reflections occur $\Delta \Omega$ (defined by the exit).

$$I_g = \frac{\Delta \Omega_{eff}}{\Delta \Omega} \quad (2.27)$$

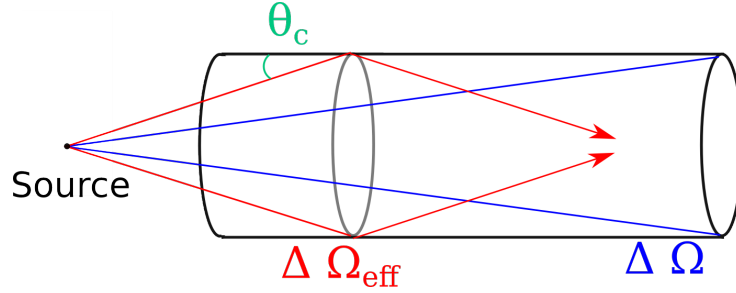


Figure 2.12: Schematic sketches of the intensity gain.

Polycapillary optics exist as full and as half lenses. Full polycapillary lenses focus a point source into the focal spot (Fig. 2.13 top). Half lenses can be used to either focus a parallel photon source, such as synchrotron radiation, in a single spot (Fig. 2.13 middle) or to define and limit the sample area seen by a detector (Fig. 2.13 bottom).

The critical angle for total reflection depends on the dispersion δ , the reflecting material (with density ρ , atomic number Z and mass number A) as well as on the energy of the radiation.

$$\theta_c \approx \sqrt{2\delta} \approx \frac{1}{E} \sqrt{\frac{Z\rho}{A}} \quad (2.28)$$

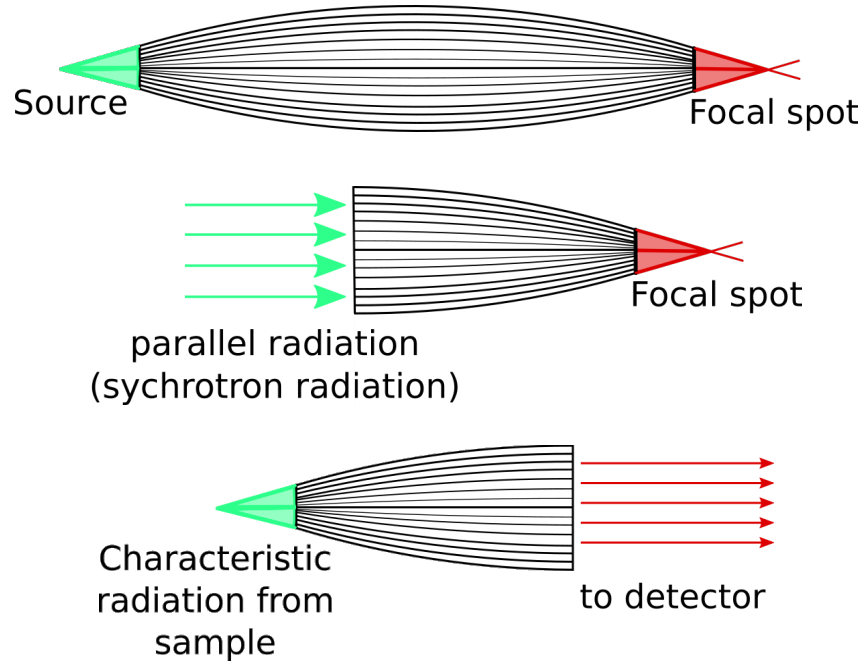


Figure 2.13: Schematic sketches of a polycapillary full lens (top) and polycapillary half lenses (middle and bottom).

For borosilicate glass the critical angle is given by:

$$\theta_c[\text{mrad}] \approx \frac{30}{E[\text{keV}]} \quad (2.29)$$

Therefore, polycapillaries change the intensities differently for different parts of a polychromatic spectrum. When a polycapillary lens is used between sample and detector, it changes the ratio between the characteristic radiation of different elements of the sample. As one can see from equation 2.28, the critical angle is smaller for higher X-ray energies and therefore for characteristic radiation from higher Z elements. This means that the acceptance angle of polycapillaries is smaller for heavier elements.

2.4 Sources of possible errors

Energy dispersive detectors measure counts versus energy as so-called spectra. Characteristic X-ray lines appear as gaussian peaks (or Voigt profile) over a background produced by scattering, low energy tailing and other possible effects.

2.4.1 Detector artefacts

Detector artefacts are peaks which are not characteristic peaks from the sample but rather are produced in the semiconductor detector. They have to be considered during spectrum fitting otherwise peaks might be misinterpreted.

Sum peaks

For high count rates it is possible that the detector registers two different signals, which are close together time-wise, as one. The resulting peak will be located at the energy sum of those two signals.

Escape peaks

X-ray photons with energies above the Si-K edge can excite atoms in the detector. As a consequence of this excitation, a photon with 1.74 keV (Si-K α) is produced. If this photon is created close to the detector surface, it can leave the detector. In this case the measured signal is 1.74 keV smaller than the energy of the original X-ray photon.

Compton edge

When a high energy X-ray beam is scattered incoherently at the surface of the detector crystal under an angle of 180°, an electron is produced which can enter the detector crystal. Due to the energy of this electron, the Compton edge appears in the low energy part of the spectrum.

2.4.2 Spectrum fitting

Spectrum fitting is performed to separate the actual signal (net counts) from the background as well as to resolve overlapping peaks. As X-ray imaging data is composed of lots of spectra, it is not possible to supervise the fitting of each single spectrum. Therefore, it is very important to create a reliable fitting model.

A good way to get a dependable model is to first have a look at the sum spectrum as it gives a good overview of the elements contained in the sample. After adding all elements found in the sum spectrum, the background model should be adapted. This is best done by adapting it to multiple single spectra. If possible the spectra should

be from different parts of the sample (for example regions of different mineralization in bone).

Within this thesis, all spectra were fitted using AXIL-QXAS [26, 27, 28]. AXIL is fitting the spectra with a least square routine and a Chi-square value (χ^2) is used as an indication of the quality of the fit. After fitting all spectra, it is a good idea to check spectra with high χ^2 -values for overlooked elements (which are missing from the model) and ill-adapted background. If additional elements or problems with the background routine are discovered, the model needs to be improved and the spectra refitted.

2.4.3 Information depth

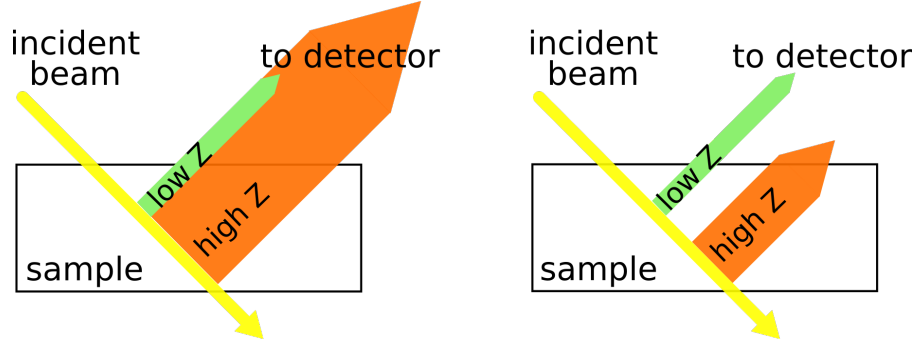


Figure 2.14: Information depth in a homogeneous (left) and heterogeneous sample for light (low Z) and heavy elements (high Z).

The information depth d_{inf} is the distance below the surface of a specimen from which information is contributed. It is usually defined as the depth where the fluorescence intensity ($I(E)$) is decreased to $1/e$ (about 37%) of its original value ($I_0(E)$) on its way out of the sample. The depth from which fluorescence radiation can be detected is limited by the attenuation of X-rays in matter which is described by the Beer-Lambert law. It is defined as followed:

$$I(E) = I_0(E) \cdot e^{-\mu(Z,E) \cdot x} \quad (2.30)$$

with $\mu(Z, E)$ [1/cm] being the linear mass absorption coefficient and x [cm] the thickness of the absorber.

As the attenuation is energy-dependent (and the energy of the fluorescence radiation is of course always smaller than the energy of the incident beam), the fluorescence energy dictates the information depth.

$$\frac{I(E)}{I_0(E)} = \frac{1}{e} = e^{-\mu(Z,E) \cdot d_{inf}} \quad (2.31)$$

$$-1 = -\mu(Z, E) \cdot d_{inf} \quad (2.32)$$

$$\frac{1}{\mu(Z, E)} = d_{inf} \quad (2.33)$$

Therefore, fluorescence radiation from light elements can only originate from the surface layer of the sample (see Fig. 2.14) while radiation from heavier elements can stem from much deeper layers. For heterogeneous samples (Fig. 2.14 on the right), this fact complicates the quantification of the measurements as the signal from high Z elements can not only stem from deeper layers but, due to the incident angle of the primary beam, might also be shifted in the position in one additional axis.

To reduce the effect of this obstacle, one can either measure thin (a couple of μm thick) samples or limit the area seen by the detector with X-ray optics as it is done in a confocal setup (see section 3.1.1).

Using the mass attenuation coefficients ($\frac{\mu}{\rho}$) for cortical bone from the National Institute of Standards and Technology (NIST) [29] and theoretical density (ρ) for hydroxyapatite of 3.16 g/cm^3 , one can estimate the information depth for various elements in bone (e.g. Ca-K: $24\mu\text{m}$, Zn-K: $60\mu\text{m}$, Pb-L: $111 \mu\text{m}$ and Sr-K: $352 \mu\text{m}$).

3 Beamlines and experimental setups

3.1 SR-XRF

Synchrotron radiation-induced X-ray fluorescence (SR-XRF) analysis with micro- or nanometer resolution is a powerful method to non-destructively investigate element distribution in a wide variety of samples [30, 31, 32]. Measurements are performed at microscopically small areas of a larger sample. The technique is widely used for analytical tasks in different fields, such as geological sciences, art and archeology, environmental, biological, and biomedical applications [30]. SR-XRF imaging can be performed in scanning or in full-field mode.

3.1.1 Confocal SR- μ XRF

Confocal synchrotron radiation micro X-ray fluorescence (SR- μ XRF) has proven to be an effective tool for qualitative and semi-quantitative analysis of spatial distribution of trace elements in bone samples [33, 34, 35]. This method takes advantage of various characteristics of synchrotron radiation such as high photon flux, polarization, collimation and the easily changeable primary photon energy which enables to detect absolute amounts in the femtogram range (for medium Z elements).

In a confocal setup two X-ray optics (often polycapillaries) are used to define the sample volume from which the fluorescence radiation is detected. The first X-ray optics system focuses the primary beam on the sample. The second X-ray optics is placed between the sample and the detector. The angle between the two optics is 90° . The overlap of the focal spots of the two optics defines a volume from which the fluorescence radiation is seen by the detector (see Fig. 3.1). The sample

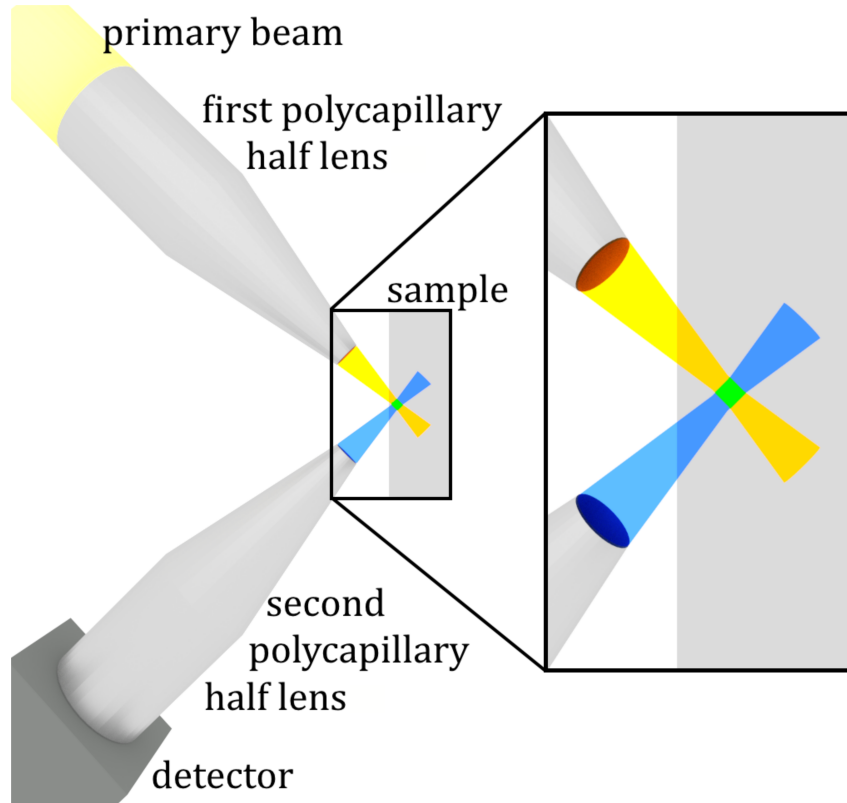


Figure 3.1: Schematic sketch of the confocal SR- μ XRF setup. The sample is scanned through a well-defined detection volume (green square) created by the overlap of the focal spots of the polycapillary half lenses.

can be moved through this detection volume, which allows to acquire information from the region of interest (ROI) voxel by voxel. Furthermore, the confocal setup eliminates fluorescence radiation (in particular of high Z elements) of deeper layers and therefore improves the overall spatial resolution. Measurements in different layers of the sample are possible and can provide 3D Information.

Further details on confocal SR- μ XRF can be found elsewhere [30, 36].

ANKA – FLUO beamline

The synchrotron light source facility ANKA (Angströmquelle Karlsruhe, KIT, Karlsruhe, Germany) typically operates at a kinetic electron energy of 2.5 GeV. During operation, the storage ring is injected with electrons twice a day. The starting ring current is usually about 150 mA and decreases over time.

The confocal setup at the FLUO beamline (see Fig. 3.2) at ANKA [36] was used during multiple beamtimes.

For this setup, a W/Si double multilayer was used for monochromatization. The excitation energy was chosen at 17 keV. As focusing optics two polycapillary half lenses were used. The fluorescence radiation was detected with a 50 mm² silicon drift detector (Vortex). The detection volume for the setup was determined by scanning 0.1 μm thick gold (Au) micro-structures. As the size of the detection volume is energy-dependent the step sizes were chosen to be slightly smaller than the detection volume for Au-L α (9.711 keV).

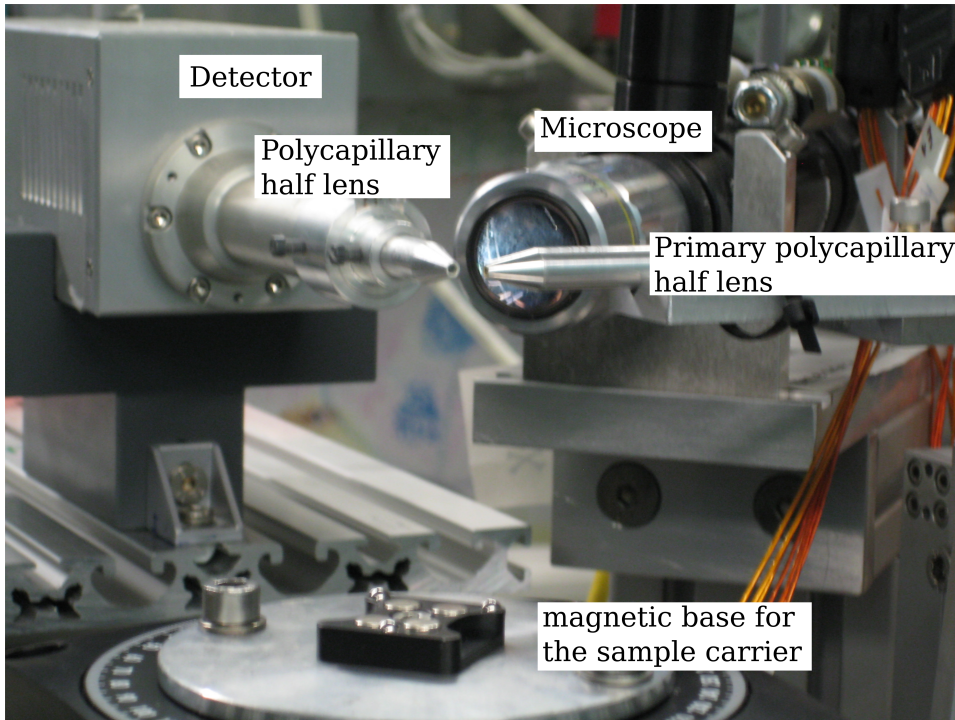


Figure 3.2: Confocal μXRF setup at the FLUO beamline at ANKA.

BESSY II – mySpot beamline

The photon source BESSY II (Helmholtz-Zentrum Berlin fuer Materialien und Energie (HZB), Germany) is usually operated in a multi bunch top-up mode with a kinetic energy of 1.7 GeV and a ring current of 300 mA.

The confocal setup at the mySpot beamline (Fig. 3.3) was used for the measurements

of the osteomalacia samples (see chapter 9). The angle between the two polycapillary half lenses is 90° . However, the second optics is not in the same plane as the first (and the primary beam) but offset by an angle of 20° . This is done to see more scattering from the sample to get an idea about the distribution of the low Z elements in the sample.

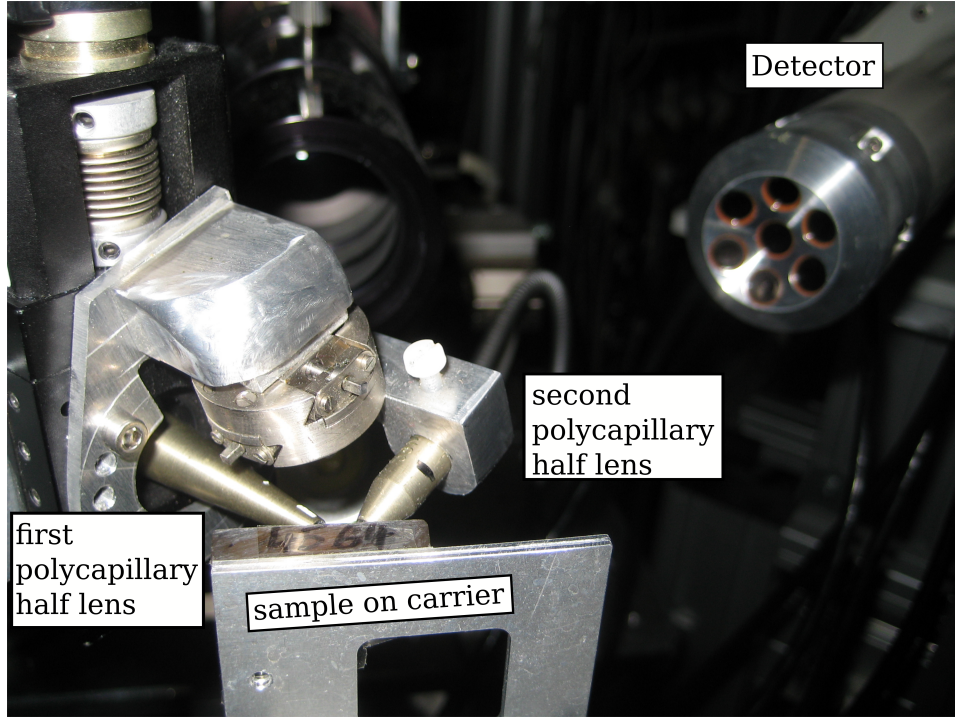


Figure 3.3: Confocal μ XRF setup at the mySpot beamline at BESSY II. For the measurements, the detector was moved as close as possible to the second polycapillary half lens.

A MoB_4C multilayer ($2d = 2\text{nm}$) was used to set the monochromatic exiting energy to 17 keV. The characteristic radiation from the sample was detected with one of the elements of a liquid nitrogen cooled 7-element $\text{Si}(\text{Li})$ detector (Gresham) with an active area of 30 mm^2 .

3.1.2 Full-field SR- μ XRF

As indicated by the name, in a full-field setup the complete area of interest of the sample is irradiated at the same time. Therefore, there is neither a need for a

first x-ray optics to focus the primary beam, nor is it required to move the sample through the beam.

In order to obtain the space-resolved information of the measured area, a detector with spatial resolution (e.g. a charge-coupled device (CCD)) and an optic are necessary. Without the optics between sample and detector, radiation from various parts of the measured sample could reach the same CCD pixel. Only by using an optics such as a pinhole (camera obscura) or a polycapillary half lens (allows for additional magnification) the space-resolved elemental distribution can be observed.

BESSY II – BAMline

The color X-ray camera (CXC) [37, 23] installed at the BAMline at BESSY II (Helmholtz-Zentrum Berlin fuer Materialien und Energie (HZB), Germany) works in full-field mode and allows both the detection of the energy of the X-ray photons as well as their spatial resolution. The CXC consists of a pn-junction charge-coupled device (pnCCD) and a polycapillary optics. The spatial resolution of the CXC is defined by the pnCCD pixel size ($48\ \mu\text{m}$) and the used polycapillary optics.

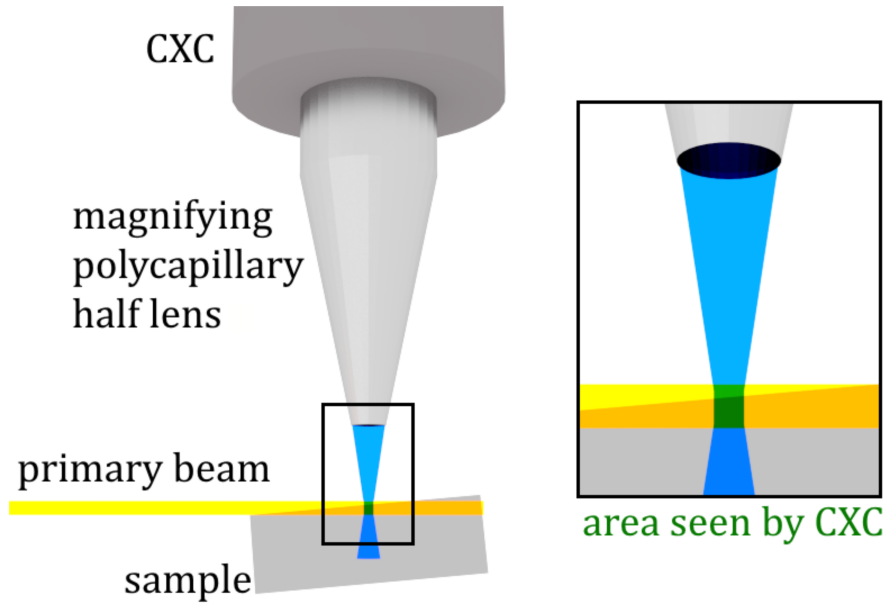


Figure 3.4: Schematic sketch of the full-field CXC setup. The whole measured sample area (264×264 pixel) is excited at once (full-field mode).

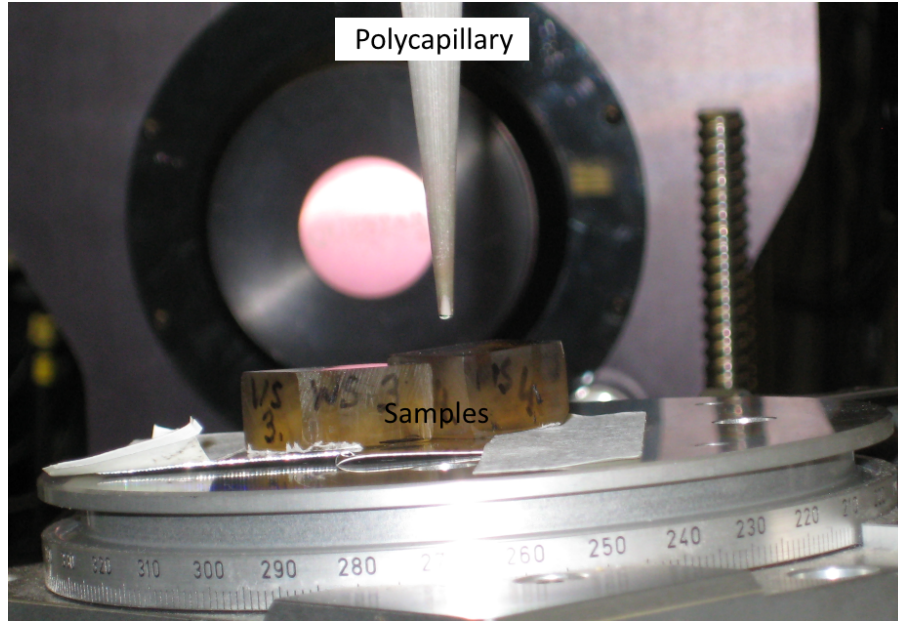


Figure 3.5: CXC setup at the BAMline at Bessy II.

For these measurements, a conical shaped magnifying polycapillary optics (magnification factor 1:8) was used (see Fig. 3.5). The spatial resolution was about $7 \times 7 \mu\text{m}^2$ in a single pixel. The depth resolution depends on the X-ray energy of the detected element as well as on angle between the collimated primary beam and the sample, which was varied between 2.5° and 5° . The samples were excited at 12.6 keV in order to maximize the Zn XRF production. A schematic sketch of the setup is shown in Fig. 3.4.

As one can see from Fig. 3.4, depending on the angle between the primary X-ray beam and the sample the CXC will see deeper into the sample downstream from the primary X-ray beam.

3.1.3 SR-submicro XRF

Nowadays, the smallest beam sizes (and therefore highest resolution) available for scanning SR-XRF imaging reach a few tens of nanometers [38, 39]. However, for many biological samples such high resolution beams are already too small to scan meaningful areas of interest on the samples on a reasonable time scale. For instance, the samples of our interest are bone tissue and articular cartilage. Within the bone we are mostly interested in osteons (diameter of $200 \mu\text{m}$). As one can imagine, scanning of such an object with such a small beam would require considerable time.

Therefore, submicro XRF is a perfect choice, allowing to measure such structures, and moreover, to resolve substructures, such as cement lines and tidemarks in bone (several micrometers thick).

Diamond Light Source – B16 beamline

The synchrotron radiation-induced XRF (SR-XRF) setup was installed for multiple experimental sessions at the B16 bending magnet test beamline of the Diamond Light Source synchrotron (see Fig. 3.6), a beamline committed to be easily adaptable and adjustable to the particular requirements of various experiments [40, 41]. The Diamond Light Source storage ring operates in top-up mode (3 GeV electron energy, 300 mA ring current). For the SR submicro-XRF experiment, the X-ray energy was set with a RuB₄C double multilayer monochromator (FMB Oxford Ltd., Oxford, UK), which can be used to produce a high flux monochromatic beam in the range of 8-20 keV [42]. The beam was focused with a Kirkpatrick–Baez (KB) mirror pair (Diamond Light Source Ltd., in-house design and construction). The sample stage consisted of piezo crystal-based motors (each of the xyz axes is a ECS5050 piezo stage, attocube systems AG, Munich, Germany) and a high-purity methyl acrylate sample holder, which was 3D-printed from a clear photoreactive resin (Form 2, Formlabs Inc., Somerville, USA) at the Diamond Light Source. The angle between the primary beam and sample was 45°.

Additionally, the setup was equipped with an optical microscope (Optem Fusion, Qioptiq, Germany), which was focused on the backside of the samples (see Fig. 3.6). This allowed identification of the regions of interest quickly. The X-ray fluorescence radiation was detected at an angle of 45° to the sample or 90° to the primary beam. Please note, that due to the setup's geometry in particular the angle of 45° between primary beam and sample, the horizontal resolution is worsen with the increase of the sample thickness. Additionally, as the microscope sees the sample from the backside, the sample should be transparent to find the areas of interest. Therefore, the recommended sample thickness should be in the range of up to several micrometers.

The size of the focused beam was determined by using a knife-edge scan of a 50 µm Au wire. Measurements of standards were performed with 17 keV to optimize the excitation for elements up to Sr.

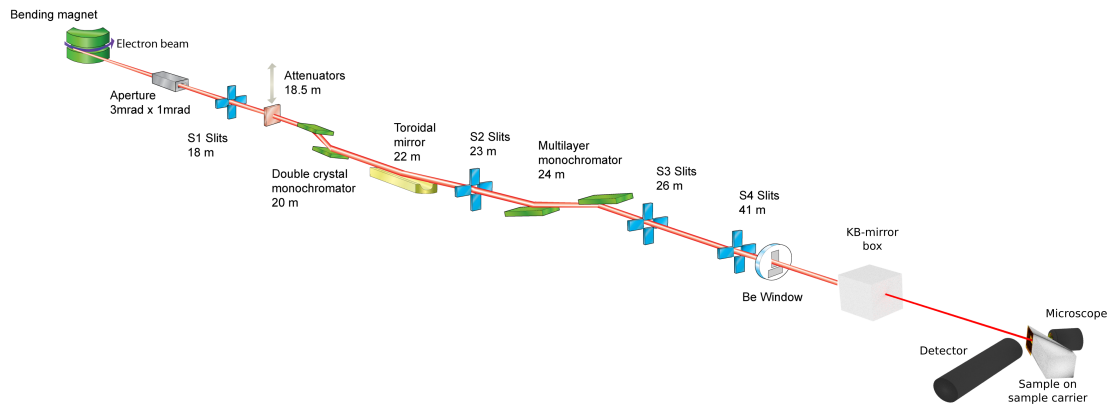
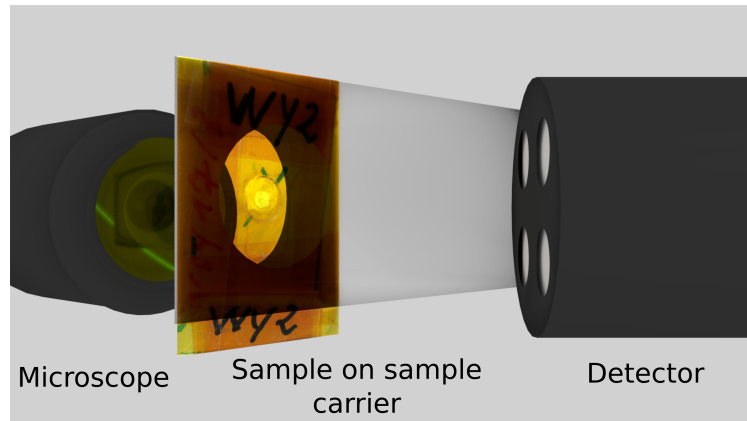
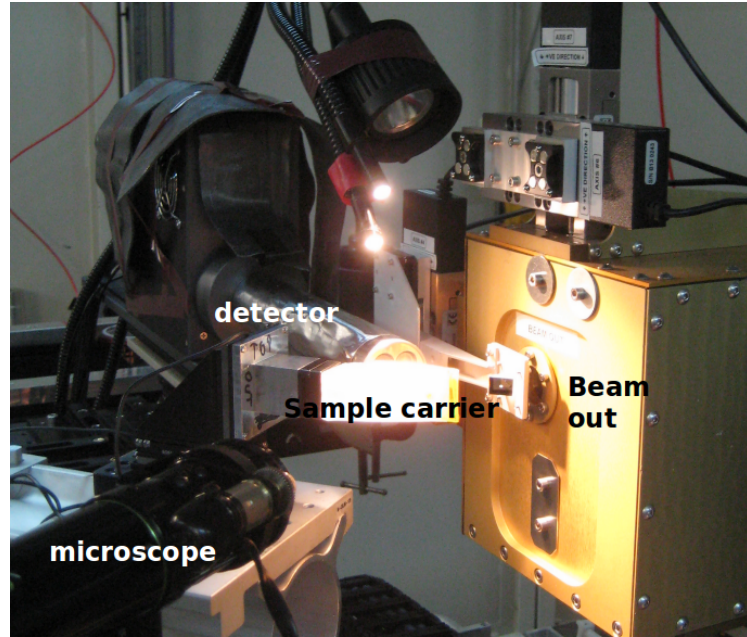


Figure 3.6: Above: Photograph of the setup at B16. Middle: Image of the microscope, a sample on its carrier and the detector (seen from the position of the beam). Below: B16 Beamline Schematic (Image adapted from [43])

The measurements were recorded with a Vortex 4-element detector (Vortex-ME4, Hitachi Ltd., Tokyo, Japan) with a total active area of $200\text{ }\mu\text{m}^2$ and SII electronics. The beam resolution (FWHM) determined with a $50\text{ }\mu\text{m}$ Au cross was about 500 nm (vertical) \times 600 nm (horizontal).

4 Quantitative backscattered electron imaging (qBEI)

Quantitative backscattered electron imaging (qBEI) gives a signal proportional to the average atomic number of the target material. For bone, calcium (Ca) - the major bone constituent with the highest atomic number ($Z=20$) - prevails the signal, which allows one to determine the degree of tissue matrix mineralization (Ca content) at each pixel area of the imaged tissue section. In the qBEI images, bright areas describe higher and dark areas lower mineralized matrix.

A digital scanning electron microscope (DSM 962, Zeiss, Oberkochen, Germany) equipped with a four-quadrant semiconductor backscattered electron detector was used. The scanning electron microscope was operated at 20 keV beam energy and ROIs were imaged with $200\times$ nominal magnification (pixel resolution $1\text{ }\mu\text{m}$).

A typical qBEI of cortical bone can be seen in Fig. 4.1. More information about qBEI can be found elsewhere [44, 45, 46, 47].

All qBEI images shown in this thesis were recorded by personnel of the Ludwig Boltzmann Institute of Osteology in Vienna, Austria.

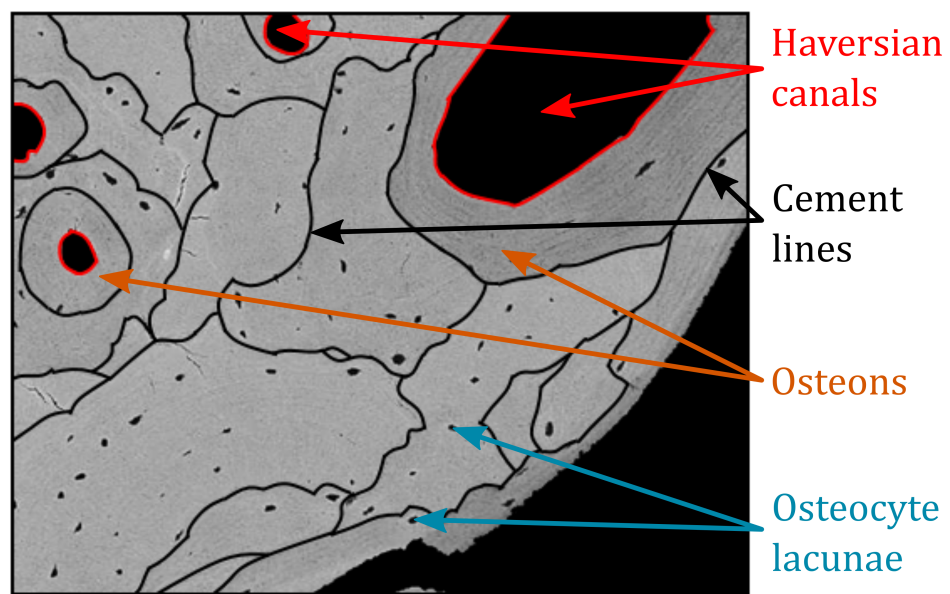


Figure 4.1: Cross section of cortical bone - qBEI close-up. Cement lines were marked in black.

5 Comparison of a confocal and a CXC setup

Parts of this chapter were previously published in the Journal of Synchrotron Radiation [48].

While confocal SR- μ XRF (a scanning mode technique) was successfully used for measurements of trace elements distributions in bone and cartilage before [33, 49, 50, 51, 52, 53] the question remained, whether or not a full-field technique would decrease measurement time and improve resolution.

To answer this question and to test the use of both modes for the analysis of thin bone micro-structures such as tidemarks (transition zone between different phases of cartilage) and cement lines (the boundaries of osteons, the fundamental functional units of compact bone), we measured the same bone samples with two different systems - a confocal SR- μ XRF and Color X-Ray Camera (full-field mode) setup.

A high fraction of the total body zinc (Zn) is stored in bone tissue. Zn is the co-factor of various metalloenzymes, which play a major role in the mineralization process on new bone formation sites as well as in bone resorption and remodeling [54, 55]. Additionally, increased Zn levels stimulate bone formation [56, 5]. All this makes the analysis of Zn distributions in bone very intriguing. Therefore, both of the setups were optimized to measure Zn.

5.1 Materials and methods

5.1.1 Samples

Three human bone samples (seven regions of interest in total) were studied. These samples were vertebral bone tissues taken as biopsies from patients with vertebral

compression fractures. Informed consent of all patients was obtained to use the material for research purposes. The study was conducted according to the guidelines of the Helsinki Declaration and approved by the ethics committee of the Medical University of Vienna, Austria.

The bone samples were undecalcified, dehydrated and fixed in a gradient of ethanol concentration (50 to 100%) and embedded in polymethylmethacrylate (PMMA). The sample blocks were trimmed (low speed diamond saw, Buehler Isomet, Lake Pluff, USA) and ground using sand paper with decreasing grit size and finally polished with a precision polishing device (PM5, Logitech Ltd, Glasgow, UK). A more detailed description of the sample preparation can be found in previous publications [45, 44].

5.1.2 SR- μ XRF

Confocal SR- μ XRF measurements were performed at the FLUO beamline at ANKA (see section 3.1.1). These measurements were compared to the results from the Color X-Ray Camera (full-field mode) and the BAMline of BESSY II (see section 3.1.2). Typical spectra for both setups can be seen in Fig. 5.1.

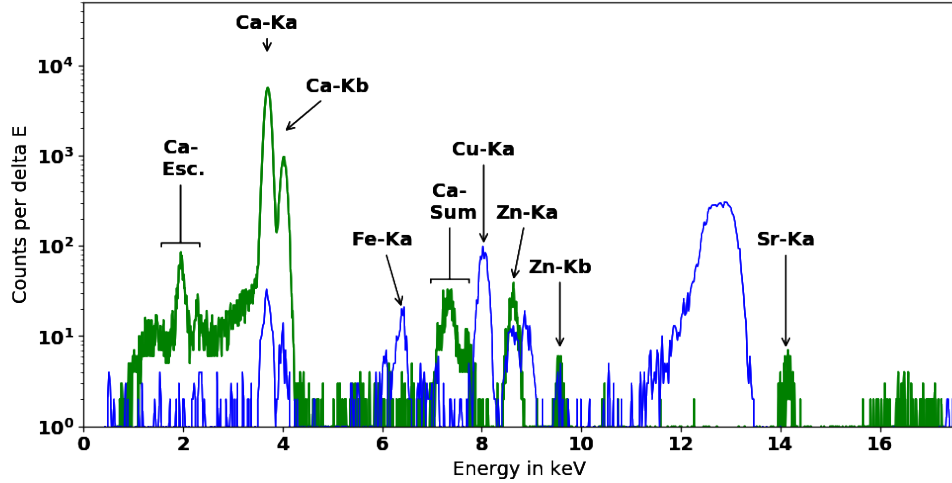


Figure 5.1: Typical SR- μ XRF spectra as obtained with a confocal setup (green) and with a full-field setup Color X-ray Camera (blue). Spectra shown correspond to measurement points of the mineralized bone area of Fig. 5.3.

5.2 Results

The raw spectral data were analyzed using the AXIL [26, 27, 28] and MICROXRF2 (B. Vekemans, XMI, Universiteit Gent) software packages in order to extract the net-line XRF intensities for each measurement point (confocal XRF) or pixel (CXC), and convert them into elemental maps.

As an example the Ca and Zn elemental maps as well as the corresponding qBEI of two areas which were measured with both setups are shown in figures 5.2 and 5.3.

Measurement time for the maps obtained in scanning mode (ANKA) were 2 s per pixels (about 3.6 h per map). The measurements with the full-field mode (BESSY II) were performed with an angle of about 2.5° between sample and primary beam and 5.5 h measurement time (Fig. 5.2) and with an angle of about 5° and 18 h measurement time (Fig. 5.3), respectively.

As one can see from those figures, we were able to image the Ca distribution with both setups quite satisfactorily. By comparing the Ca maps with the corresponding qBEI data (e.g. by observing the small holes in the bone in Fig. 5.2), one can easily see the higher resolution in the plane in the BESSY II maps.

By observing bigger hole structures in the qBEIs and comparing them to the Ca maps one can see that especially the right side of the BESSY II maps show some structure from deeper layers which is neither visible in the qBEIs nor in the ANKA maps. This leads to the conclusion that the depth resolution of the BESSY II maps is worse compared to the ANKA maps. Additionally, it should be mentioned that the depth resolution of our measurements at BESSY II is dependent on the angle between sample and primary beam and will be slightly different in different parts of the elemental maps (see Fig. 3.4)

Although the Ca distribution is clearly imaged in the BESSY II maps the same does not hold for the Zn distribution. For the maps measured for 5.5 h with a 2.5° angle between sample and primary beam, the intensity was too low (and therefore the signal was too noisy) to reliably recognize the bone structure in the Zn distribution (see Fig. 5.2). For this reason, we measured the next sample for a longer time (18 h) and with a larger angle (about 5°). While this improved the intensity by approximately a factor of 5, the Zn distribution imaged in Fig. 5.3 shows a pattern, which is not consistent with the qBEI and the Ca distribution. The reason for this is the higher energy of the Zn- $K\alpha$ line (8.6 keV) compared to

the Ca-K α line (3.69 keV) due to which we get the Zn signal with a worse depth resolution than the Ca signal. As the qBEIs had a depth resolution of 1 μm , the low depth resolution of the BESSY II maps also makes it harder to correlate the elemental maps with the bone structure seen in the qBEIs.

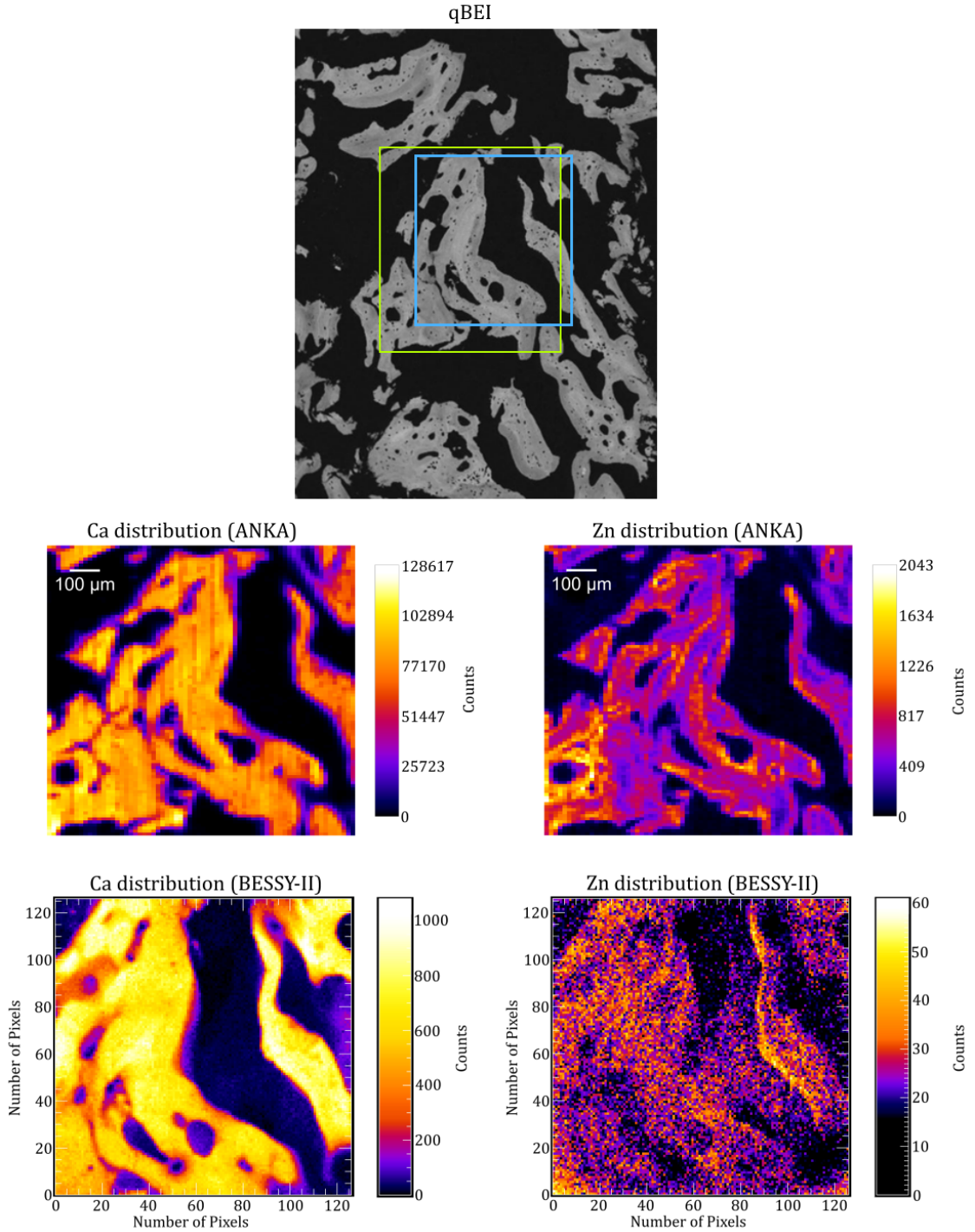


Figure 5.2: qBEI as well as Ca and Zn maps from the approximately the same area measured at ANKA and BESSY II. The exact area measured at ANKA is marked by a green rectangle in the qBEI. Measurement time per pixel was 2 s (about 3.6 h for the complete map). The measurement performed at BESSY II was done in the region marked in blue and took 5.5 h. The angle between primary beam and sample was about 2.5° .

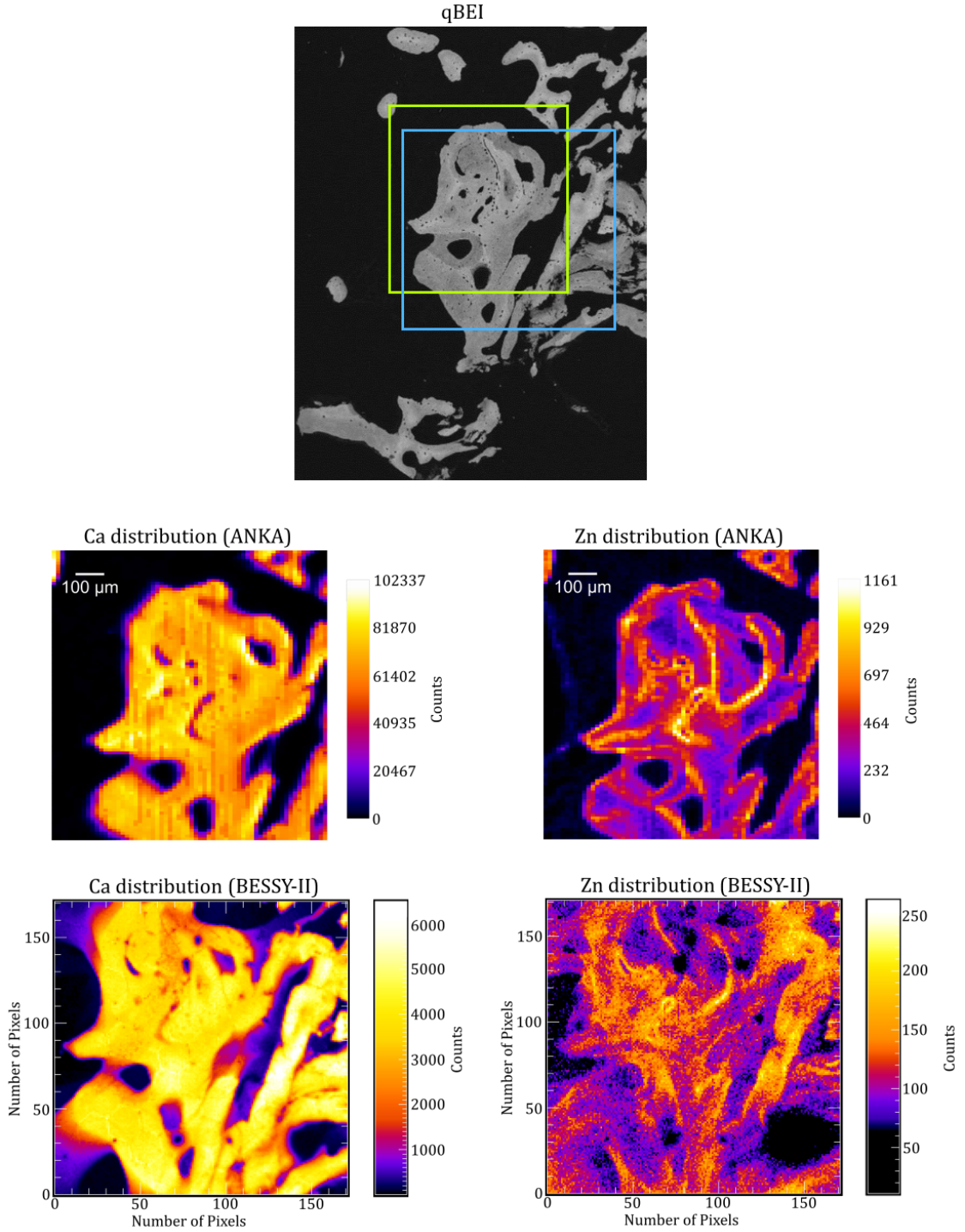


Figure 5.3: qBEI as well as Ca and Zn maps from the approximately the same area measured at ANKA and BESSY II. The exact area measured at ANKA is marked by a green rectangle in the qBEI. Measurement time per pixel was 2 s (about 3.6 h for the complete map). The measurement performed at BESSY II was done in the region marked in blue and took 18 h. The angle between primary beam and sample was about 5°.

5.3 Conclusion

While the CXC setup with the better resolution in the plane would be great to image the Ca distribution (one of the major elements in bone) in the samples, the count rates of Zn (trace element) were too low to take advantage of that. Enlarging the angle between primary beam and sample to obtain higher Zn count rates worsens the depth resolution and makes it harder to compare the elemental maps with the qBEIs from the surface. Additionally, the long radiation times with the primary beam must have heated up the samples significantly. Fig. 5.4 shows two samples after they were irradiated for 18 h. As one can see, the PMMA had become so hot that it blistered and destroyed the smooth sample surface.



Figure 5.4: Two samples after 18 h in the primary beam (at an angle of about 5°).

The confocal SR- μ XRF setup at ANKA allowed us to image both Ca and Zn sufficiently, which made it possible to see a higher Zn accumulation in the cement line regions. However, as the cement line is only a few nanometers thin, the resolution is too low to investigate possible substructures. Furthermore, it should be mentioned, that the ANKA synchrotron is no longer available for peer-reviewed user operation to the external users. To further investigate narrow bone structures and potential substructures a combination of SR- μ XRF and TXM (Transmission X-ray Microscopy) with thin samples could be fruitful. The use of thin samples could also solve the problem of restricted depth resolution for the CXC setup. Additionally, the CXC setup would benefit from optics with a higher efficiency to obtain results comparable to the confocal setup.

6 Characterization of a submicro-XRF setup on the B16 beamline

Parts of this chapter were previously published in the Journal of Synchrotron Radiation [57].

To find the ideal SR-XRF imaging method for the investigation of trace element distributions and possible substructures (in the micrometer range) in biological samples, such as bone, single cells and other tissues [58, 59] SR-XRF at the B16 beamline at the Diamond Light Source was tested with different samples and a standard reference material.

To characterize the setup, especially for thin samples, a NIST standard (Standard Reference Material 2783 – Air Particulate on Filter Media, NIST, Gaithersburg, USA) was measured. This standard is quite heterogeneous as one can see from the distribution maps of Ca, Fe, Cr and Zn in Fig. 6.1. The certified values can only be considered to be valid within the stated uncertainty if an area of at least 1 cm^2 is measured [60]. As one can easily see this is too large of an area to analyze with a sub-micrometer beam. Additionally a measurement time of 120 s per pixel was required for this standard to produce an evaluable spectrum. To obtain sensitivity and lower limits of detection in reasonable time, the area scanned was limited to 6×6 pixels (considering our beam size this results in an area of about $10.8 \text{ }\mu\text{m}^2$). Between each point measured the sample was moved by $10 \text{ }\mu\text{m}$ (step size). Additionally to the loaded filter, a blank filter (also part of the NIST SRM 2783) was scanned the same way. This allowed determination of the components of the signal that originate from the blank filter alone. Sum spectra for the loaded

and the blank filters (see Fig. 6.1 top left) were fitted using AXIL-QXAS ver. 3.6 [26, 27, 28]. Sensitivities and lower limits of detection (LLD) were calculated using the fitted result of the loaded filter corrected with the net counts of the blank filter. The uncertainties for the sensitivities were calculated by using the uncertainties (about 95%) given in the NIST certificate [60] as well as two times the fit error (2σ) of the fitted net counts of the loaded filter. Please be aware that due to the considerably smaller measured area (compared to the given recommendation), the error bars shown in Fig. 6.1 do not correspond to a confidence interval of 95 % and are only given as a rough indication. As one can see from Fig. 6.1 the sensitivities obtained ranged from about 8 cps/fg for Ca-K α to 249 cps/fg for As-K α , while lower limits of detection ranged from 169 to 4 ag in 1000 s.

To put these values in perspective, a comparison with the LLDs for Mn and Cu reached at the ID16B-NA beamline at the ESRF can be seen in table 6.1.

Table 6.1: Comparison of the lower limits of detection (LLD) for Mn and Cu determined for the B16 beamline at the Diamond Light Source and the ID16B-NA beamline at the ESRF as well as some of the measurement parameters. For both beamlines a multi-element standard was scanned to determine the LLDs for various elements. The values for the ESRF ID16-NA beamline are taken from [61]. For ESRF the standard was NIST SRM 1832 - Thin Glass Film on Polycarbonate for X-ray Fluorescence Spectrometry.

	Diamond B16	ESRF ID16B-NA
Mn-K LLD (in ag for 1000 s)	15	0.0457 (12 ppm)
Cu-K LLD (in ag for 1000 s)	7	0.0136 (4 ppm)
Standard	NIST SRM 2783	NIST STM 1832
Measurement time/pixel	120 s	0.1 s
Excitation	17 keV (multilayer monochromated)	17.5 keV (pink beam)
Spot size (vertical \times horizontal)	500 nm \times 600 nm	59 nm \times 48 nm
Step size (vertical \times horizontal)	1 μ m \times 1 μ m	0.85 μ m \times 0.9 μ m

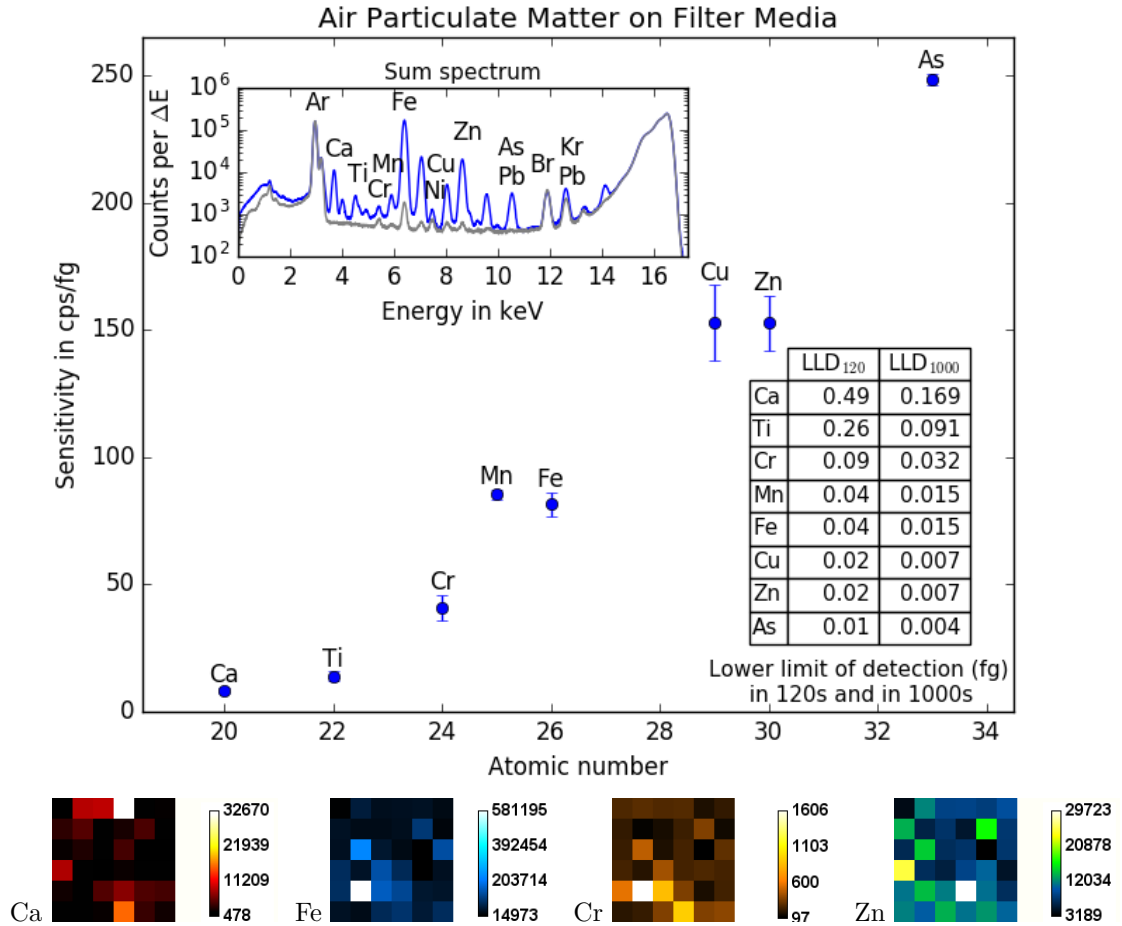


Figure 6.1: Above: Sensitivities, lower limits of detection (inset table) and sum spectra (inset; in blue for the loaded, gray for the blank filter) of 36 (6×6) pixels measured on the NIST Standard Reference Material (SRM) 2783 (Air Particulate on Filter Media) with 17 keV monochromatic excitation. Note that the whiskers on the sensitivity values are most likely underestimated due to the small size of the measured area. Below: The distribution maps for four selected elements (Ca, Fe, Cr and Zn) showing the inhomogeneity of the SRM. The distance between pixels was 10 μm . Measurement time per pixel was 120 s.

6.1 Scanned Samples – Results

To show the potential of the XRF setup on B16, scans from three projects are presented in this section. The analysis of three different sample types was carried out with 17 keV. An Au test structure was measured to show the resolution capabilities of the setup. The results of an area measured in bone and the elemental maps gained by measuring a single cell demonstrate the potential of the XRF setup tested at B16 for biological samples.

6.1.1 Gold test structure

This sample was produced for the Atominstitut (ATI) by the Karlsruhe Nano Micro Facility (KNMF) by the means of electron beam lithography. A 4 inch Silicon wafer was coated with a start layer (10 nm Ti, 100 nm Au) for electroplating by vapor deposition. The structures were written as trenches in a 1.5 μm thick PMMA layer with an electron beam writer (EBPG5200Z, Raith, Germany). Dose was 800 $\mu\text{C}/\text{cm}^2$. Development took place in a mixture of MIBK and IPA (1:1). The trenches had been filled with Gold of 1 μm thickness by electroplating. Residual resist was removed by Oxygen plasma. The sample is a Ti-coated (over the whole surface) Si wafer. On top of the Ti layer there are Au structures in the shape of 100 $\mu\text{m} \times 100 \mu\text{m}$ squares and consecutive stripes of different widths between 1 and 10 μm . A microscope image of the sample is shown in Fig. 6.2.

Two areas of this sample were scanned with the XRF setup on B16; the square shown on the bottom right (of the microscope image, Fig. 6.2) as well as parts of the line structure on the bottom left. From top to bottom - the first stripe of the line structure has a width of 10 μm and is followed by a gap of 10 μm , the second stripe has a width of 9 μm , followed by a 9 μm gap. The stripe widths and stripe gaps decrease in 1 μm steps down to the smallest stripe which has a width of 1 μm . Both structures were scanned with a step size of one μm and a measurement time of one second. Measurements for the two Au maps took about 50 minutes for the stripes and 8 hours for the square, respectively. The time given above includes the time needed for the communication of the measurement software with the detector and motor movements time (about one second per pixel).

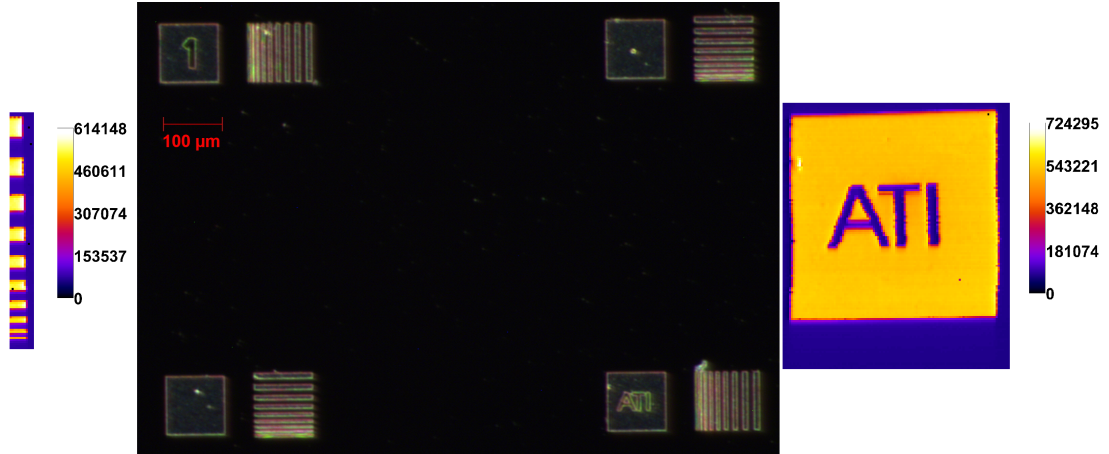


Figure 6.2: Au maps from SR-XRF (left and right) and microscope image (middle) of the KNMF gold test structure

The results from the scanned Au structure confirm that 1 μm structures are easily resolved with the XRF setup on B16.

6.1.2 Human bone biopsy sample

The sample is a vertebral body biopsy and was prepared as 4 μm (thickness) cut. This cut was sandwiched between two 8 μm Kapton foils and fastened between Plexiglas frames. The bone sample was thus fixed on the sample carrier, which can be seen in Fig. 3.6.

Fig. 6.3 shows a microscope image of the area of the sample measured (top left), the Ca distribution of an overview scan (bottom left) and the Ca, Zn, Sr and Co distribution of the final high resolution scan. The overview scan was performed with a step size of 20 μm and a measurement time per pixel of 2 seconds. The overview area was 400 $\mu\text{m} \times 360 \mu\text{m}$ and the scan took about 20 minutes.

The high resolution scan (step size 1 μm) was performed in the area marked with a blue frame in the microscope image and was optimized for measuring Zn and therefore a considerably longer measurement time (20 s per pixel) was needed. The whole scan took about 15 hours. The scan area is 11 \times 237 μm^2 . A single spectrum of the sample is shown in Fig. 6.4.

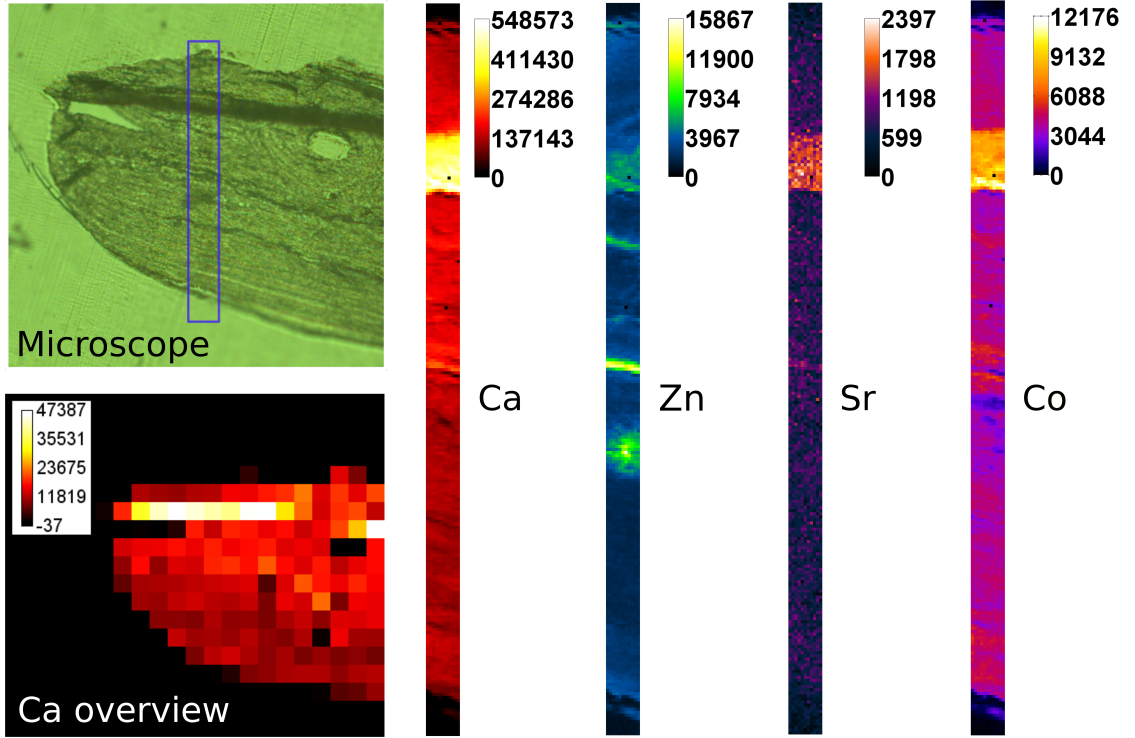


Figure 6.3: Microscope image (upper left) of the measured bone sample as well as the Ca distribution of a rough scan over this sample (lower left) and the distributions for Ca, Zn, Sr and Co of the fine scan (right).

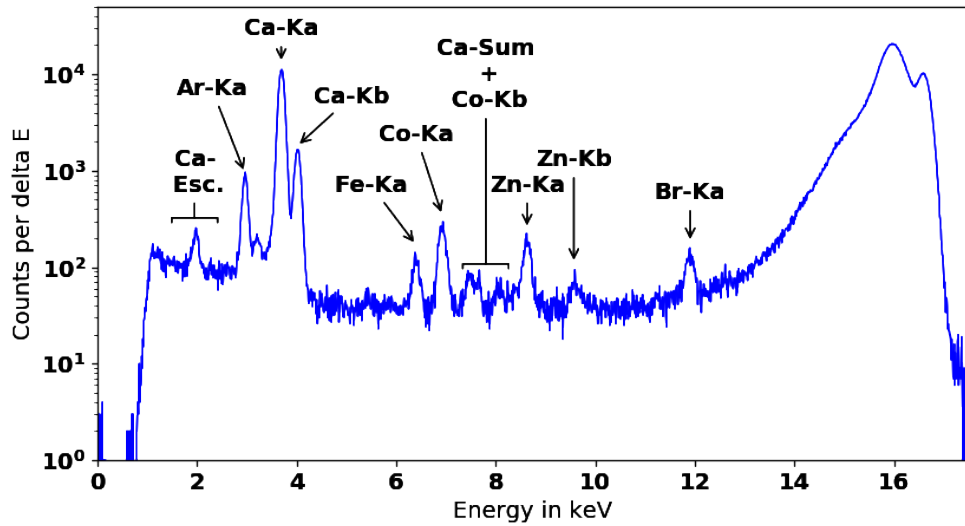


Figure 6.4: Spectrum of a bone sample measured at B16.

Fig. 6.3 demonstrates that the setup is not only capable of imaging thin structures in bone samples (especially visible in the Zn map) but also that the resulting elemental maps can easily be correlated to microscope images using rough scans.

6.1.3 Cancer Cell

These measurements were performed as a part of a project investigating the localization of metals within cells. Human A-375 malignant melanoma cells (ECACC, Salisbury, UK) were grown on $7.5\text{ mm} \times 7.5\text{ mm}$ low stress silicon nitride windows with a thickness of 500 nm (Norcada, Edmonton, AB, Canada). Cells were treated with copper sulfate and chelators. A more detailed description of the sample treatment can be found in [62, 63].

Generally, a maximum of 100 cells per total area is sufficient. Usually, a cell suspension of half a million cells in 2 ml of medium is prepared and applied to the plate. The cells will adhere to the membrane. If too many cells have been placed on the membrane, the process should be started from the beginning; if too little, then more cells should be pipetted. If this method is used, we can scan individual cells and small groups of cells on the same membrane.

The cell sample area was measured for 5 s per pixel with a step size of $0.5\text{ }\mu\text{m}$. Area size is $20\text{ }\mu\text{m} \times 20\text{ }\mu\text{m}$ (41×41 pixels). The complete scan took about 2.8 h. The elemental maps in Fig. 6.5 show the suitability of the setup to investigate elemental distributions within a single cell.

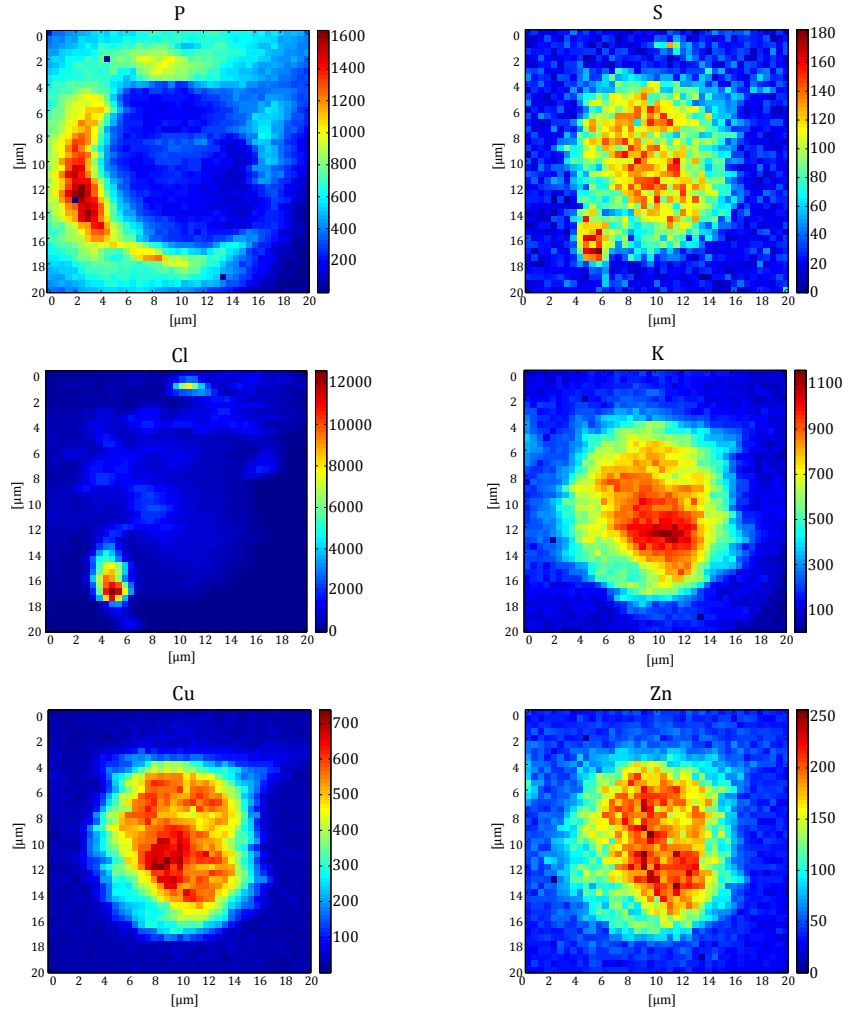


Figure 6.5: P, S, Cl, K, Cu and Zn maps of a copper-poisoned human A-375 malignant melanoma cell.

6.2 Conclusion

We characterized an XRF setup on the B16 beamline at the Diamond Light Source using an excitation energy of 17 keV using three different sample types as well as a standard sample. The beam size was determined as $500\text{ nm} \times 600\text{ nm}$ and thus the $1\text{ }\mu\text{m}$ structures of the Au test sample were easily resolved. The following sensitivities were obtained: 8 cps/fg for Ca-K α to 249 cps/fg for As-K α . The lower limits of detection ranged from 169 (Ca) to 4 ag (As) in 1000s. Although the detection limits presented do not reach the impressive values of the ID16B-NA at ESRF (due to the bigger beam size), the setup is very recommendable for imaging biological samples, which we illustrated by means of scans on a bone sample and a single cancer cell. Additionally, it should be mentioned that at the Diamond Light Source there exists the possibility to first scan a larger sample area at I18 with micrometer resolution (e.g. $2\text{ }\mu\text{m} \times 2\text{ }\mu\text{m}$) followed by further investigation of smaller areas of interest with sub-micrometer resolution at B16 [58]. In conclusion, the XRF setup on the B16 beamline is very well suited for studying thin samples and especially for biological applications.

7 Zinc and other trace elements in mineralized osteosarcoma and healthy tissue

Parts of this chapter were previously published in X-ray Spectrometry [64].

Osteosarcoma is the most common primary malignant bone tumor with a peak incidence in childhood and adolescence frequently occurring at sites of rapid bone growth [65] with a second smaller incidence peak in the elderly. While the exact cell of origin for this cancer remains to be ill-defined, osteosarcoma cells produce osteoid and tumor matrix that can mineralize. Due to the use of neoadjuvant chemotherapy long-term survival of patients with osteosarcoma has improved from 10 to 20 % to nearly 80 % within the last 25 years [66, 67]. However, these rates have not improved in the last 15 years [66, 67]. Therefore it is essential to get more insight into the fundamental biology of osteosarcoma that may lead to new treatment [68]. Trace elements have recently become a field of interest in various physiological processes in health as well as disease and especially in cancer [69, 70, 71]. It was found that trace element levels differ between normal and cancerous tissue [71, 1, 2, 72]. Moreover, novel approaches using trace elements to treat cancer have recently emerged [73].

Zinc (Zn) is an essential trace element implicated in several biological processes, and various studies reported significant changes in the levels of Zn in different cancer types [1, 74, 2, 72]. Zn is also an important trace element for bone metabolism [4]. Zn levels are known to affect the proliferation rate of osteoblasts [54]. The Zn concentration is higher in bone than in most of the other tissues [4]. Technical advances in recent times allow the spatial characterization of trace elements in

tissues. Confocal synchrotron radiation micro X-ray fluorescence (SR- μ XRF) has proven to be an effective imaging method for qualitative and semi-quantitative analysis of spatial distribution of trace elements in different materials [30]. We have successfully used this technique to characterize spatial distribution of various trace elements in cartilage and bone samples [33, 34, 35]. However, little is known about Zn levels in osteosarcoma. The aim of this study was to investigate the Zn content as well as its spatial distribution in human mineralized osteosarcoma tissue and compare it to adjacent normal bone using both confocal SR- μ XRF and quantitative backscattered electron imaging (qBEI).

7.1 Materials and methods

7.1.1 Patients

Nine patients (4 female/ 5 male) with a highly-malignant G3 osteosarcoma underwent wide resection of the tumor and implantation of a tumor prosthesis following neoadjuvant chemotherapy according to standardized protocols [75]. Eight patients were between 10 and 18 years old and one patient was 66 years old (Tab. 7.1). Seven samples were from the knee joint, one from the proximal femur and one from the proximal humerus. Grades of Regression were classified histologically according to Salzer-Kuntschik et al. [76]. Details are summarized in Tab. 7.1. The study was approved by the ethics committee of the Medical University of Vienna, Austria and was done in accordance with the Helsinki Declaration.

7.1.2 Sample preparation

All bone/tumor tissue samples were dehydrated and fixed in a gradient of ethanol concentration (50 to 100%) and embedded in polymethylmethacrylat (PMMA). The sample blocks were trimmed by a low speed diamond saw (Buehler Isomet, Lake Pluff, USA) and three micron thick tissue sections were cut by a hard microtome (LEICA SM2500, Leica Microsystems GmbH, Wetzlar, Germany) for histological examinations (Fig. 7.1). Modified trichrome Goldners and Giemsa staining was performed in representative samples. Consecutively, the blocks were ground with sand paper with decreasing grit size and finally polished by silk cloths loaded with

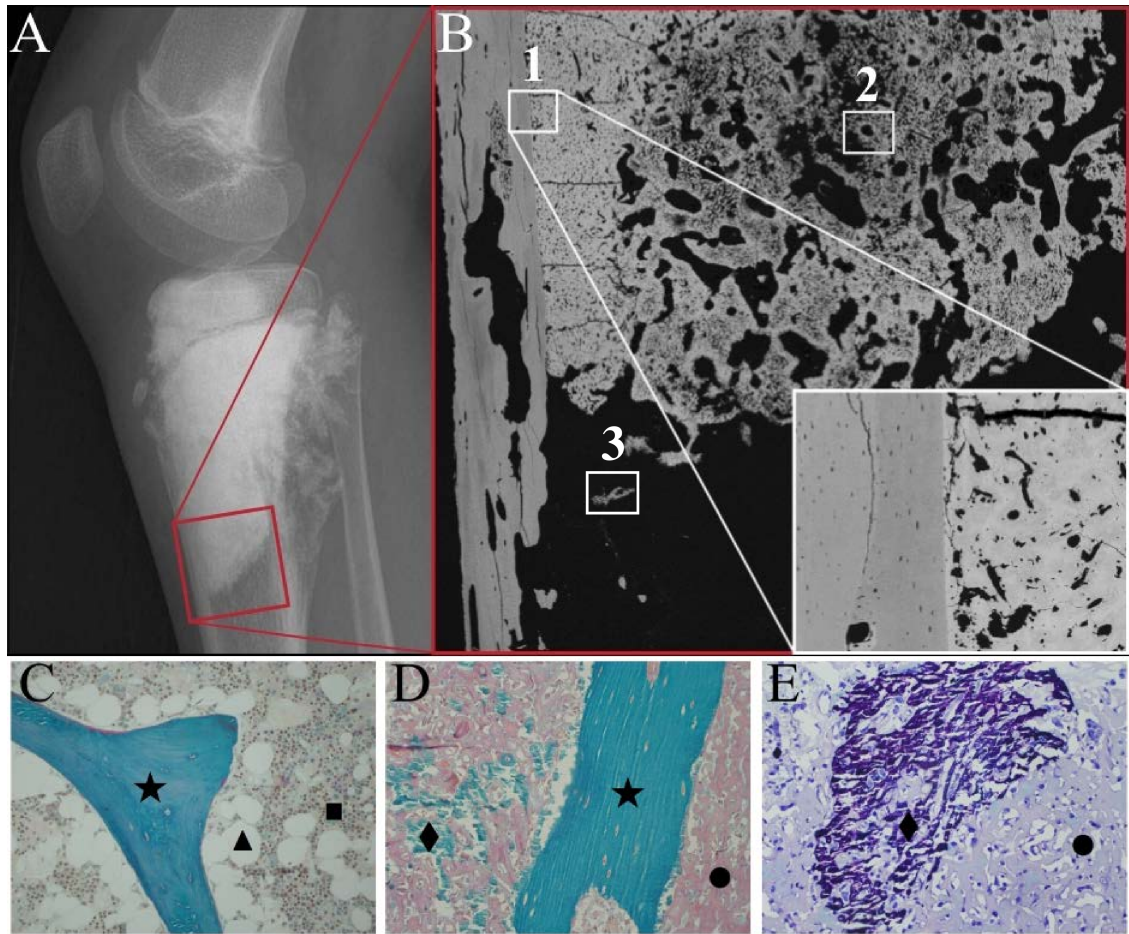


Figure 7.1: Radiograph (A) of a knee joint with a sclerosing osteosarcoma. The red box indicates the region examined by quantitative backscattered electron imaging (qBEI). Backscattered electron image (B) showing an overview of a tissue sample. Two regions of interest (ROIs) selected for consecutive Zn SR- μ XRF-analysis are indicated. ROI 1 contains healthy bone tissue together with a tumor tissue area, which is mineralized to an extremely high percentage. Further the tissue matrix itself is mineralized to a much higher degree than normal bone. ROI 2 contains a tumor tissue area, which is mineralized to a much lower percentage than in ROI 1. Representative histological images of tissue sample sections from the same patient: (C) healthy trabecular bone area with intact bone marrow compartment; modified trichrom Goldner's staining: green mineralized trabecular bone feature (★), brownish bone marrow cells (■) and white fat cells (▲). (D) tumor affected bone tissue: normal trabecular bone (★), non-mineralized (●) and mineralized (◆) tumor matrix, (E) region of mineralized (◆) and non-mineralized (●) tumor matrix (Giemsa staining).

Table 7.1: List of analyzed samples (n is the number of the measured areas, regression grades refer to the histologic grade of regression as defined by Salzer-Kuntschik et al. [76]).

Patient	n	Tissue	Age (years)	regression grade
P1	5	prox. tibia	11	4
P2	5	prox. tibia	12	2
P3	5	prox. femur	66	5
P4	6	dist. femur	18	2
P5	4	dist. femur	18	2
P6	3	dist. femur	17	2
P7	3	prox. tibia	14	3
P8	6	prox. fibula	10	3
P9	4	prox. humerus	10	3

diamond grains (3 μm and 1 μm) using a precision polishing device (PM5, Logitech Ltd., Glasgow, UK). A flat surface of the sectioned tissue area is crucial for qBEI and SR- μXRF measurements. Afterward the sample blocks were coated with a thin carbon layer by vacuum evaporation (Agar SEM Carbone coater, Agar Scientific Limited, Essex, UK) to avoid electrical charging effects during backscattered electron imaging. A more detailed description of the sample preparation can be found in previous publications [44, 52].

7.1.3 Micro XRF measurements

The samples were measured at the FLUO beamline at the ANKA light source with the confocal setup described in section 3.1.1. The step sizes varied between $10 \times 10 \mu\text{m}^2$ and $10 \times 17 \mu\text{m}^2$ for the different beam times. Depth resolution at 9.71 keV ($\text{Au-L}\alpha$) was about 20 μm .

The acquisition time of the μXRF signal per voxel was chosen by the signal to noise ratio of test measurements. For most samples 2 s were sufficient. All spectra were dead time corrected. A typical spectrum obtained in a voxel of a mineralized bone tissue is shown in Fig. 7.2.

7.1.4 qBEI

An example of ROIs, in which consecutively Zn content measurements/mapping were performed, are shown in Fig. 7.1 as well as histological images of tissue sample sections from the same patient and a radiography of the patient's knee joint. The qBEI measurements for one sample (P1) were previously presented in detail as a case study [77]. A significantly higher degree of mineralization (Ca content) was reported in the tumor bone tissue compared to the surrounding healthy bone matrix.

7.1.5 Data evaluation

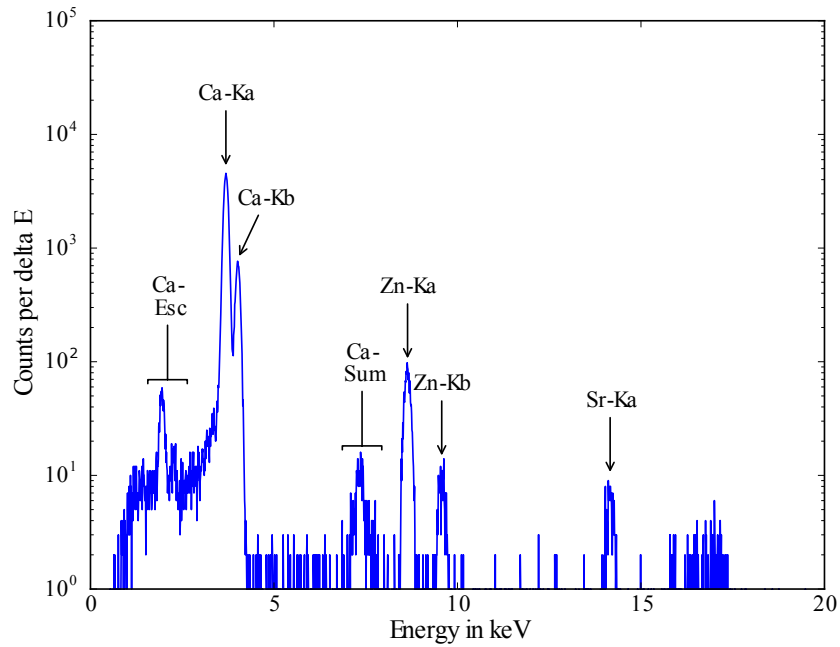


Figure 7.2: Typical SR-μXRF spectrum as obtained from a voxel inside a mineralized bone matrix. Data acquisition time was 3 s per pixel.

The spectra acquired in each voxel were processed using AXIL software [27, 26, 28]. Net counts per Ca, Sr, Fe and Zn were converted to text maps (further referred to as elemental maps).

Custom made software was written in python (v.3.4) [78] for further data processing using the modules: numpy [79], scipy [80] and matplotlib [81]. The following evaluation steps were performed:

1. All elemental maps were normalized to 100 mA ring current and counts per second (cps).
2. No Zn levels were detected in the non-mineralized tumor tissue as well as bone marrow. Therefore we focused our analysis solely on the mineralized tissue areas. We differentiated between tumor tissue and adjacent normal bone, which can be easily distinguished based on the backscattered electron images. As there was no Zn, a threshold was introduced in the Ca maps to clearly segment between mineralized tissue areas and soft tissue areas and/or embedding medium. This was done in an adaptive manner using equation (7.1) for each ROI, because of variations in tissue characteristics and experimental conditions on the synchrotron between the different measurements sessions. A value of 0.5 for “*level*” in equation (7.1) turned out to be a suitable level to evaluate the tissue samples. By this way partially filled volume effects occurring at the edges between the mineralized and adjacent non mineralized regions were minimized. Thus regions around small voids could be excluded from Zn evaluation.

$$T_{Bone} = Ca_{min} + level \cdot (Ca_{max} - Ca_{min}) \quad (7.1)$$

T_{Bone} is the threshold value for the mineralized tissue. All voxels with a lower Ca count rate than T_{Bone} are not included in the Zn map analysis. Ca_{min} represents the minimal Ca count rate of a sample area (ROI). Ca_{max} stands for the maximal Ca count rate in the same ROI. The variable *level* can be assigned any value between 0 and 1.

3. Areas of all samples were classified as tumorous or healthy by inspecting the corresponding qBEI images. For sample areas containing both healthy and diseased tissue such as shown in Fig. 7.3a - 7.3c masks were created as binary images in ImageJ (v1.48o, National Institutes of Health, USA) [82] which then were used by the software to allocate the various pixels of the sample area to healthy bone and to tumor tissue.

4. The relative Zn content of a voxel was defined as the fraction of the Zn count rate from the total count rates of Ca (Counts_{Ca}) and Zn (Counts_{Zn}) together (equation 7.2).

$$Zn \text{ fraction} = \frac{Counts_{Zn}}{Counts_{Ca} + Counts_{Zn}} \quad (7.2)$$

5. Mean, standard deviation, 5-percentile, 25-percentile, 50-percentile (= median), 75-percentile and 95-percentile of the Zn fraction data were determined for each sample area (ROI) as well as for each sample.
6. Frequency distributions of voxels with certain Zn fraction values were plotted (Zn histograms).
7. Boxplots showing the median (black horizontal line), mean (black square), a colored box starting at the 25th percentile and ending at the 75th percentile (containing 50% of the data) and whiskers reaching from the 5th to 95th percentile (and therefore representing a 90% confidence interval) were created.
8. Moreover we investigated if the Zn concentration differs with respect to the calcium content in highly versus lowly mineralized areas.

7.1.6 Statistical analysis

Statistical comparison was performed between the groups of median Zn fraction of healthy bone tissue versus tumor tissue. Since healthy and tumor tissue was measured from the same sample a paired test was appropriate. Further due to the small sample size it would be unreasonable to assume normal distribution of the measured data, thus a Wilcoxon signed-rank test was performed using tabulated critical values [83]. We correlated the Zn fractions of each tumor to the Salzer-Kuntschik regression grade [76] in order to see if there is a relationship between the Zn levels and chemotherapy response.

7.2 Results

7.2.1 Zinc

As an example, three ROIs within the sample from patient P1 are shown in Fig. 7.1.

ROIs with different tumor characteristics were selected and resulting Ca count rates and Zn fraction maps with corresponding histograms were determined. The ROI 1 contains both tumor tissue and healthy bone: the classification of the regions is given in the qBEI image (Fig. 7.3a), one can see that the mineralization and accordingly also the Ca content are distinctly lower in the healthy part than in the tumor area (Fig. 7.3b). In parallel the Zn fraction was significantly increased in tumor area compared to the healthy bone area (Fig. 7.3c).

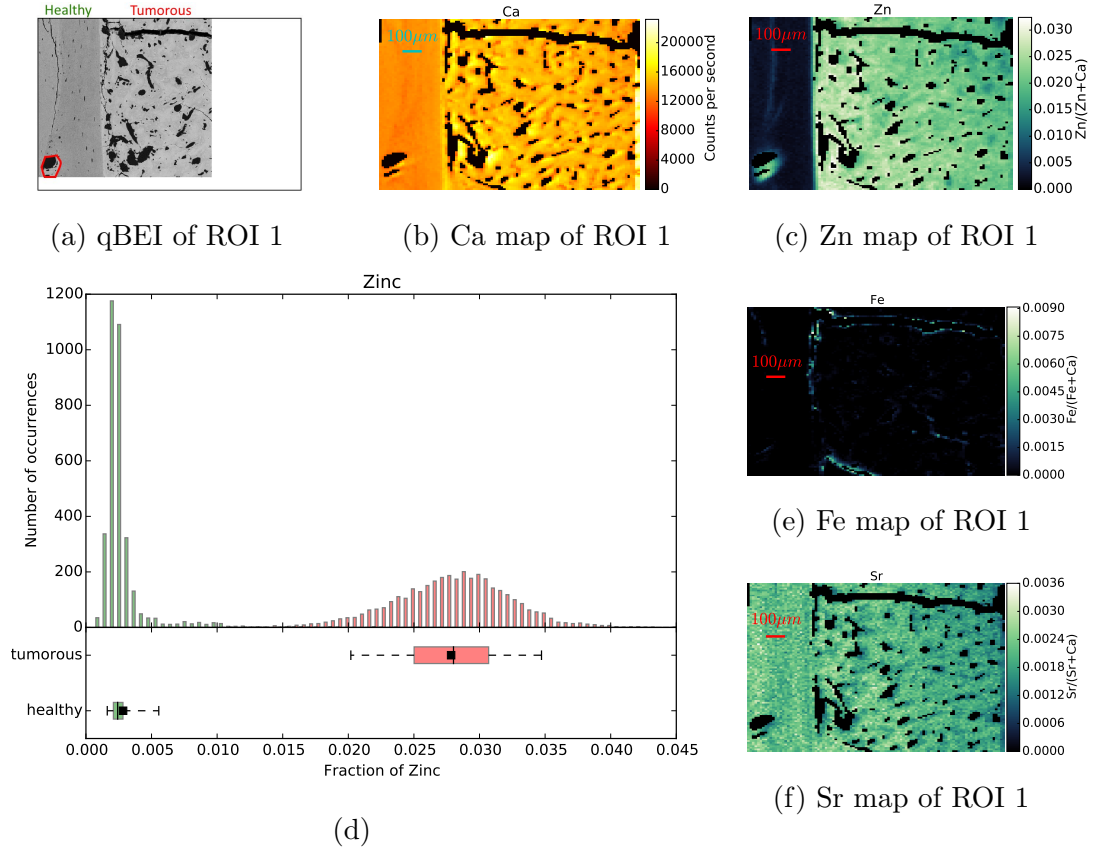


Figure 7.3: Example of confocal synchrotron radiation micro X-ray fluorescence (SR- μ XRF) analysis in ROI 1 (Fig. 7.3a - 7.3c) of a mineralized tumor tissue from patient P1: The qBEI (quantitative backscattered electron imaging) is reflecting the mineral content where Ca and Zn mapping was performed (Fig. 7.3a). Units in Ca map (Fig. 7.3b) are given in counts per second (cps), Zn map (Fig. 7.3c) units are given as fraction of Zn count rates per total (Ca+Zn) count rates. Fig. 7.3d shows the distribution of these Zn fractions (healthy pixels in green, tumorous in red) as a histogram and in boxplots (black square - mean value, black line - median, colored box - 50% of the data from 25 to 75 percentile, whiskers - 90% of the data from 5 to 95 percentile).

The qBEI, Ca map and Zn fractions map of ROI 2 (Figs. 7.4a - 7.4c) show an area containing exclusively tumor tissue.

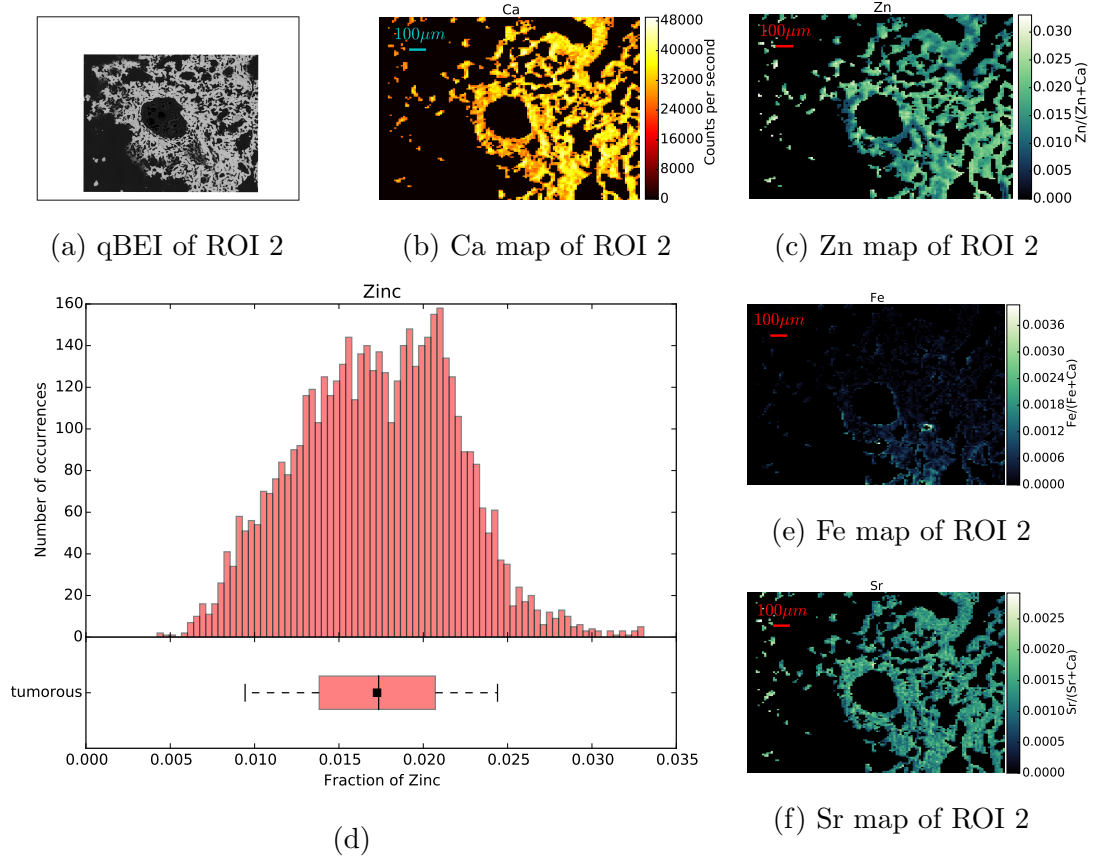


Figure 7.4: SR- μ XRF analysis of ROI 2 (Fig. 7.4a - 7.4c) of a mineralized tumor tissue from patient P1: The qBEI is reflecting the mineral content where Ca and Zn mapping was performed (Fig. 7.4a). Ca map (Fig. 7.4b) is given in counts per second (cps), Zn map (Fig. 7.4c) units are given as fraction of Zn count rates per total (Ca+Zn) count rates. Fig. 7.4d shows the distribution of these Zn fractions as a histogram and a boxplot.

Figs. 7.5a - 7.5c show qBEI, Ca map and Zn fractions map of ROI 3 show an area also containing exclusively tumor tissue, which is mineralized to a much lower percentage than ROI 1 and ROI 2.

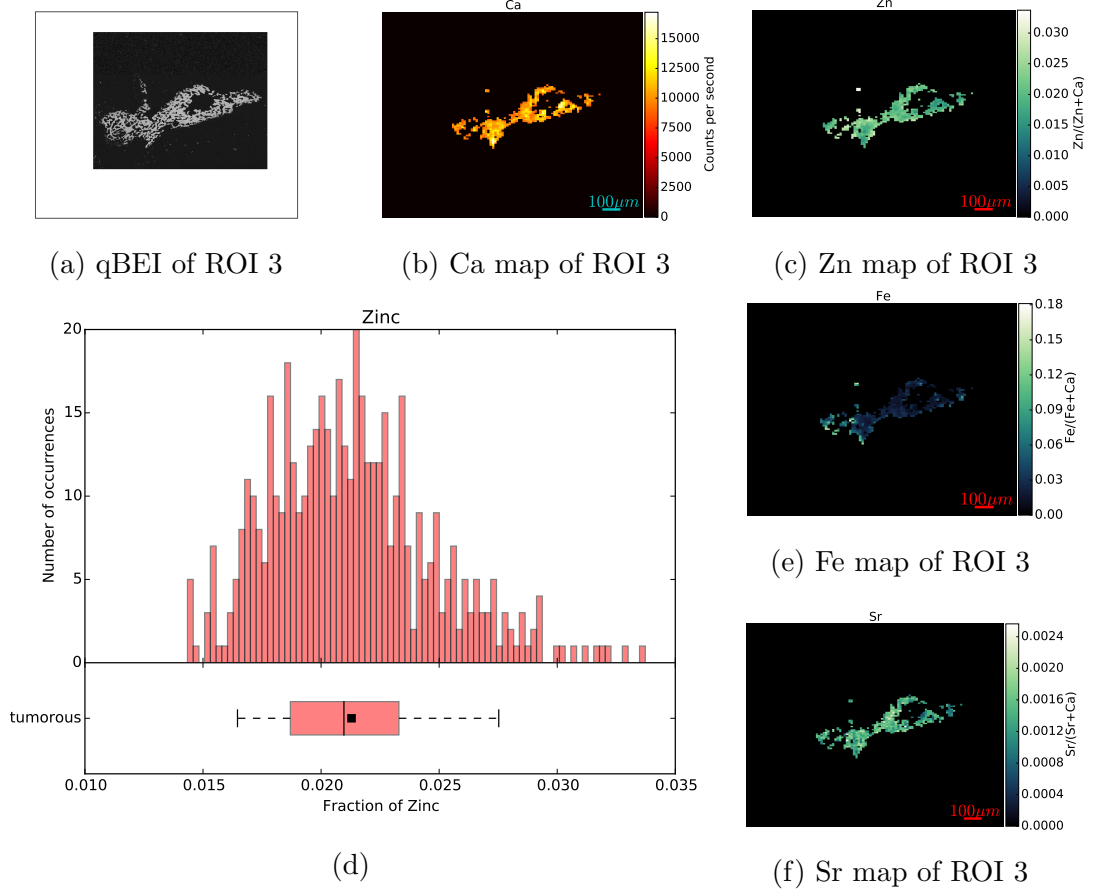


Figure 7.5: SR- μ XRF analysis of ROI 3 (Fig. 7.5a - 7.5c) of a mineralized tumor tissue from patient P1: The qBEI is reflecting the mineral content where Ca and Zn mapping was performed (Fig. 7.5a). Ca map (Fig. 7.5b) is given in counts per second (cps), Zn map (Fig. 7.5c) units are given as fraction of Zn count rates per total (Ca+Zn) count rates. Fig. 7.5d shows the distribution of these Zn fractions as a histogram and a boxplot.

The histogram of Zn fractions of all 5 ROIs of P1 is shown at once in Fig. 7.6. Two separated peaks (green bars healthy and red bars tumorous region) are visible. Boxplots for the same data set are also shown in Fig. 7.6 (underneath the histogram). The 90% confidence intervals of the healthy and the tumorous areas are distinctly separated. Only a few outliers of those two distributions overlap.

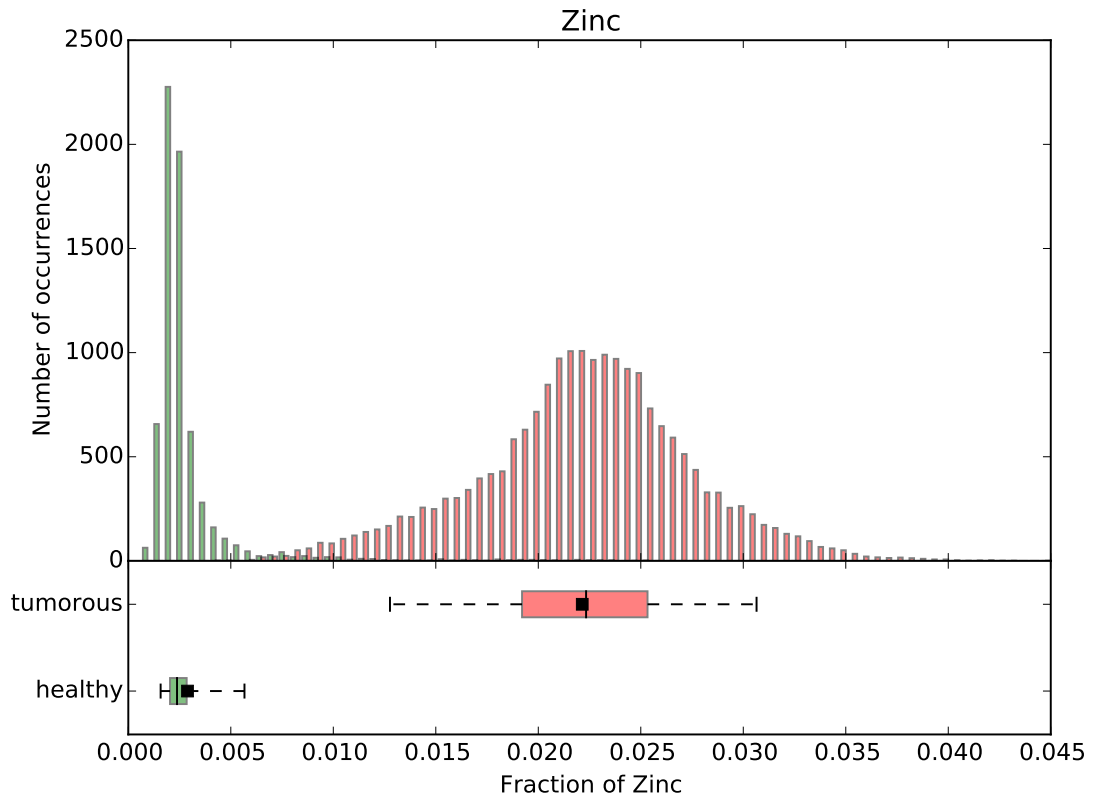


Figure 7.6: Histogram and boxplots for the Zn fractions over all the healthy (green) and tumorous (red) areas of P1

Figure 7.7 compares the Zn fraction distribution for healthy and tumorous tissue areas of all patients. The histograms were normalized so that the data of each patient contribute equally and independently of the number of points measured per patient. As one can see, the Zn fraction distribution of the healthy and tumorous areas are clearly separated, and Zn content in the tumorous areas is a lot higher in the osteosarcoma tissue compared with the surrounding healthy tissue.

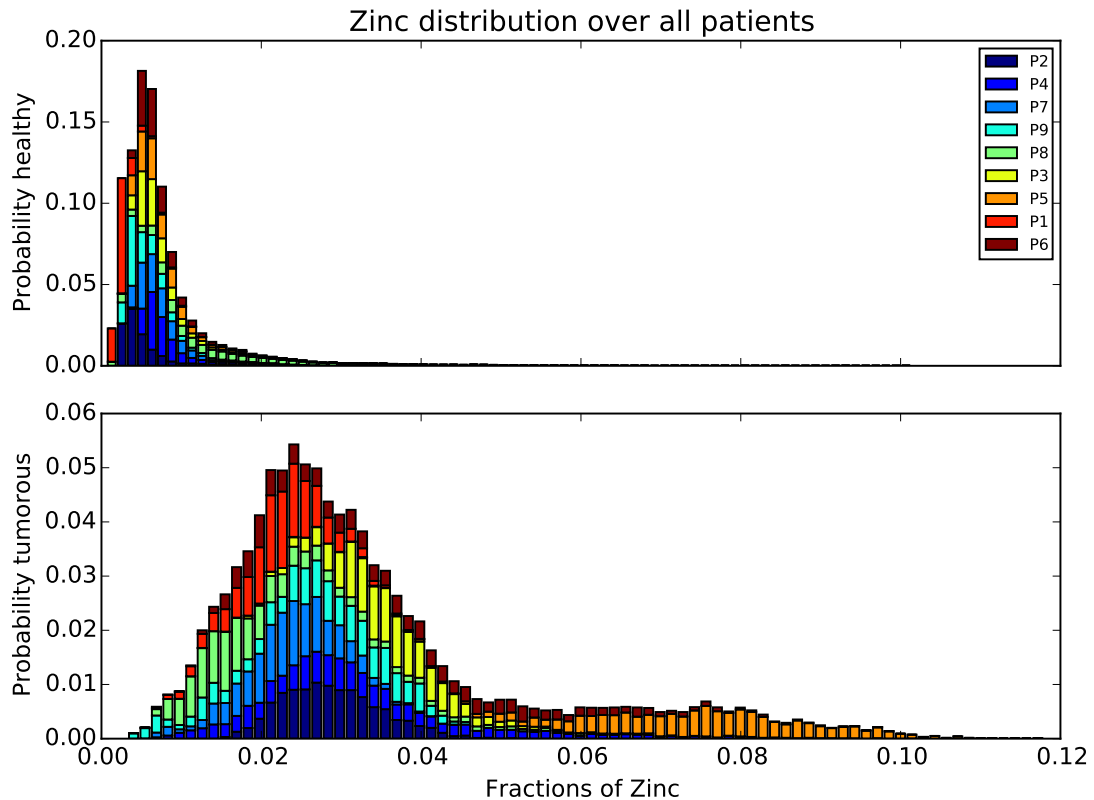


Figure 7.7: Zn fraction distribution over all patients for healthy (top) and tumorous areas (bottom). The distributions were normalized so that each patient contributes equally to the histogram (independently of the numbers of points measured by patient).

Zn fractions with their means and standard deviations over the healthy and the tumor regions of the nine patients are shown in Fig. 7.8. As one can see, the Zn mean values for the tumorous regions of a patient are always higher than those for the healthy regions.

The Wilcoxon signed-rank test showed that the median of the tumorous areas of a patient is significantly higher ($p < 0.005$) than the median of the healthy areas of the same patient.

The average of the median ratios (tumorous Zn fractions median divided by healthy Zn fractions median) of all nine patients and its standard deviation can be reported as 6.05 ± 3.02 . While the weighted mean for the nine Zn fraction

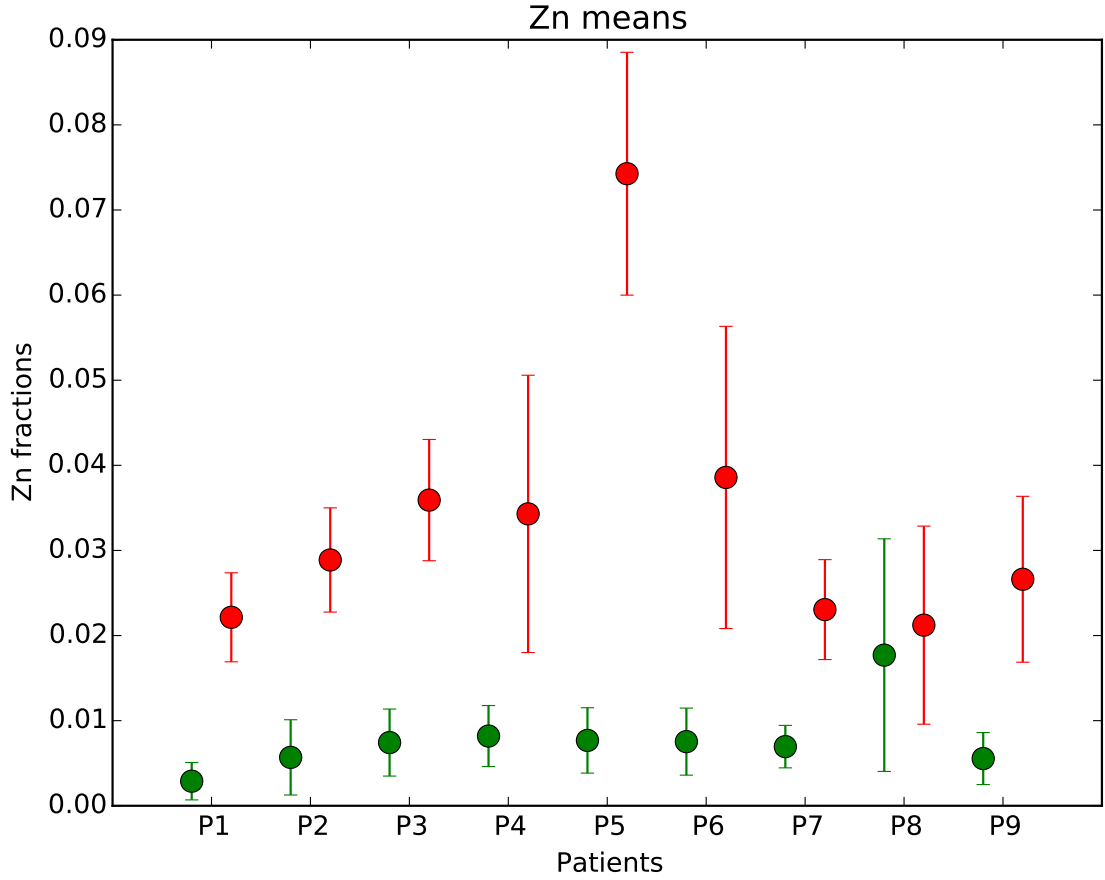


Figure 7.8: Comparison of Means and Standard deviations of Zn fractions between healthy bone (green circles) and mineralized tumor (red) matrix for each patient

ratios (mean of tumorous Zn fractions divided by the mean of healthy Zn fractions) and their standard deviations results to 3.67 ± 0.12 . As one can see from both the weighted average and average of the median ratios, the Zn count rate in the tumorous areas of the samples is at least about four times higher than that in the healthy areas of the samples.

Furthermore, we did not find a significant difference in $\frac{Zn}{Zn+Ca}$ ratio in lowly versus highly mineralized tumor areas indicating this ratio is relatively unchanged.

Both mean and median of Zn fractions were compared to the histologic grade of regression for each patient. No correlation between Zn fraction values and grades of regression were found, indicating that Zn-levels did not correlate with the response to chemotherapy.

7.2.2 Iron and Strontium

As a lot of scanned pixels in the mineralized tissue showed no presence of iron (as can be seen in the spectrum in Fig. 7.2) either because the region contains no iron or because its concentration is below the detection limit. This can also be seen by looking at the histograms and boxplots over all healthy and tumorous areas (see Fig. 7.9), which shows that in an overwhelming majority of the measured mineralized tissue areas the Fe content is below the detection limit.

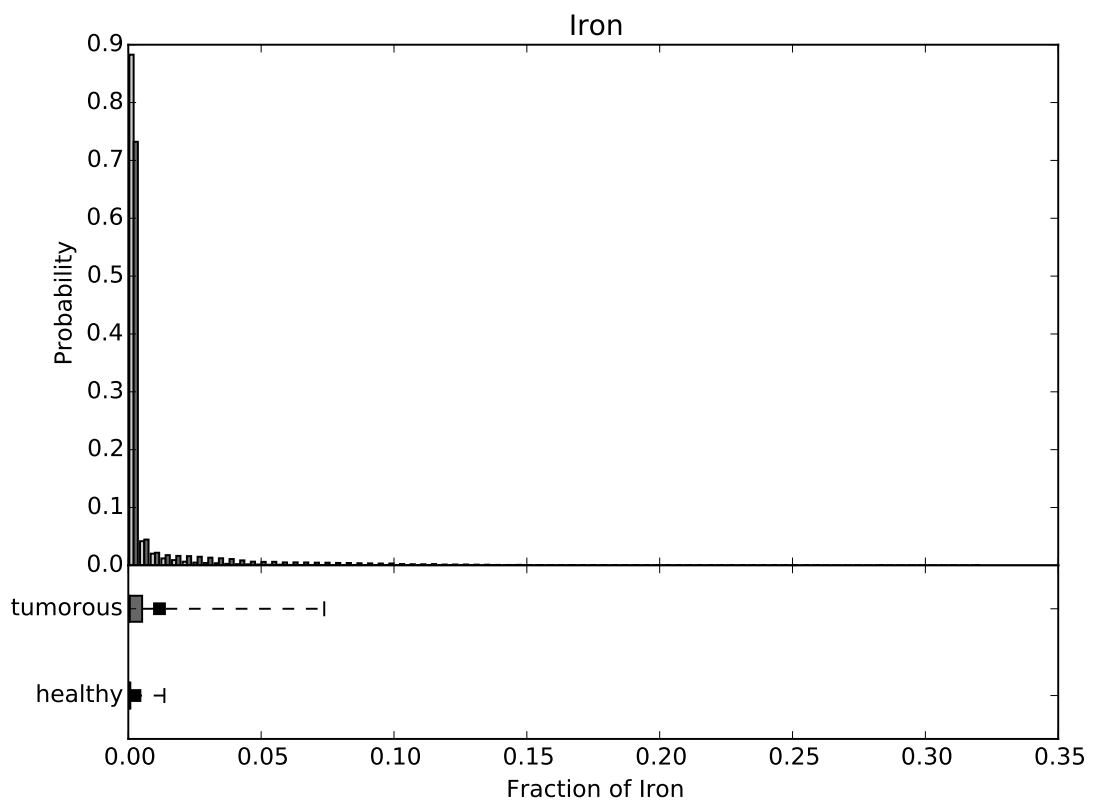


Figure 7.9: Histogram and boxplots for the Fe fractions over all the healthy (light gray) and tumorous (dark gray) areas of all samples. The histogram was normalized so that data from each patient contributes equally.

Sr was found in all mineralized areas which means that the Sr distribution was similar to the Ca distribution. The comparison of the Sr fraction in healthy and tumorous areas is presented in Fig. 7.10. As one can see from this figure, the

normalized to the Ca content, there is no difference in Sr distribution between healthy and tumorous areas.

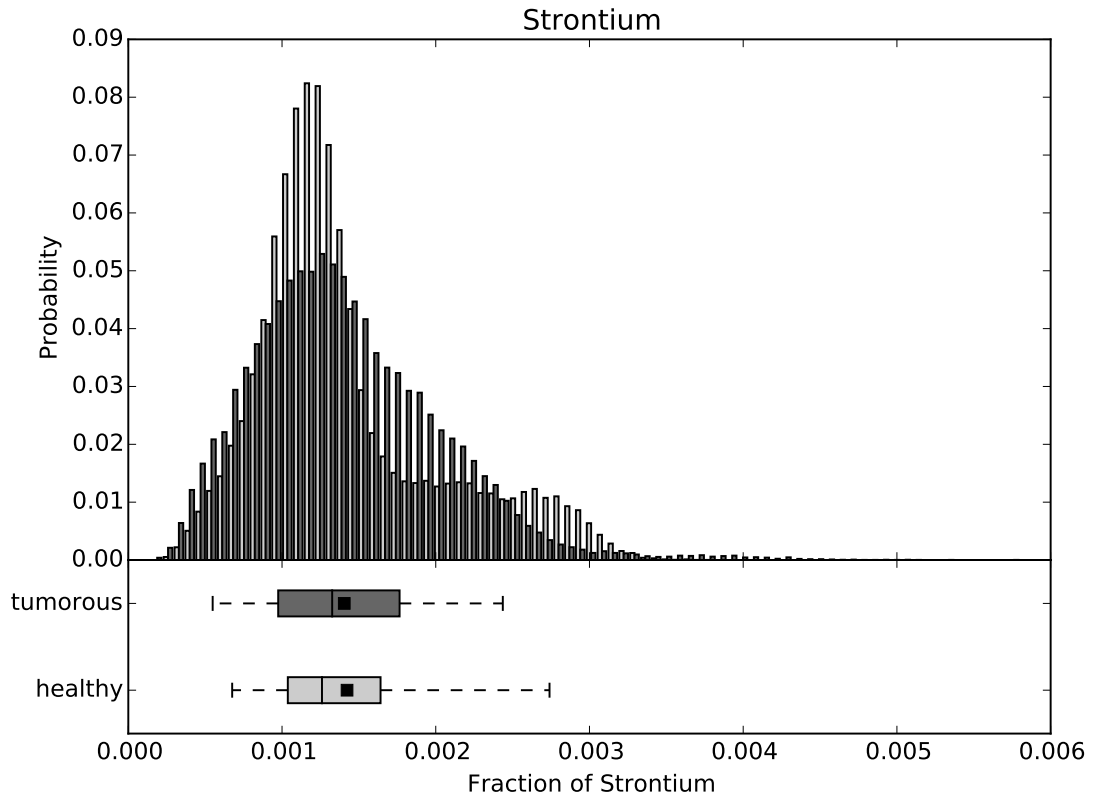


Figure 7.10: Histogram and boxplots for the Sr fractions over all the healthy (light gray) and tumorous (dark gray) areas of all samples. The histogram was normalized so that data from each patient contributes equally.

The same conclusion can be drawn from the comparison of healthy and tumorous Sr fractions for each sample (Fig. 7.11).

To easily compare the results for Fe, Sr and Zn, the minimum, maximum as well as the 5, 25, 50 (median), 75 and 95 percentile of their element fractions are given in table 7.2.

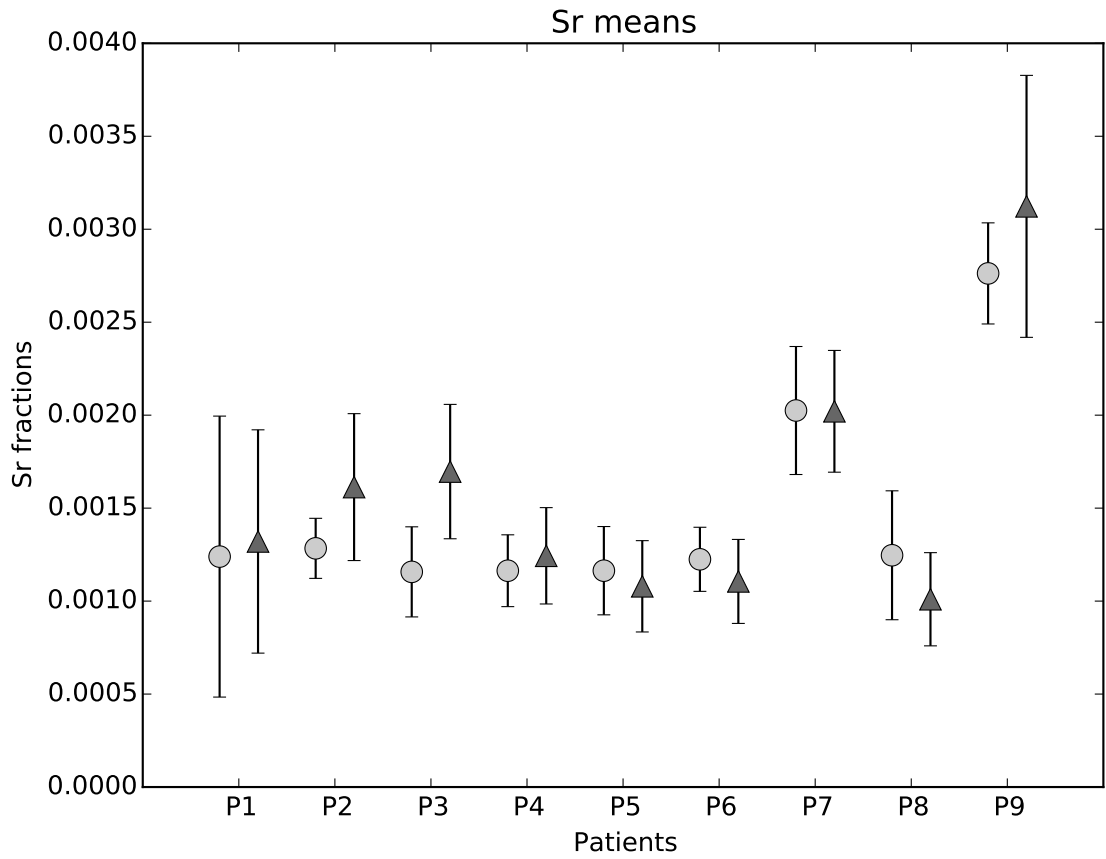


Figure 7.11: Comparison of Means and Standard deviations of Sr fractions between healthy bone (light gray circles) and mineralized tumor (dark gray triangles) matrix for each patient

Table 7.2: Results for Fe, Zn and Sr in over all healthy (H) and tumorous (T) areas. The minimum and maximum of the element fractions as well as the 5, 25, 50 (median), 75 and 95 percentile are given.

	Min	Max	5 %	25 %	50 %	75 %	95 %
Fe _H :	0.0000	0.152	0.0000	0.0001	0.0003	0.0008	0.014
Fe _T :	0.0000	0.321	0.0000	0.0001	0.0006	0.0052	0.074
Zn _H :	0.0007	0.101	0.0021	0.0040	0.0060	0.0085	0.021
Zn _T :	0.0033	0.118	0.0126	0.0199	0.0243	0.0310	0.059
Sr _H :	0.0002	0.004	0.0007	0.0010	0.0013	0.0016	0.003
Sr _T :	0.0002	0.006	0.0005	0.0010	0.0013	0.0018	0.002

7.3 Discussion

Synchrotron radiation induced confocal μ XRF was used to evaluate trace elements in human osteosarcoma tissue. The study revealed tremendously higher Zn level in mineralized osteosarcoma regions compared to the healthy bone areas of the same patient. On average the Zn fraction median for tumorous bone areas was 6 times higher than for healthy bone areas. In our samples, we found regions with varying fractions of mineralized tumor tissue areas. Interestingly, we did not find a significant difference in $\text{Zn}/(\text{Zn}+\text{Ca})$ ratio between tumor areas with a low or a high fraction of mineralized tissue indicating that this ratio is relatively constant.

Changes in Zn levels have been observed in connection with various cancer types. For instance Christudoss et al. reported decreased levels of mean tissue Zn (83% and 61%) and plasma Zn (27% and 18%) compared to controls in benign prostatic hyperplasia and prostate carcinoma [2]. Zn concentration was also found to be significantly decreased in serum for liver cancer compared to that in normal serum [72]. The same study also reported lower Zn tissue concentrations in cancerous and non-cancerous livers of hepatoma patients compared to normal livers. A meta-analysis of tissue and serum Zn in epithelial malignancies [69] confirmed the decrease of serum Zn levels in lung, breast, liver, stomach, and prostate cancers and Zn tissue levels in prostatic, liver, lung, and thyroid cancer. A clear increase of Zn was only found in cancerous breast tissue. Moreover, the results of Al-Ebraheem et al. [74] imply an interrelation between the sites of cancer cell clusters and higher concentrations of Zn, Fe, Cu and Ca in breast tissue.

In our study, we did not see a significant correlation between the Zn fraction values and the response to chemotherapy.

The mechanisms underlying the changes in the Zn concentration between healthy and tumorous mineralized tissue can only be speculated about at this time. As Zn stimulates bone formation [56, 5] higher Zn levels in mineralized tumor tissue compared with healthy mineralized tissue seem perspicuous. Zn is an essential trace element implicated in several biological processes including bone metabolism [4]. Zn ions are used by many proteins to stabilize their structure. E.g. Zn finger proteins are among the most abundant proteins in eukaryotic genomes. Many of them are involved in transcriptional regulation [84]. Moreover, Zn is also a co-factor of several enzymes in bone such as the tissue non-specific alkaline phosphatase, which plays an important role in bone matrix mineralization [85, 86].

In a recent study we found homogenous Zn concentration within bone structural units while increased Zn concentrations were observed in the cement lines separating the differently aged bone structural units [35]. Interestingly, the Zn concentration was not correlated with the degree of bone matrix mineralization in the different bone structural units, which suggests that Ca is not a significant factor for explaining the Zn concentration in bone and that Zn is therefore likely under homeostatic control [87]. Zn in the mineralized bone matrix is bound to hydroxyapatite very likely during the early phase of the mineralization process [88]. It seems that Zn is not just incorporated by ion exchange, but by substitution of vacancy-defects of Ca^{2+} [89].

However it is noteworthy that no Zn was found in the surrounding soft tumor tissue. As it cannot be entirely ruled out that Zn in soft tissue is lost during sample preparation, cryosections should be analyzed in future studies.

Furthermore, it should be mentioned that our samples were taken after chemotherapy. While it is known that chemotherapy of osteosarcomas has limited effect on the tumor mineralization [90] we do not know if the chemotherapy-induced necrosis has any influence on Zn levels.

Ambroszkiewicz et al. investigated serum bone turnover markers [91], such as bone alkaline phosphatase (BALP) which contains Zn as co-enzyme [92], in children and adolescents with osteosarcoma. Their findings suggest that BALP levels decrease (from levels similar to healthy patients) during pre-operative chemotherapy for all patients and significantly lower values for patients with good prognosis compared to patients with poor prognosis during post-operative chemotherapy and after therapy were found [91]. Another study [93] was reported to have found no significantly different serum Zn values in patients with osteosarcoma compared to age and sex-matched controls. Future studies combining measurements of Zn distribution in mineralized healthy and tumorous tissue of osteosarcoma patients as well as of BALP values and serum Zn levels at different stages of the treatment could provide new insights into the role of Zn in osteosarcoma.

Due to the complexity of bone structure there is no acceptable reference material for calibration of the μXRF setup available which would allow to quantify the absolute trace element concentrations corresponding to the measured count rates. While higher count rates equate higher concentrations no absolute values (wt%), but only relative values (fractions), can be given. As the osteosarcoma tissues are

not easy to acquire the sample size was rather small ($n=9$). Heterogeneity of the samples exists concerning age, sex, localization (location of sampling), histological specification and treatment with different types of chemotherapy.

7.4 Conclusion

Using Synchrotron radiation induced confocal μ XRF, we were able to show for the first time that Zn concentrations in mineralized osteosarcoma tissue are higher than in normal adjacent bone. However the underlying mechanism of Zn accumulation remains unclear. Given the emerging data on other types of cancer and trace elements, future studies will need to take a closer look at the role of trace elements and the clinical outcome of osteosarcoma. Our findings of increased Zn levels warrant further studies on the role of Zn and bone cancer.

8 Trace elements in the tidemark

This chapter will be published in a scientific journal.

The tidemark is a very narrow structure between non-calcified and calcified articular cartilage. It is an active or resting calcification front. It is not well defined but is suspected to have a part in some cartilage diseases such as osteoarthritis. In previous μ XRF measurements [33] with lower resolution (beam size about $20\text{ }\mu\text{m} \times 14\text{ }\mu\text{m}$) it was found that Zn and Pb are accumulated in the tidemark region. However, as the tidemark was suspected to be thinner than the diameters of the used X-ray beams, the results would be smeared over a larger volume. This means that if the tidemark is thinner, the true levels would be underestimated.

Depending on how high the Pb and Zn levels in the tidemark are, it might be possible that during joint erosion (for example in osteoarthritis patients) the systemic levels of Zn and Pb might increase to values of medical relevance.

To gain a better insight into the accumulation of Zn and Pb in the tidemark, its structure and different element levels compared to the mineralized cartilage, we measured the elemental distribution in thin bone samples from 5 different patients.

8.1 Materials and methods

8.1.1 Patients

Bone material from five patients was available. Those bone tissue samples were dehydrated and fixed in a gradient of ethanol concentration (50-100%) and afterwards fixed in PMMA. Then, six $3\text{ }\mu\text{m}$ thick cuts were prepared with a microtome. Each of those slices was put between two $8\text{ }\mu\text{m}$ thick Kapton foils and fastened to plexiglas frames. During the measurements the samples were fixed to a 3D-printed samples carrier so that the frame opening would overlap with the hole in the sample carrier.

Table 8.1: List of measured tidemark samples.

Patient	Section	Block	Tissue
P1	TM1	CY6	femoral head, osteoporotic
	TM6		
P2	TM2	CY10	femoral head, osteoporotic
P3	TM3	CY13	femoral head, osteoporotic
P4	TM4	ON10	femoral head, osteonecrosis
P5	TM5	ON16	femoral head, control

8.1.2 Submicro XRF measurements

The samples were measured at the B16 beamline at the Diamond Light source with the setup described in section 3.1.3. The beam size was about $500 \times 800 \text{ nm}^2$. To find the tidemark area on the samples and to correlate the measured areas with the microscope images of the samples, rather big sample regions were roughly scanned ($1 \text{ }\mu\text{m}$ step size, 1 s measurement time per point). Step size and sample area size were further reduced until a reasonable sized region for the high-resolution scan was found (see Fig. 8.1a and 8.1c). For each sample this high-resolution scan (with $1 \text{ }\mu\text{m}$ step size) was recorded around the tidemark region. These scans were performed with a measurement time of 20 s per point (see Fig. 8.1d - 8.1f).

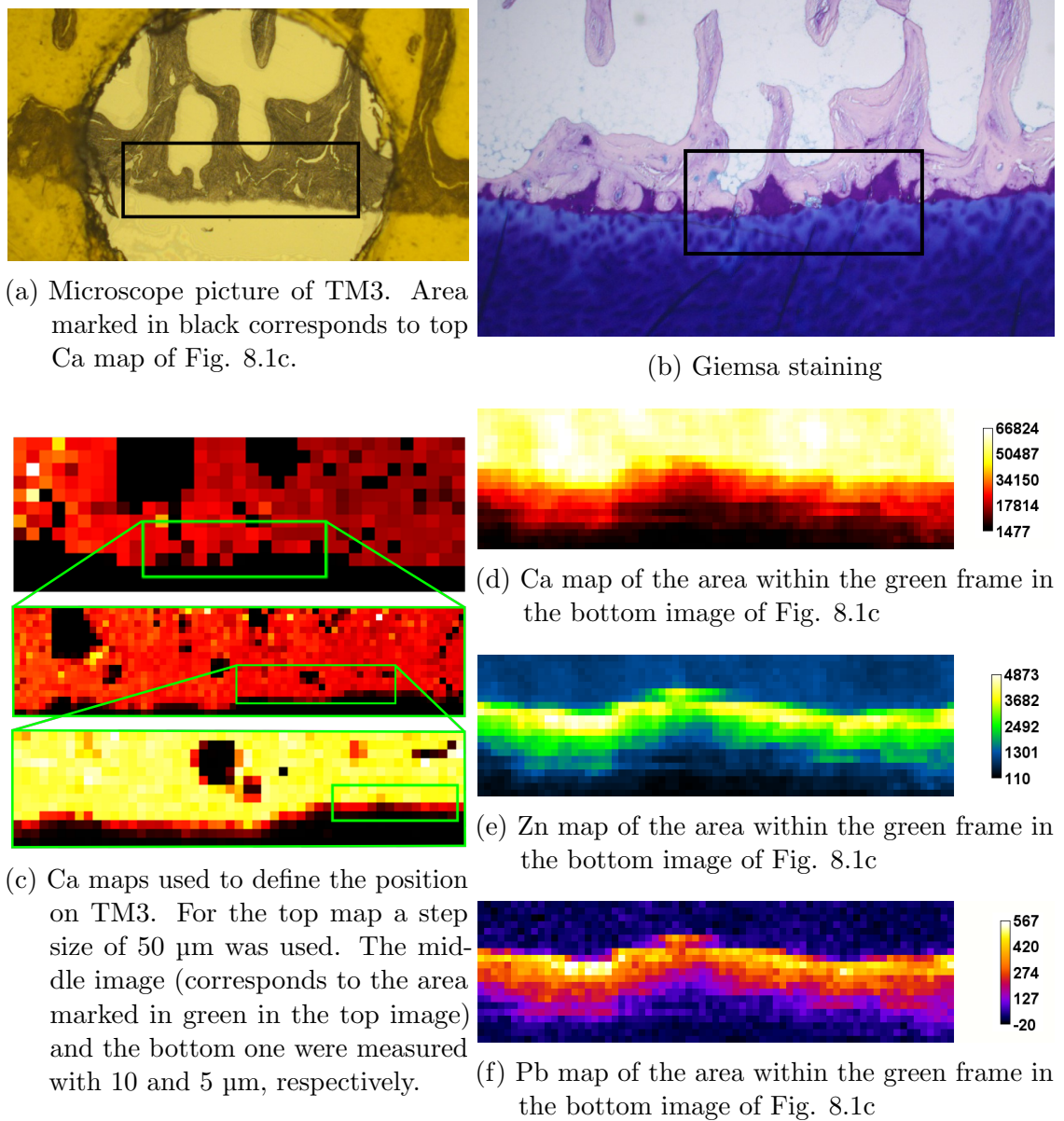


Figure 8.1: Microscope picture (a) of a measured sample (P3, TM3) and Giemsa staining (b) of a consecutive cut of the same sample. Area marked by the black frame indicates the position of the overview scan.

In the staining: Light violet - bone; dark violet - mineralized cartilage; blue - non-mineralized cartilage; dark blue circles in blue area - chondrocyte lacunae.

Ca maps (c) used as overview pictures to define the position on the sample. For all 3 maps: 1 s measurement time/pixel.

Fine scan of the tidemark region (d): Ca (top), Zn (middle) and Pb (bottom) distribution. Measurement time: 20 s/pixel. Step size: 1 μm .

8.2 Data evaluation

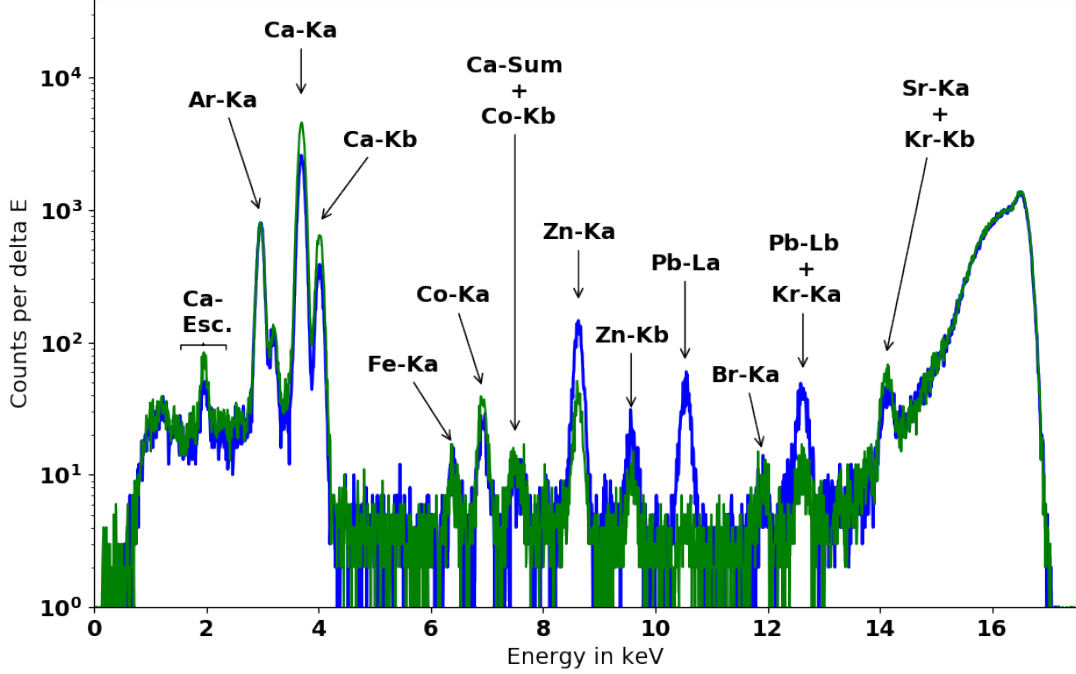


Figure 8.2: Typical submicro XRF spectra obtained from a point in the mineralized matrix (green) and a point in the tidemark region (blue). Measurement time was 20 s for each point.

The spectra acquired in each point were processed using AXIL software [27, 26, 28]. Net counts per Ca and Zn were converted to text maps (further referred to as elemental maps). Additionally, also the standard deviation of the fit of each elements were converted into text maps. Typical submicro XRF spectra for the mineralized matrix and the tidemark region are shown in Fig. 8.2.

Custom made software was written in python (v.3.4) [78] for further data processing using the modules: numpy [79], scipy [80], matplotlib [81] and lifelines [94].

8.2.1 Identifying the tidemark

The following evaluation steps were performed to find the single and double tidemarks within the elemental maps:

1. To find the tidemark within the Zn and Pb map the data from the Ca, Zn and Pb maps as well as their standard deviations are loaded into the program.
2. The median of the first 5 points of all lines within a Ca map are used to represent the Ca level in the mineralized matrix ($Ca_{mineralized}$). The median of the last 5 data points of each line are used to determine the Ca level outside of the mineralized matrix ($Ca_{non-min.}$). As border between the mineralized and the non-mineralized tissue the following value was defined:

$$Border = Ca_{non-min.} + 0.5 \cdot (Ca_{mineralized} - Ca_{non-min.}) \quad (8.1)$$

3. Using the Savitzky-Golay filter [95] of the scipy module, the data of the Zn and the Pb maps are smoothed line-by-line and the first derivative is estimated to identify the local extrema. Extrema were saved and it was determined if they were minima or maxima. Extrema were only considered to be of interest if the value of positive or negative elevation between them was bigger than 3 times the standard deviation of the extrema. This restriction is needed otherwise statistical fluctuations are registered as extrema. A peak was defined as two minima with a maximum in-between them. An exception was made for negative elevations in the beginning of a line. For such an elevation to be considered as part of a peak it needed to be greater than or equal to 5 times the standard deviation. Position of the minima were saved as limits for the search of the actual peaks. The higher value of two consecutive minima was considered the baseline of the peak.
4. Using the position of two consecutive minima in the smoothed data the maximum (height and position) in-between those minima is determined in the unfiltered data. Using the baseline and the height, the full width at half maximum (FWHM) of the peak is calculated. It should be noted that due to the pixel dimensions an exact determination of the FWHM is not possible.
5. At this point all peaks within the Zn and the Pb maps were determined line-by-line. To identify the tidemark, those peaks need to be more or less at the same position over multiple lines. Therefore, a peak was accepted as part of a specific tidemark if the position of its FWHM somewhat overlapped with

the FWHM of the previous or following line. Peaks which did not satisfy this condition were considered to be part of another possible tidemark.

6. After identifying all potential candidates, all tیدemarks shorter than 5 lines were removed from further consideration. This step was done to exclude possible hotspots.

As an example of the obtained information about the tidemark from this program see the results of P3 (TM3) in Fig. 8.3.

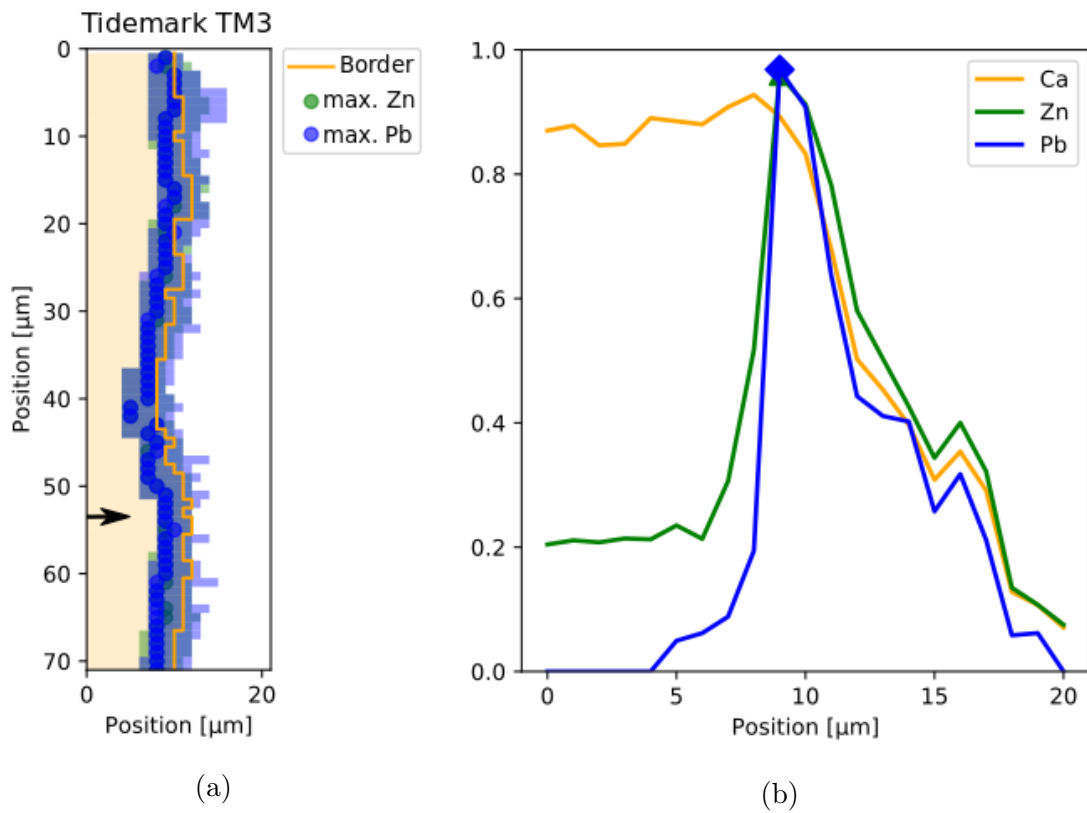


Figure 8.3: (a) Mineralized matrix (light yellow), the border between mineralized and non-mineralized matrix (yellow line), position of the peak maximum for Zn (green dots) and Pb (blue dots) as well as the FWHM for both Zn and Pb (in semi-transparent green and blue, respectively) of TM3. (b) Ca, Zn and Pb signal (each normalized so that their maximum counts within the scan reach 1) of line 53 (marked with a black arrow in (a)) of scan TM3.

Savitzky–Golay filter

The Savitzky-Golay filter is a data smoothing method based on a least-squares polynomial approximation [96]. It works by dividing the data point into equal sized sections (called window length) which are fitted separately with n^{th} order polynomials (in this work n was chosen to be 2) and which will meet at their junction points (continuity). Contrary to conventional cubic spline smoothing, the filter has a better performance in approximating sharp peaks as the derivatives at the junction points are not forced to be equal. Therefore, sharp peak heights are less distorted. Additionally, the filter provides an estimation for the signals derivatives. [96, 95]

8.2.2 Kaplan-Meier Estimation

As the measurements were optimized to obtain a good Zn signal, a lot of scanned pixels showed no presence of Pb either because the regions contained no Pb or because their concentrations were below the detection limit. As the information about Pb is unavailable on the side of the lower concentrations (which are usually displayed on the left side in plots), the data is left censored. The calculation of mean and standard deviation is not possible for censored data. Ignoring the pixels without Pb in the mean calculation would overestimate the Pb content. The calculation of the mean value might underestimate the Pb content, if one assumes that all pixels that show no presence of Pb do not contain any Pb. Therefore, a different evaluation method is needed. As the quantiles (including the median) are stable location measures, they are suitable parameters to compare samples as long as they are not themselves below the censor level.

M. Pajek et al. have previously shown that the Kaplan-Meier approach can be used to estimate the cumulative distribution function from censored XRF data fairly accurately [97]. The cumulative distribution function gives the probability that a data set assumes a certain value or less. For the highest value in a data set the probability is always 1. As the median is defined as the value where half of the data set has values smaller than the median and half the data set has values greater than the median it can be found at the probability of 0.5 in a cumulative distribution function.

The Kaplan–Meier (KM) method (also known as the product limit estimator) was originally developed to assess survival rates, when including incomplete observations

(e.g. lost contact with patients). Nowadays, it is a non-parametric standard way to describe patient survival in medical research. [98, 99] At the time of the evaluation of the data, some events might not yet have happened (death of a patient in a survival study), in this case one deals with right censored data. If the data of the left side of a scale such as the lower concentrations (below the detection limit) in XRF measurements are unknown, this is called left-censorship. The KM algorithm creates a curve very similar to an empirical cumulative distribution function. If there are no censored values, the KM curve becomes the empirical cumulative distribution function.

The Kaplan-Meier estimator can easily be implemented in a python program by using the lifeline module [94].

As a quick example of the cumulative distribution function, three (not censored) data points sorted from lowest to highest value (see Fig. 8.4a) can be assumed. For those data points, the cumulative distribution looks like Fig. 8.4b showing the intensity of the data points (counts) on the x- and the probability of the data on the y-axis. The probability of the sum of all data points is 1. The data points are added cumulatively to the graph, therefore the highest data point is located at 1. As the smallest data point in the example is 3, the probability in Fig. 8.4b for values below 3 is zero. The median (5) is located at 50% probability.

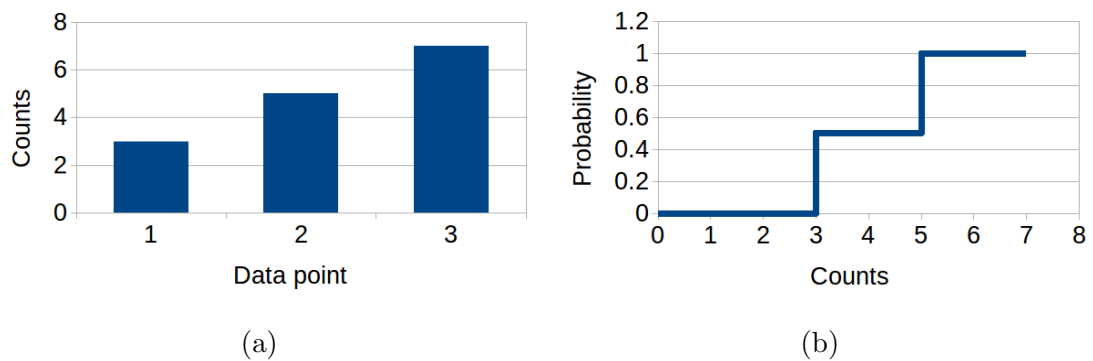


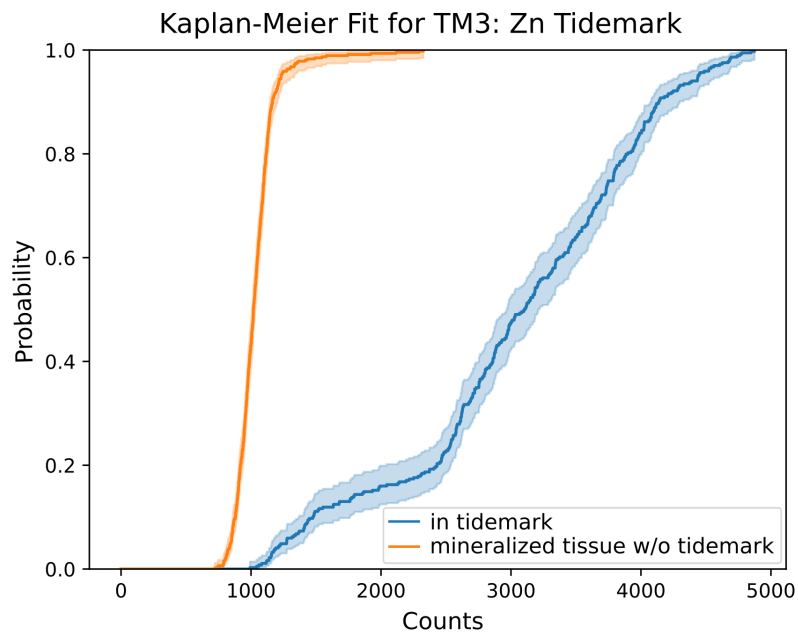
Figure 8.4: Example for a cumulative distribution function.

8.3 Results

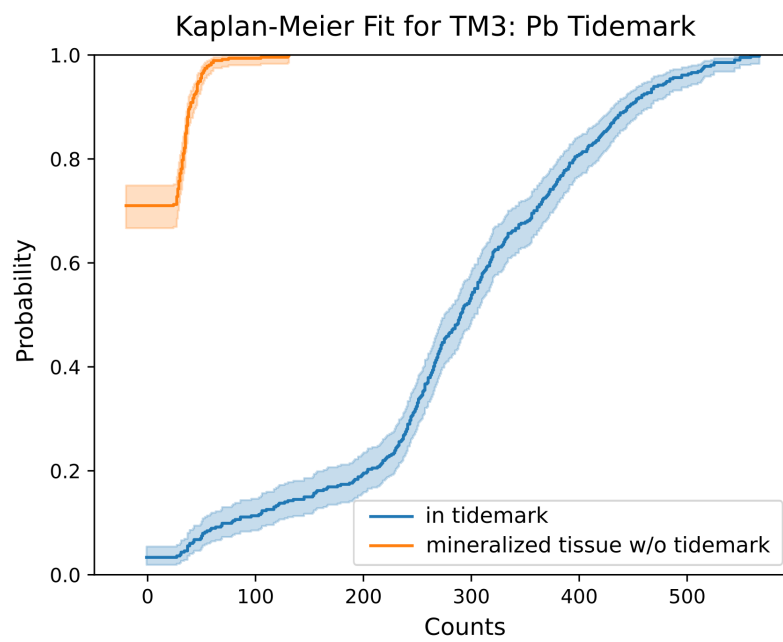
A Zn and Pb tidemark was found in every measured bone tissue section.

Fig. 8.5a shows the Kaplan-Meier estimated cumulative distribution function (as explained by Fig. 8.4b) for Zn in the tidemark (blue) and the remaining calcified tissue (orange) of the measured area of P3 – the same area as shown in Fig. 8.1. The medians between those two groups can easily be compared by just looking at the 0.5 probability level. The Zn median is about 3100 counts for the tidemark and 1020 counts for the mineralized tissue, respectively. As one can see from Fig. 8.5b that in about 70% of the mineralized tissue there was no Pb detected.

In two measured areas (TM1 of P1 and TM4 of P4) two tیدemarks were found. However, only one of them had an inner and an outer Pb tidemark. The other one, TM4, only has an inner Pb tidemark (see Fig. 8.6) with a median value of 92 counts in 20 s (8.7). The Zn medians were about 3840 and 2780 counts in the inner and outer tidemark, respectively (8.8).

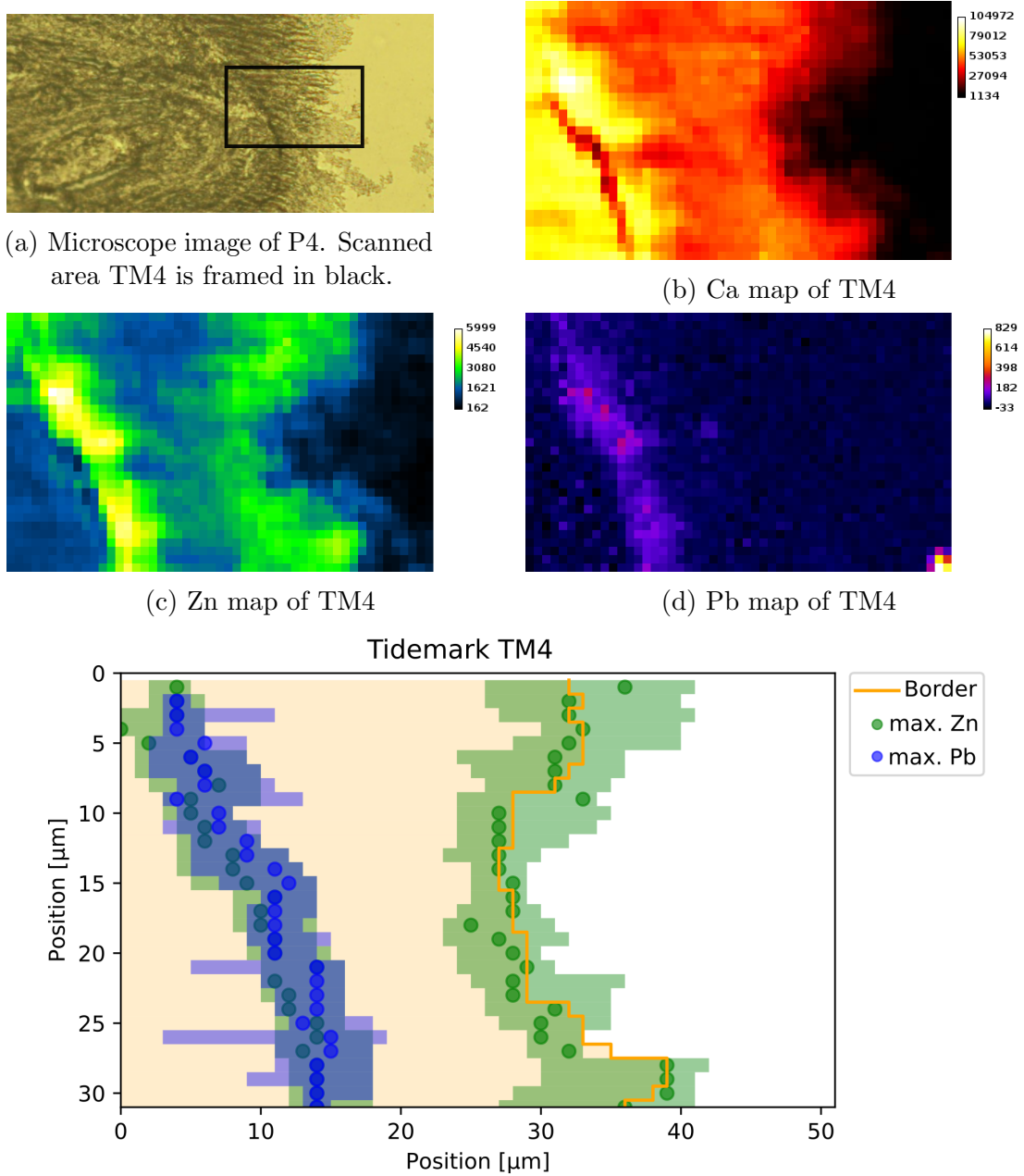


(a)



(b)

Figure 8.5: Kaplan-Meier estimate for Zn (a) and Pb (b) within the mineralized tissue (orange) and the tidemark (blue).



(e) Mineralized matrix (light yellow), the border between mineralized and non-mineralized matrix (yellow line), position of the peak maximum for Zn (green dots) and Pb (blue dots) as well as the FWHM for both Zn and Pb (in semi-transparent green and blue, respectively) of patient 4.

Figure 8.6: (a) Microscope image, (b-d) elemental maps and (e) found tidemarks of TM4

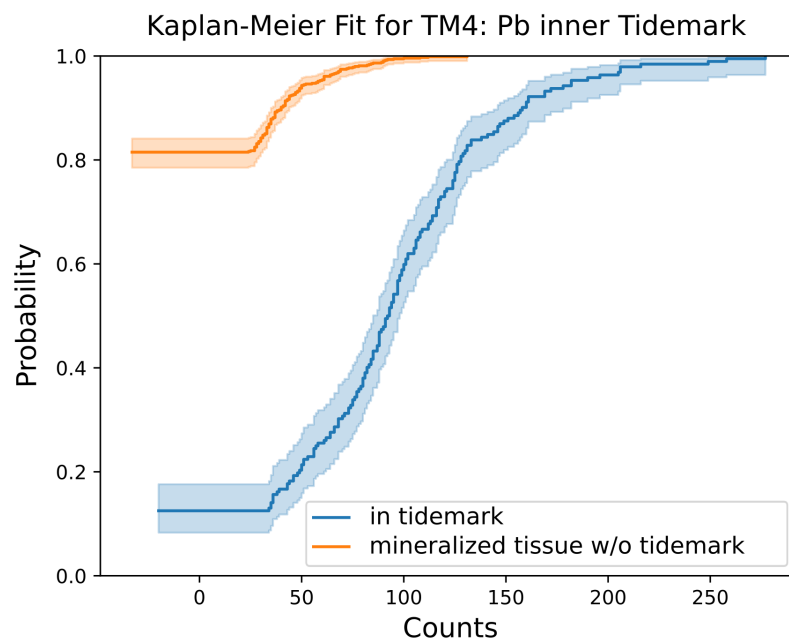
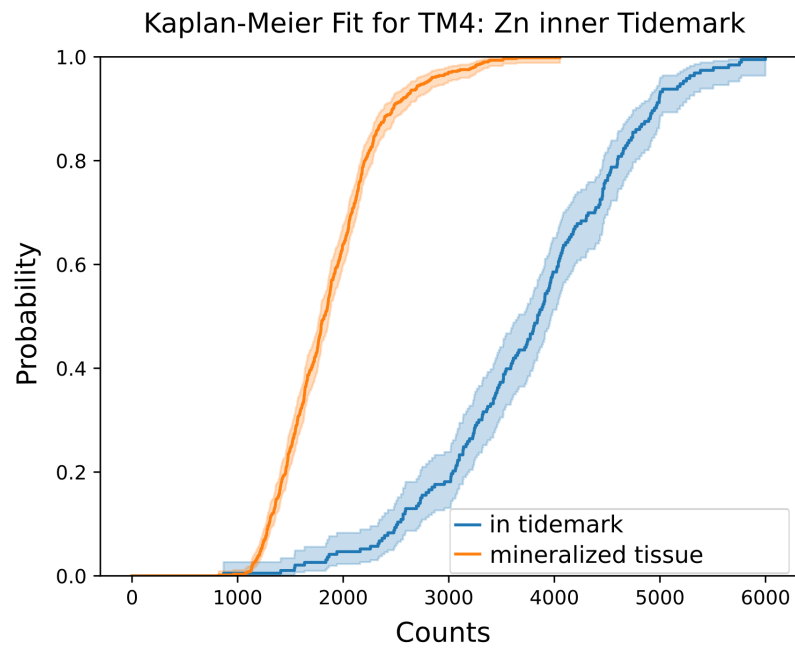
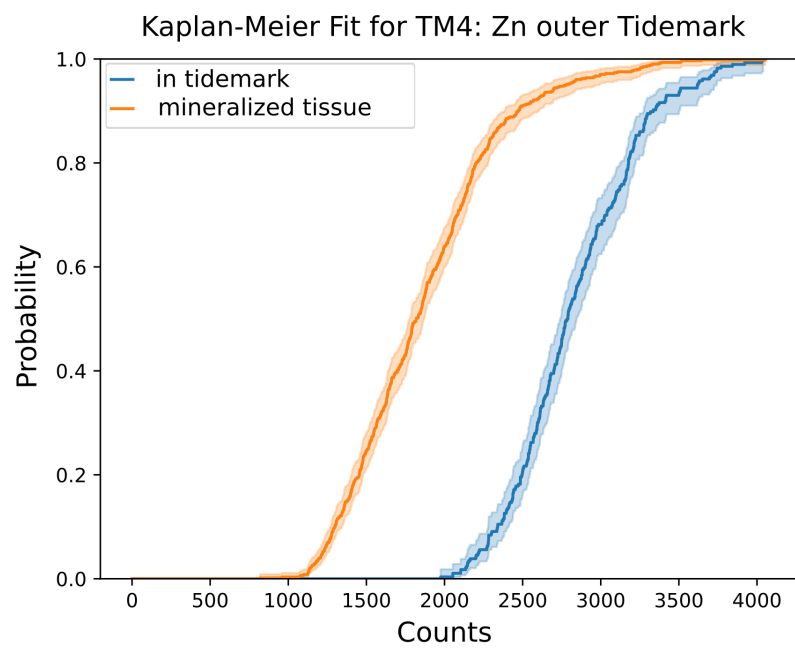


Figure 8.7: Kaplan-Meier estimate for Pb within the mineralized tissue (orange) and the tidemark (blue).



(a)



(b)

Figure 8.8: Kaplan-Meier estimate for Zn within the mineralized tissue (orange) and the tidemarks (blue).

The median width (FWHM) of the tidemarks ranged from 3 to 11 and 4 to 14.5 μm for Zn and Pb, respectively. The widths for all analyzed areas are listed in table 8.2. Interestingly, the highest differences were found between the two cuts of the same patient (P1). Median counts for the tidemarks can be found in table 8.3. For three samples we had so little counts above the detection limit in the mineralized tissue that the medians can not be compared. For those samples higher percentiles are given.

Table 8.2: Tidemark widths for Zn and Pb in all measured areas.

Patient	Section	number of tidemarks	Median width (FWHM in μm)	
			Zn	Pb
P1	TM1	2	3 (inner)	4 (inner)
			3 (outer)	4 (outer)
	TM6	1	11	14.5
P2	TM2	1	10	9
P3	TM3	1	5	6
P4	TM4	2	6 (inner)	6.5 (inner)
			9 (outer)	-
P5	TM5	1	8	9

Table 8.3: Zn and Pb median counts for the tidemark and the mineralized matrix in all measured areas. Values were determined by Kaplan-Meier fit.

Patient	Section	Zn median (counts in 20s)		Pb median (counts in 20s)	
		tidemark	matrix	tidemark	matrix
P1	TM1	2274 (inner)	1246	526 (inner)	60
		2182 (outer)		104 (outer)	
	TM6	2672	937	753	41
P2	TM2	3167	1605	282	76
P3	TM3	3098	1018	290 (377 for 75%)	- (29 for 75%)
P4	TM4	3841 (inner)	1819	-	-
		2784 (outer)		92 (182 for 95%)	- (57 for 95%)
P5	TM5	6913	4445	95 (119 for 75%)	- (42 for 75%)

8.4 Conclusion

Tidemark regions were identified and measured in areas of all six samples. Tidemark thicknesses (FWHM) varied between 3 and 11 μm for Zn and between 3.5 and 14.5 μm for Pb. In two of the measured areas (TM1 and TM4) the elemental map of Zn revealed a double tidemark. A double tidemark for Pb was only found in TM1. Matrix medians for Zn ranged from about 900 to 1800 counts in 20 s for all but one patient. For the same patients the tidemark Zn medians ranged from about 2200 to 3800 counts in 20 s. The patient with significantly higher median values (about 6900 counts in 20 s for the tidemark and 4400 for the matrix) was P5. For only two patients (P1 and P2) a median Pb matrix value could be detected. For all other patients, the Pb matrix did not have a detectable median value (e.g. see Figs. 8.5b and 8.7). Median Pb tidemark values ranged from 92 to 526 counts in 20 s.

9 Trace elements in bone tissue of patients with diagnosed osteomalacia

Osteomalacia is a bone condition causing inadequate bone mineralization. It is often caused by insufficient calcium, phosphate (hypophosphatemia) and vitamin D levels. However, there also exist genetic forms of this disease such as X-linked hypophosphatemia (XLH). In rare cases, hypophosphatemia can be caused by a tumor. This condition is called tumor-induced osteomalacia (TIO) and is reversible by resection of the tumor. [100, 101, 102]

To obtain a better understanding of the generalized condition, the trace element distribution within the mineralized tissue of seven patients suffering from different forms of osteomalacia was investigated. Additionally, a bone tissue sample of a patient possibly suffering from Zn poisoning (ZN 8 in table 9.1) and a osteonecrotic bone sample with microcallus formation (ZN9) were measured.

9.1 Materials and methods

9.1.1 Patients

Bone samples from nine patients with different diseases all leading to a change in bone structure were selected. Additionally, healthy bone tissue from seven individuals (3 male, 4 female) were chosen as controls.

Similar to the process described in section 7.1.2, all bone tissue samples were prepared as blocks. Therefore, they were dehydrated and fixed in a gradient of ethanol concentration (50 to 100%) and embedded in PMMA. The blocks were trimmed (Buehler Isomet, Lake Pluff, USA) and were ground with sand paper with

Table 9.1: List of measured samples form patients and controls.

Patient / Control	Areas measured	Sex	Disease
ZN1	1	f	malacia
ZN2	2	f	malacia Vit. D def.
ZN3	1	f	hypophosphatemia (XLH)
ZN4	1	m	hypophosphatemia (XLH)
ZN5	1	m	hypophosphatemia (XLH)
ZN6	2	m	hypophosphatemia (TIO)
ZN7	1	f	hypophosphatemia
ZN8	1	f	Zn intoxication?
ZN9	1	-	osteonecrosis & microcallus
MN12	1	m	control
MN13	1	m	control
MN14	1	m	control
MN40	1	f	control
MN41	1	f	control
MN42	1	f	control
MN43	1	f	control

decreasing grit size and finally polished by silk cloths loaded with diamond grains (PM5, Logitech Ltd., Glasgow, UK).

9.1.2 Micro XRF measurements

The samples were measured at the mySpot Beamline at the BESSY II with the confocal setup described in section 3.1.1. To find the areas of interest on the samples qBEI and microscope images were used. The chosen step size was $15 \times 15 \mu\text{m}^2$. The scans were performed with a measurement time of 10 s per voxel. A typical spectrum is shown in Fig. 9.1.

9.2 Data evaluation

The data evaluation process was much the same as for the tumor samples (see section 7.1.5).

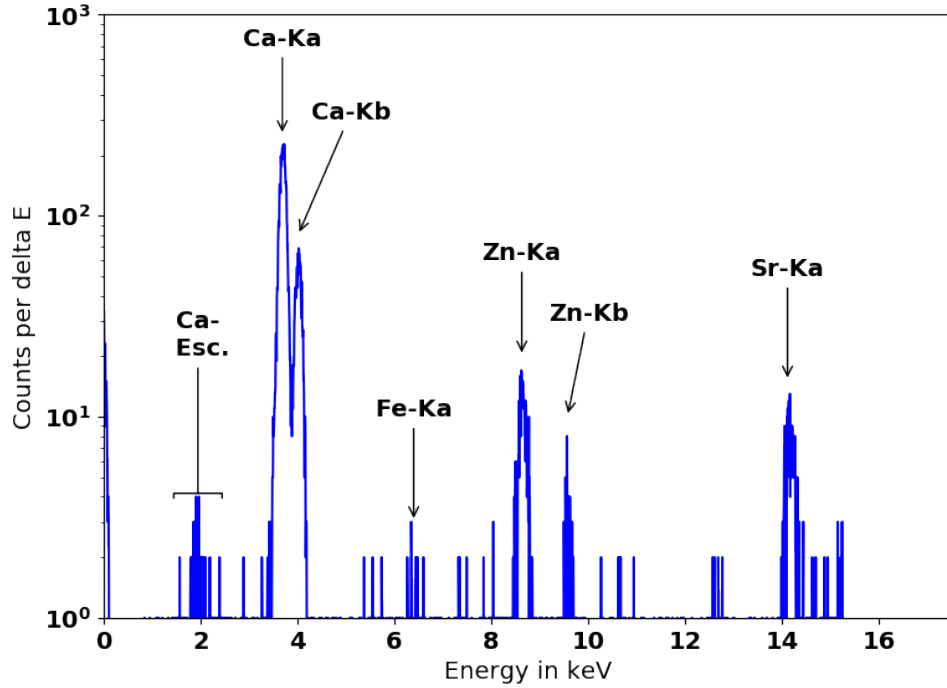


Figure 9.1: Typical spectrum obtained from a voxel in the mineralized bone matrix. Measurement time was 10s.

Notable differences are:

- As the BESSY II storage ring is operated in top-up mode, the correction to the ring current was no longer needed. However, for an easier comparison with the tumor data shown in section 7.2 the Ca maps were normalized to 1 s measurement time and 100 mA ring current.
- For the threshold value for the mineralized tissue ("*level*") 0.25 was chosen.

9.3 Results

For the malacia samples, one area of ZN1 and one of ZN2 each are shown in Fig. 9.2. While the Ca and Zn values for those two areas are very similar, the Sr values for patient ZN2 are a lot higher than for ZN1.

As example for the hypophosphatemia, Fig. 9.3 shows qBEI, Ca, Zn and Sr map of patient ZN5 while in Fig. 9.4 the maps for one male control (MN12) are given.

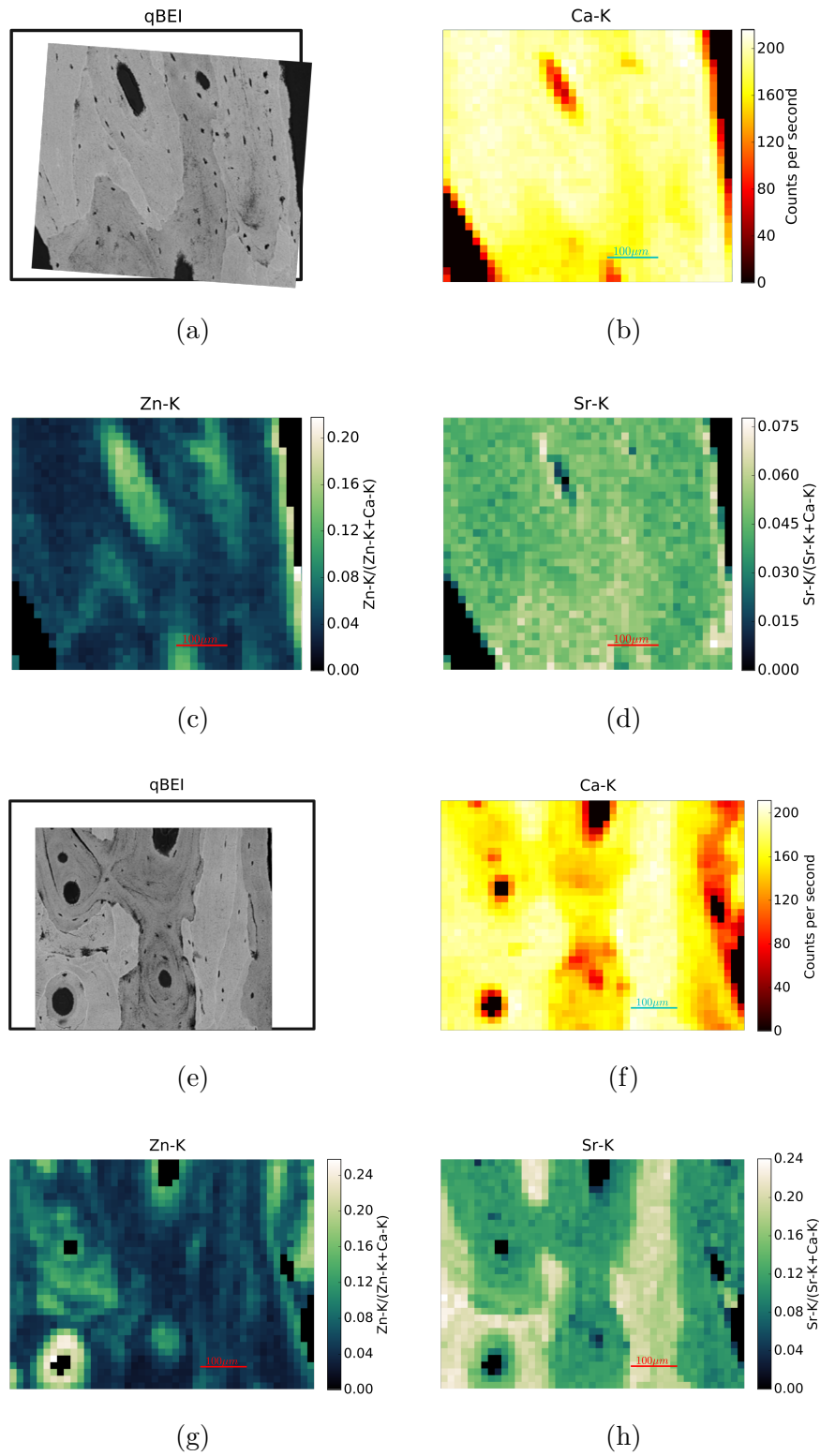


Figure 9.2: qBEI and elemental maps of the two malacia patients. (a)-(d) show the area of patient ZN1 and (e)-(h) one of the areas of patient ZN2.

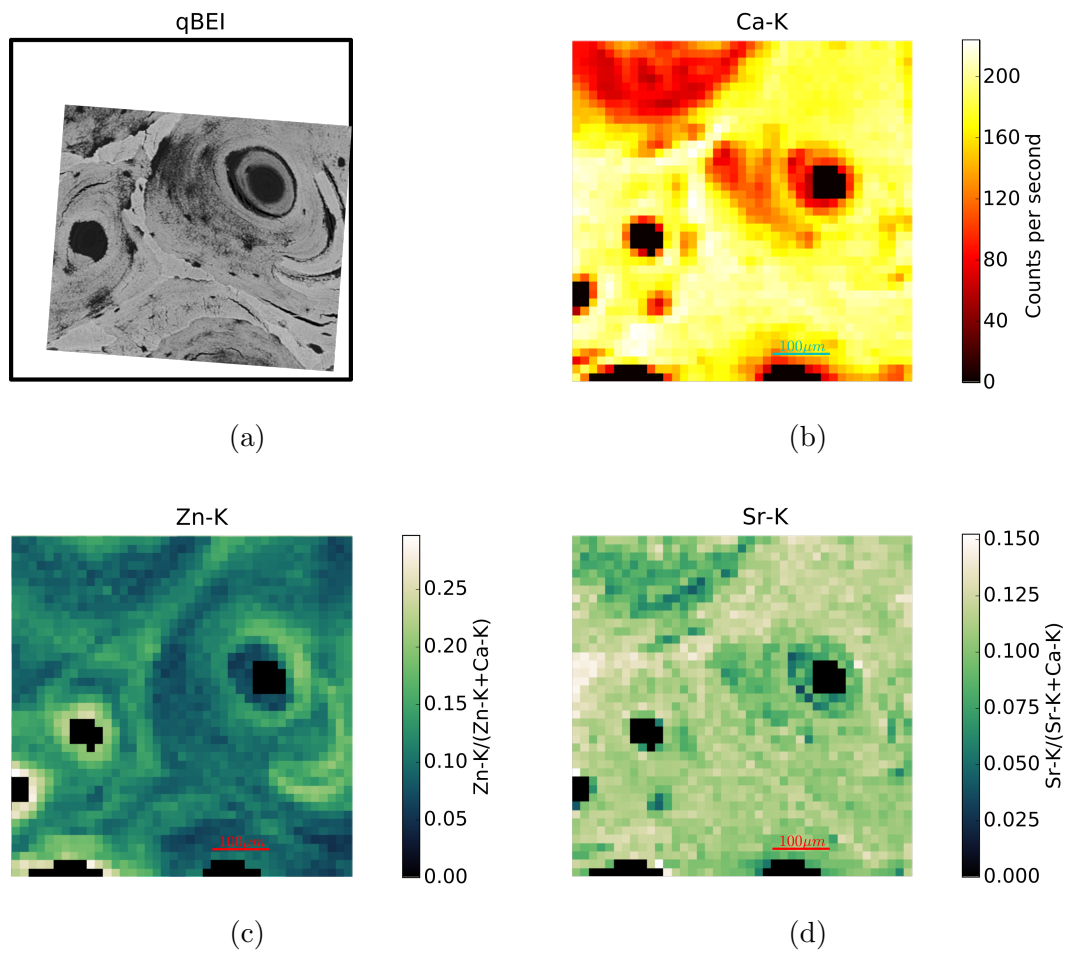


Figure 9.3: qBEI and elemental maps of one hypophosphatemia patient (ZN5).

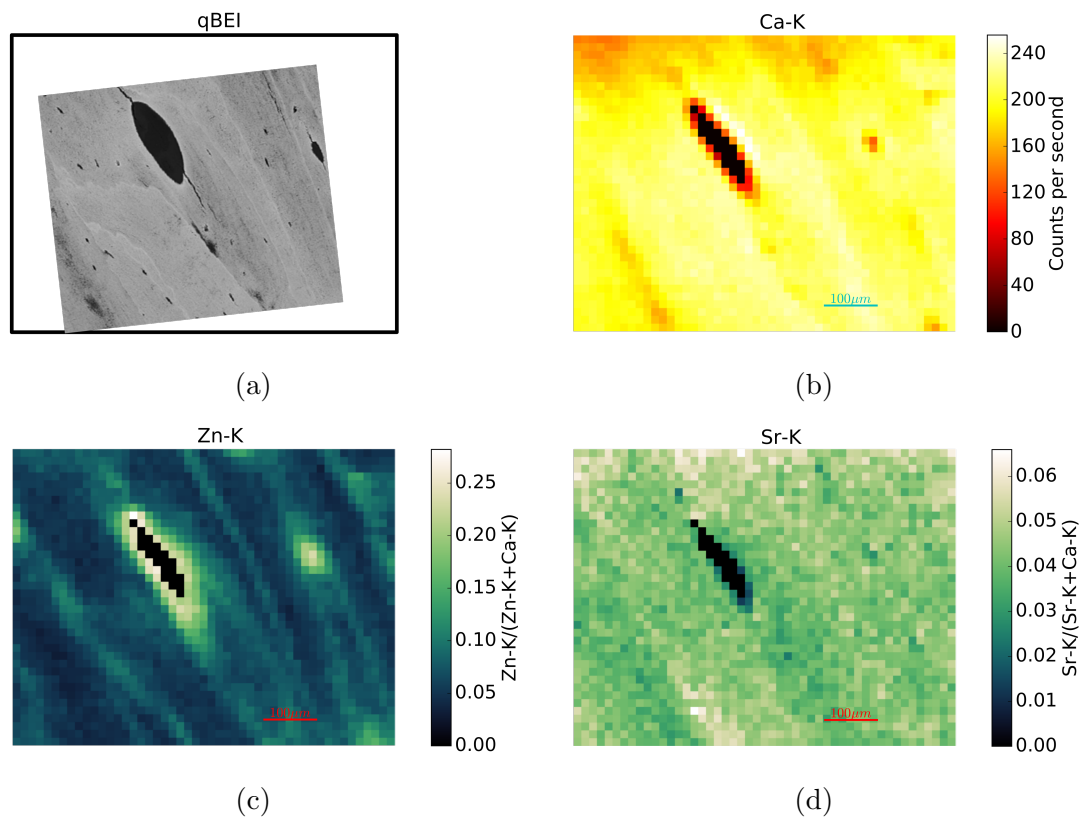


Figure 9.4: qBEI (a) as well as Ca (b), Zn (c) and Sr (d) map of a healthy control (MN12).

To compare the diseased samples with the healthy ones, the median of the Zn fractions are plotted versus the median of the Sr fraction for all measured samples (Fig. 9.5). As one can see, the healthy controls are somewhat clustered between the malacia samples in the low Zn region (on the left) and the hypophosphatemia sample as well as the suspected Zn intoxication and the osteonecrosis & microcallus sample in the high Zn region (on the right).



Figure 9.5: Median of the fraction of Zn versus median of the fraction of Sr for all measured samples. Male controls are shown in light green, female controls in dark green, malacia patients in orange, hypophosphatemia patients in blue, the Zn intoxication sample in pink and the osteonecrosis & microcallus sample in purple.

While the medians of the diseased samples seem to be clearly separated from the controls it is important to look at the complete distribution of Ca, Sr and Zn. Figs. 9.6, 9.8, and 9.10 show the stacked histogram for the healthy (on top) and the diseased samples (on bottom) for Ca, Sr and Zn, respectively.

In the boxplots (Figs. 9.7, 9.9 and 9.11), the median (black horizontal line) and a colored box starting at the 25th percentile and ending at the 75th percentile (containing 50% of the data) are given for all diseased samples as well as the female

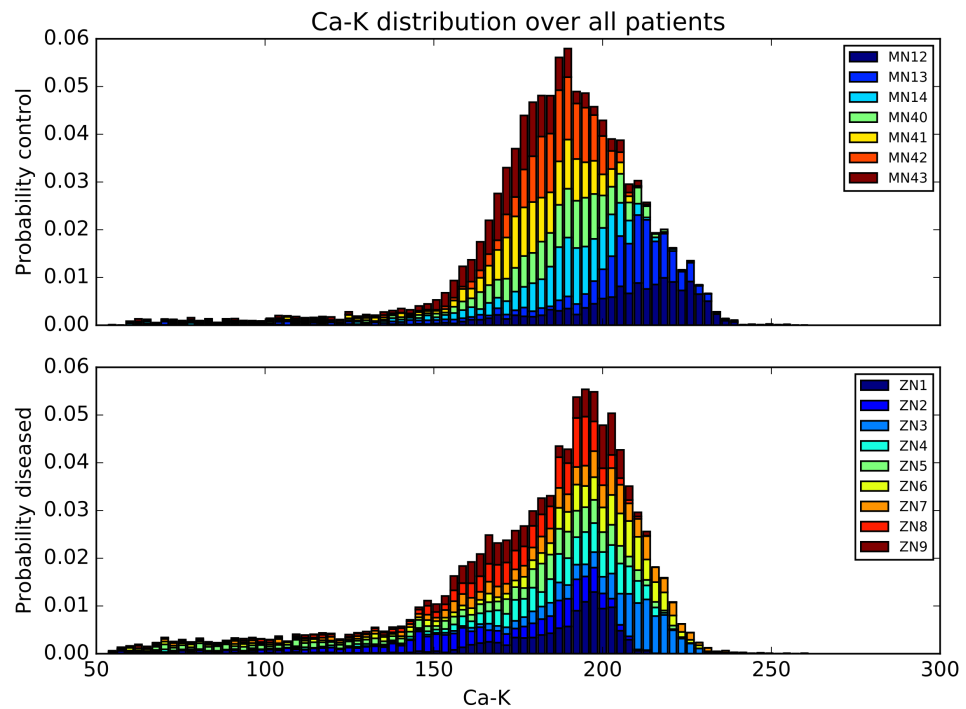


Figure 9.6: Ca distribution over all healthy (top) and diseased patients (bottom). The distributions were normalized so that each patient contributes equally to the histogram (independently of the numbers of points measured by patient).

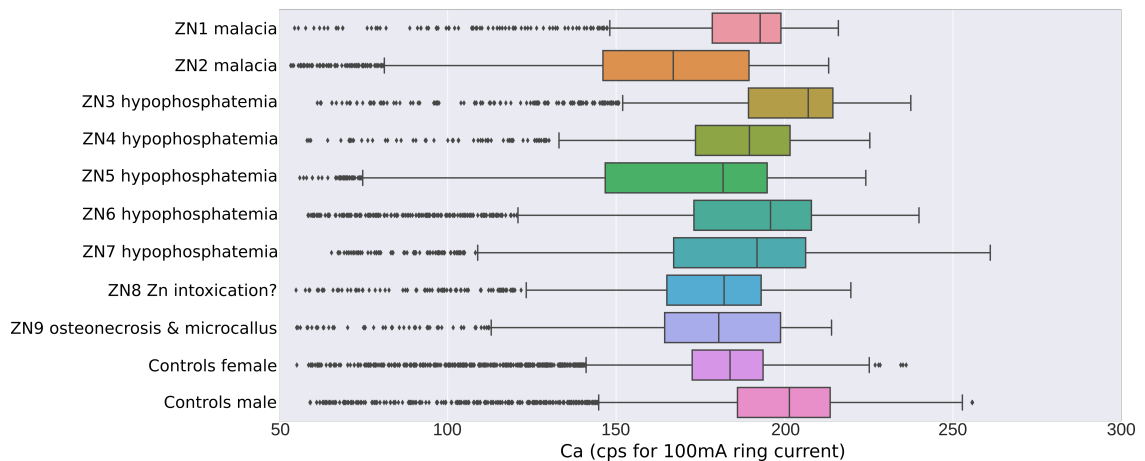


Figure 9.7: Boxplots for the Ca distribution of all diseased patients as well as of the female and male controls.

and male controls. The whisker length on each side of the colored box is at most $1.5\times$ the box size. The whisker length is shorter, if the last data point is closer to the colored box.

From the more detailed analysis of the elemental distribution, one can see that while the Ca distribution (Figs. 9.6 and 9.7) is very similar for the diseased patients and the controls, Ca values are slightly higher for two of the male controls (MN12 and MN13) as well as ZN3 and slightly lower for ZN2 (and to an even lesser degree for ZN5).

For the Sr fractions (Figs. 9.8 and 9.9), three patients (ZN2, ZN4 and ZN5) have considerably higher Sr content than the other patients and the controls. Furthermore, two samples show somewhat lower Sr levels (ZN6 and ZN7).

The Zn content was slightly higher in all but one hypophosphatemia sample (ZN4) and a little bit lower in the ZN1 sample (Figs. 9.10 and 9.11).

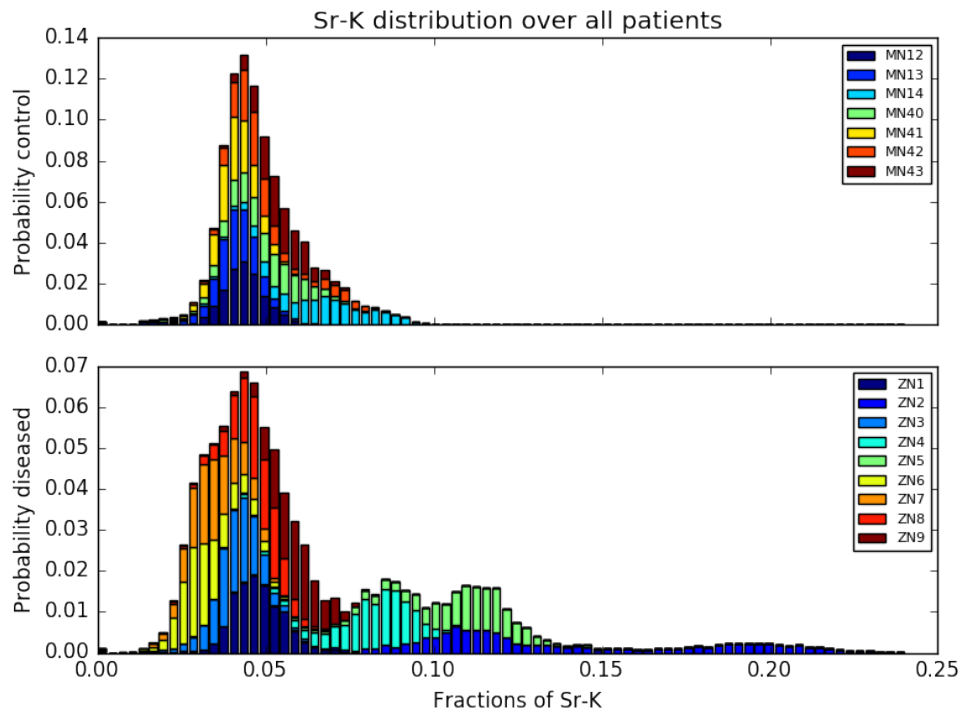


Figure 9.8: Sr distribution over all healthy (top) and diseased patients (bottom). The distributions were normalized so that each patient contributes equally to the histogram (independently of the numbers of points measured by patient).

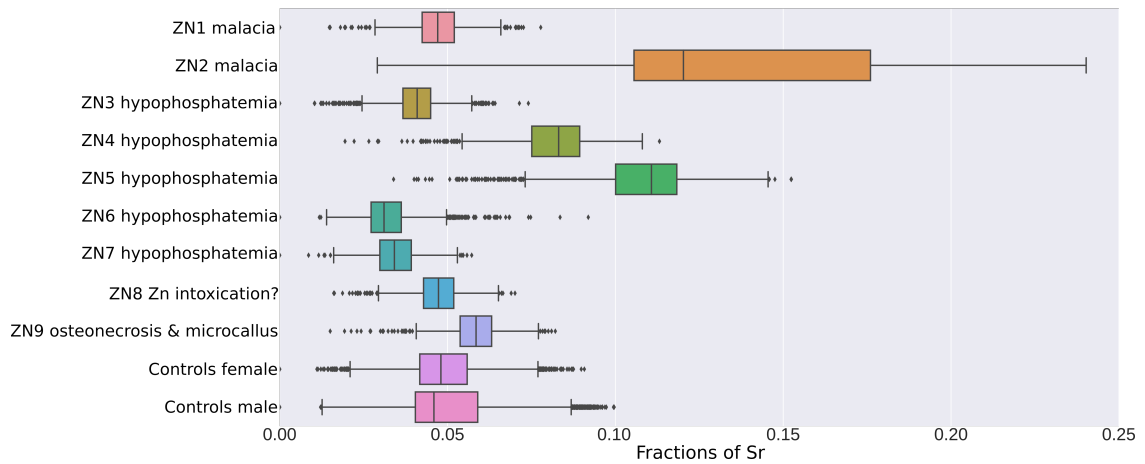


Figure 9.9: Boxplots for the Sr distribution of all diseased patients as well as of the female and male controls.

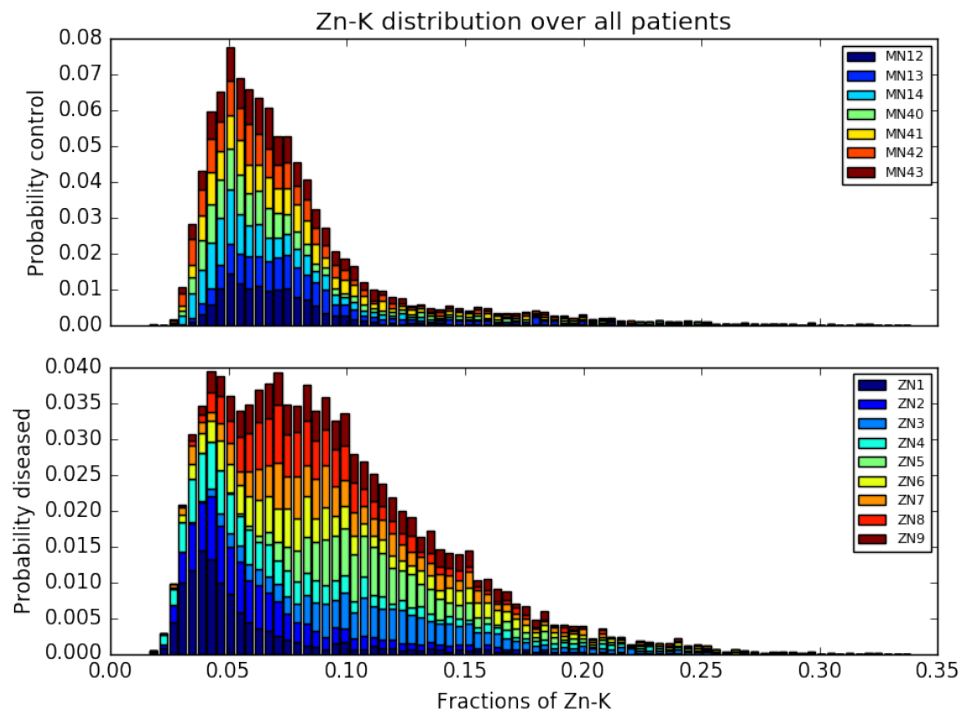


Figure 9.10: Zn distribution over all healthy (top) and diseased patients (bottom). The distributions were normalized so that each patient contributes equally to the histogram (independently of the numbers of points measured by patient).

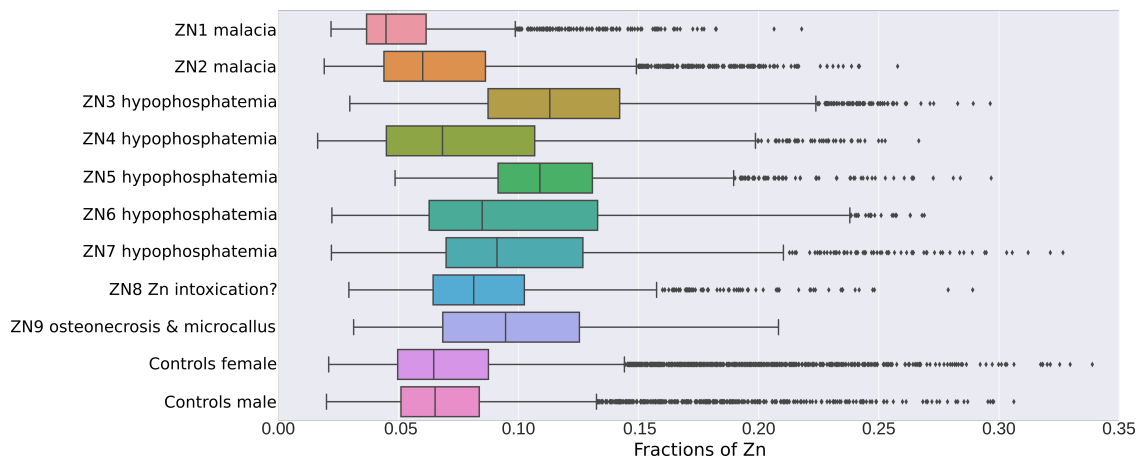


Figure 9.11: Boxplots for the Zn distribution of all diseased patients as well as of the female and male controls.

9.4 Discussion and Outlook

While there are differences in the Zn and Sr counts for the diseased compared to the healthy samples, no clear trend emerged from the analysis so far.

For a more detailed data evaluation, it would be very interesting to compare regions with the same Ca content (same gray level in the qBEI image) of healthy and diseased patients.

Additionally, it would be useful to see where the high concentrations of Zn are located with respect to the structures in the qBEI images.

10 Concluding remarks and Outlook

In the scope of this thesis, different SR-XRF methods were compared to find the ideal setup to investigate trace element distributions in bone.

For measurements with resolution in the tens of micrometer range, a confocal μ XRF setup at the ANKA FLUO beamline and a full-field setup at the BESSY II BAMline were compared. Although, the full-field setup had a better resolution in the plane, it was not sensitive enough for Zn (a trace element in bone). The confocal SR- μ XRF setup was able to image both Ca and Zn sufficiently. Therefore, it was concluded that a confocal SR- μ XRF setup is superior to a full-field setup for the analysis of trace elements in bone (see chapter 5).

For a resolution in the micrometer and sub-micrometer range, the XRF setup at Diamond's B16 bending magnet test beamline was characterized with a standard and different samples prepared as thin slices. The setup proved to be ideal for imaging trace elements in biological samples (see chapter 6).

After defining the optimal setup for the measurement of trace elements in bone, three different sample sets were analyzed.

For patients with a primary malignant bone tumor (osteosarcoma) a higher Zn concentration was found in the tumorous mineralized tissue compared to the normal adjacent bone. While Fe and Sr were also found in these samples, no differences between healthy and diseased tissue were found for them (chapter 7).

To further investigate the tidemark, a narrow structure between the non-calcified and the calcified articular cartilage, thin bone samples were measured. The tidemark region was found in all analyzed samples. In two specimens a double tidemark was found. Both, Zn and Pb counts were higher in the tidemark than in the remaining mineralized matrix. Tidemark thickness ranged from about 3 to 11 μm for Zn and 3.5 to 14.5 μm for Pb (chapter 8).

Sr and Zn were analyzed in samples with inadequate bone mineralization, a condition

called osteomalacia. Additionally, bone tissue from healthy patients was measured as controls. While differences in both Zn and Sr counts for diseased samples compared to the healthy controls were identified, no clear trend emerged (chapter 9).

10.1 Outlook

To further evaluate the osteomalacia samples, it would be interesting to compare regions with the same Ca content (the same gray level in the qBEI images) of healthy and diseased patients. Additionally, it would be beneficial to know where the high Zn concentrations are situated with respect to the structures visible in the qBEI images.

It would be interesting to assess the speciation of Zn in osteosarcoma samples by XANES measurements. This would determine if only the concentration of Zn changes between a tumorous area and its surrounding area or if the chemical binding is also changed.

A speciation of Zn in the tidemark would also be of interest. The assessment of chemical species of lead accumulated in the tidemark was already done by F. Meirer et al. [103] and showed no differences in the μ -XANES spectra between tidemark and trabecular bone region.

Furthermore, there exist a lot of SR- μ XRF data from both this thesis and the PhD thesis of Bernhard Pemmer, where Sr was measured (amongst other elements) at the FLUO beamline at ANKA. As there is not a lot known about the Sr distribution in human bone, a detailed analysis of this huge data set could provide a new understanding of the role of Sr in human bone tissue.

For now, defining different regions of interest in elemental maps such as the healthy and tumorous areas in the osteosarcoma samples had often had to be done by hand in imaging processing software (e.g. ImageJ). But with higher computer power as well as the availability of algorithms for unsupervised machine learning to find clusters such as the HDBSCAN [104], it should be possible to automate this process. Additionally, clustering could provide further insight by showing differences between sample groups which were not previously thought of by the experimenters.

Bibliography

- [1] A. Al-Ebraheem, K. Geraki, R. Leek, A. L. Harris, and M. J. Farquharson, “The use of bio-metal concentrations correlated with clinical prognostic factors to assess human breast tissues”, *X-Ray Spectrom.*, vol. 42, p. 330–336, 2013.
- [2] P. Christudoss, R. Selvakumar, J. J. Fleming, and G. Gopalakrishnan, “Zinc status of patients with benign prostatic hyperplasia and prostate carcinoma.”, *Indian J. Urol.*, vol. 27, p. 14–8, 2011.
- [3] A. Peretz, T. Papadopoulos, D. Willems, A. Hotimsky, N. Michiels, V. Siderova, P. Bergmann, and J. Neve, “Zinc supplementation increases bone alkaline phosphatase in healthy men”, *Journal of Trace Elements in Medicine and Biology*, vol. 15, no. 2, p. 175–178, 2001.
- [4] A. Ito, H. Kawamura, M. Otsuka, M. Ikeuchi, H. Ohgushi, K. Ishikawa, K. Onuma, N. Kanzaki, Y. Sogo, and N. Ichinose, “Zinc-releasing calcium phosphate for stimulating bone formation”, *Mater. Sci. Eng. C*, vol. 22, p. 21–25, 2002.
- [5] M. Yamaguchi and R. Yamaguchi, “Action of zinc on bone metabolism in rats”, *Biochem. Pharmacol.*, vol. 35, p. 773–777, 1986.
- [6] B. Starcher and F. H. Kratzer, “Effect of zinc on bone alkaline phosphatase in turkey poults.”, *Journal of Nutrition*, vol. 79, p. 18–22, 1963.
- [7] J. Ovesen, B. Møller-Madsen, J. Thomsen, G. Danscher, and L. Mosekilde, “The positive effects of zinc on skeletal strength in growing rats”, *Bone*, vol. 29, no. 6, p. 565–570, 2001.
- [8] P. Relea, M. Revilla, E. Ripoll, I. Arribas, L. F. Villa, and H. Rico, “Zinc, biochemical markers of nutrition, and type I osteoporosis”, *Age and Ageing*, vol. 24, no. 4, p. 303–307, 1995.

- [9] V. B. Kraus, “Osteoarthritis: The zinc link”, *Nature*, vol. 507, no. 7493, p. 441, 2014.
- [10] P. S. Barry, “A comparison of concentrations of lead in human tissues.”, *Occupational and Environmental Medicine*, vol. 32, no. 2, p. 119–139, 1975.
- [11] G. Olchowiak, J. Widomska, M. Tomaszewski, M. Gospodarek, M. Tomaszewska, and E. Jagiello-Wojtowicz, “The influence of lead on the biomechanical properties of bone tissue in rats”, *Annals of Agricultural and Environmental Medicine*, vol. 21, no. 2, 2014.
- [12] A. E. Nelson, X. A. Shi, T. A. Schwartz, J.-C. Chen, J. B. Renner, K. L. Caldwell, C. G. Helmick, and J. M. Jordan, “Whole blood lead levels are associated with radiographic and symptomatic knee osteoarthritis: a cross-sectional analysis in the johnston county osteoarthritis project”, *Arthritis Research & Therapy*, vol. 13, p. R37, 2011.
- [13] J. A. Brito, I. M. Costa, A. M. e Silva, J. M. Marques, C. M. Zagalo, I. I. Cavaleiro, T. A. Fernandes, and L. L. Gonçalves, “Changes in bone pb accumulation: Cause and effect of altered bone turnover”, *Bone*, vol. 64, p. 228–234, 2014.
- [14] Y. Sun, D. Sun, Z. Zhou, G. Zhu, H. Zhang, X. Chang, L. Lei, and T. Jin, “Osteoporosis in a chinese population due to occupational exposure to lead”, *American Journal of Industrial Medicine*, vol. 51, no. 6, p. 436–442, 2008.
- [15] G. A. B. Silva, B. M. Bertassoli, C. A. Sousa, J. D. Albergaria, R. S. de Paula, and E. C. Jorge, “Effects of strontium ranelate treatment on osteoblasts cultivated onto scaffolds of trabeculae bovine bone”, *Journal of Bone and Mineral Metabolism*, vol. 36, p. 73–86, 2018.
- [16] U. Pietsch, V. Holy, and T. Baumbach, *High-resolution X-ray scattering: from thin films to lateral nanostructures*. Springer-Verlag New York, second ed., 2004.
- [17] R. Bartolini (John Adams Institute) [Public domain], “Synchrotron radiation energy flux”, *via Wikimedia Commons*, 2010.

- [18] G. Buzanich, “Characterization of compound refractive lenses for synchrotron μ -XRF and μ -XAS and applications with high spatial resolution”, *PhD Thesis, Atominstitut, TU Wien*, 2012.
- [19] J. Jackson, “Classical electrodynamics”, *via Wikimedia Commons*, 1999.
- [20] B. Holst [GFDL (<http://www.gnu.org/copyleft/fdl.html>)], “Undulator (english).svg”, *via Wikimedia Commons*, 2005.
- [21] DESY Webpage, “Comparison of the spectra of bending magnets, wigglers and undulators”, *How does a synchrotron radiation source work?*, accessed 26.9.2018.
- [22] Oxford Instruments plc, “Construction and operation of an SDD detector.”, *Silicon Drift Detectors Explained*, 2012.
- [23] I. Ordavo, S. Ihle, V. Arkadiev, O. Scharf, H. Soltau, A. Bjeoumikhov, S. Bjeoumikhova, G. Buzanich, R. Gubzhokov, A. Günther, R. Hartmann, P. Holl, N. Kimmel, M. Kühbacher, M. Lang, N. Langhoff, A. Liebel, M. Radtke, U. Reinholz, H. Riesemeier, G. Schaller, F. Schopper, L. Strüder, C. Thamm, and R. Wedell, “A new pnCCD-based color X-ray camera for fast spatial and energy-resolved measurements”, *Nucl. Instruments Methods Phys. Res. Sect. A Accel. Spectrometers, Detect. Assoc. Equip.*, vol. 654, p. 250–257, 2011.
- [24] H. Mimura, S. Matsuyama, H. Yumoto, H. Hara, K. Yamamura, Y. Sano, M. Shibahara, K. Endo, Y. Mori, Y. Nishino, K. Tamasaku, M. Yabashi, T. Ishikawa, and K. Yamauchi, “Hard x-ray diffraction-limited nanofocusing with kirkpatrick-baez mirrors”, *Japanese Journal of Applied Physics*, vol. 44, no. 4L, p. L539, 2005.
- [25] I. Snigireva and A. Snigirev, “X-ray microanalytical techniques based on synchrotron radiation”, *J. Environ. Monit.*, vol. 8, p. 33–42, 2006.
- [26] International Atomic Energy Agency, *Quantitative X Ray Analysis System*. No. 21 in Computer Manual Series, Vienna: IAEA, 2009.

- [27] P. Van Espen, K. Janssens, and J. Nobels, “AXIL-PC, software for the analysis of complex X-ray spectra”, *Chemom. Intell. Lab. Syst.*, vol. 1, p. 109–114, 1986.
- [28] B. Vekemans, K. Janssens, L. Vincze, F. Adams, and P. Van Espen, “Analysis of X-ray spectra by iterative least squares (AXIL): New developments”, *X-Ray Spectrom.*, vol. 23, p. 278–285, 1994.
- [29] NIST Webpage, “X-ray mass attenuation coefficient for cortical bone”, <https://physics.nist.gov/PhysRefData/XrayMassCoef/ComTab/bone.html>, 2018.
- [30] K. Janssens, W. De Nolf, G. Van Der Snickt, L. Vincze, B. Vekemans, R. Terzano, and F. E. Brenker, “Recent trends in quantitative aspects of microscopic X-ray fluorescence analysis”, *TrAC Trends Anal. Chem.*, vol. 29, p. 464–478, 2010.
- [31] M. Holt, R. Harder, R. Winarski, and V. Rose, “Nanoscale Hard X-Ray Microscopy Methods for Materials Studies”, *Annual Review of Materials Science*, vol. 43, p. 183–211, 2013.
- [32] M. West, A. T. Ellis, C. Streli, C. Vanhoof, and P. Wobrauschek, “2017 atomic spectrometry update - a review of advances in x-ray fluorescence spectrometry and its special applications”, *J. Anal. At. Spectrom.*, vol. 32, p. 1629–1649, 2017.
- [33] A. Roschger, J. G. Hofstaetter, B. Pemmer, N. Zoeger, P. Wobrauschek, G. Falkenberg, R. Simon, A. Berzlanovich, H. W. Thaler, P. Roschger, K. Klaushofer, and C. Streli, “Differential accumulation of lead and zinc in double-tidemarks of articular cartilage.”, *Osteoarthritis Cartilage*, vol. 21, p. 1707–15, 2013.
- [34] B. Pemmer, J. G. Hofstaetter, F. Meirer, S. Smolek, P. Wobrauschek, R. Simon, R. K. Fuchs, M. R. Allen, K. W. Condon, S. Reinwald, R. J. Phipps, D. B. Burr, E. P. Paschalis, K. Klaushofer, C. Streli, and P. Roschger, “Increased strontium uptake in trabecular bone of ovariectomized calcium-deficient rats

- treated with strontium ranelate or strontium chloride.”, *J. Synchrotron Radiat.*, vol. 18, p. 835–41, 2011.
- [35] B. Pemmer, A. Roschger, A. Wastl, J. G. Hofstaetter, P. Wobrauschek, R. Simon, H. W. Thaler, P. Roschger, K. Klaushofer, and C. Streli, “Spatial distribution of the trace elements zinc, strontium and lead in human bone tissue.”, *Bone*, vol. 57, p. 184–93, 2013.
- [36] R. Simon, G. Buth, and M. Hagelstein, “The X-ray-fluorescence facility at ANKA, Karlsruhe: Minimum detection limits and micro probe capabilities”, *Nucl. Instruments Methods Phys. Res. Sect. B Beam Interact. with Mater. Atoms*, vol. 199, p. 554–558, 2003.
- [37] O. Scharf, S. Ihle, I. Ordavo, V. Arkadiev, A. Bjeoumikhov, S. Bjeoumikhova, G. Buzanich, R. Gubzhokov, A. Günther, R. Hartmann, M. Kühbacher, M. Lang, N. Langhoff, A. Liebel, M. Radtke, U. Reinholz, H. Riesemeier, H. Soltau, L. Strüder, A. F. Thünemann, and R. Wedell, “Compact pnCCD-based X-ray camera with high spatial and energy resolution: a color X-ray camera.”, *Anal. Chem.*, vol. 83, p. 2532–8, 2011.
- [38] G. Martínez-Criado, J. Villanova, R. Tucoulou, D. Salomon, J.-P. Suuronen, S. Labouré, C. Guilloud, V. Valls, R. Barrett, E. Gagliardini, Y. Dabin, R. Baker, S. Bohic, C. Cohen, and J. Morse, “ID16B: a hard X-ray nanoprobe beamline at the ESRF for nano-analysis”, *Journal of Synchrotron Radiation*, vol. 23, p. 344–352, 2016.
- [39] L. Lemelle, A. Simionovici, T. Schoonjans, R. Tucoulou, E. Enrico, M. Salomé, A. Hofmann, and B. Cavalazzi, “Analytical requirements for quantitative x-ray fluorescence nano-imaging of metal traces in solid samples”, *TrAC Trends in Analytical Chemistry*, vol. 91, no. Supplement C, p. 104–111, 2017.
- [40] K. J. S. Sawhney, I. P. Dolbnya, M. K. Tiwari, L. Alianelli, S. M. Scott, G. M. Preece, U. K. Pedersen, and R. D. Walton, “A Test Beamline on Diamond Light Source”, in *American Institute of Physics Conference Series* (R. Garrett, I. Gentle, K. Nugent, and S. Wilkins, eds.), vol. 1234 of *American Institute of Physics Conference Series*, p. 387–390, 2010.

- [41] K. J. S. Sawhney, I. P. Dolbnya, S. M. Scott, M. K. Tiwari, G. M. Preece, S. G. Alcock, and A. W. Malandain, “A double multilayer monochromator for the B16 Test beamline at the Diamond Light Source”, in *Society of Photo-Optical Instrumentation Engineers (SPIE) Conference Series*, vol. 8139 of *Proceedings of the SPIE*, p. 813908, 2011.
- [42] Diamond Webpage *B16 - Facility and Equipment Availability*, 2017.
- [43] Diamond Webpage *B16 - Beamline Schematic*, 2017.
- [44] P. Roschger, P. Fratzl, J. Eschberger, and K. Klaushofer, “Validation of quantitative backscattered electron imaging for the measurement of mineral density distribution in human bone biopsies”, *Bone*, vol. 23, p. 319–326, 1998.
- [45] P. Roschger, E. P. Paschalis, P. Fratzl, and K. Klaushofer, “Bone mineralization density distribution in health and disease.”, *Bone*, vol. 42, p. 456–66, 2008.
- [46] N. Fratzl-Zelman, P. Roschger, A. Gourrier, M. Weber, B. M. Misof, N. Loveridge, J. Reeve, K. Klaushofer, and P. Fratzl, “Combination of nanoindentation and quantitative backscattered electron imaging revealed altered bone material properties associated with femoral neck fragility.”, *Calcif. Tissue Int.*, vol. 85, p. 335–43, 2009.
- [47] A. Roschger, S. Gamsjaeger, B. Hofstetter, A. Masic, S. Blouin, P. Messmer, A. Berzlanovich, E. P. Paschalis, P. Roschger, K. Klaushofer, and P. Fratzl, “Relationship between the $\nu_2\text{PO}_4$ /amide III ratio assessed by Raman spectroscopy and the calcium content measured by quantitative backscattered electron microscopy in healthy human osteonal bone.”, *J. Biomed. Opt.*, vol. 19, p. 065002, 2014.
- [48] M. Rauwolf, A. Turyanskaya, A. Roschger, J. Prost, R. Simon, O. Scharf, M. Radtke, T. Schoonjans, A. Guilherme Buzanich, K. Klaushofer, P. Wobrauschek, J. G. Hofstaetter, P. Roschger, and C. Streli, “Synchrotron radiation micro X-ray fluorescence spectroscopy of thin structures in bone samples: comparison of confocal and color X-ray camera setups”, *Journal of Synchrotron Radiation*, vol. 24, p. 307–311, 2017.

- [49] B. Pemmer, A. Roschger, A. Wastl, J. G. Hofstaetter, P. Wobrauschek, R. Simon, H. W. Thaler, P. Roschger, K. Klaushofer, and C. Streli, “Spatial distribution of the trace elements zinc, strontium and lead in human bone tissue.”, *Bone*, vol. 57, p. 184–93, 2013.
- [50] S. Smolek, B. Pemmer, M. Fölser, C. Streli, and P. Wobrauschek, “Confocal micro-x-ray fluorescence spectrometer for light element analysis.”, *Rev. Sci. Instrum.*, vol. 83, p. 083703, 2012.
- [51] B. Pemmer, J. G. Hofstaetter, F. Meirer, S. Smolek, P. Wobrauschek, R. Simon, R. K. Fuchs, M. R. Allen, K. W. Condon, S. Reinwald, R. J. Phipps, D. B. Burr, E. P. Paschalis, K. Klaushofer, C. Streli, and P. Roschger, “Increased strontium uptake in trabecular bone of ovariectomized calcium-deficient rats treated with strontium ranelate or strontium chloride.”, *J. Synchrotron Radiat.*, vol. 18, p. 835–41, 2011.
- [52] P. Roschger, I. Manjubala, N. Zoeger, F. Meirer, R. Simon, C. Li, N. Fratzl-Zelman, B. M. Misof, E. P. Paschalis, C. Streli, P. Fratzl, and K. Klaushofer, “Bone material quality in transiliac bone biopsies of postmenopausal osteoporotic women after 3 years of strontium ranelate treatment.”, *J. Bone Miner. Res.*, vol. 25, p. 891–900, 2010.
- [53] N. Zoeger, C. Streli, P. Wobrauschek, C. Jokubonis, G. Pepponi, P. Roschger, J. Hofstaetter, A. Berzlanovich, D. Wegrzynek, E. Chinea-Cano, A. Markowicz, R. Simon, and G. Falkenberg, “Determination of the elemental distribution in human joint bones by SR micro XRF”, *X-Ray Spectrom.*, vol. 37, p. 3–11, 2008.
- [54] H.-J. Seo, Y.-E. Cho, T. Kim, H.-I. Shin, and I.-S. Kwun, “Zinc may increase bone formation through stimulating cell proliferation, alkaline phosphatase activity and collagen synthesis in osteoblastic MC3T3-E1 cells.”, *Nutr. Res. Pract.*, vol. 4, p. 356–61, 2010.
- [55] J. Beattie and A. Avenell, “Trace element nutrition and bone metabolism”, *Nutr. Res. Rev.*, 1992.

- [56] S. L. Hall, H. P. Dimai, and J. R. Farley, “Effects of zinc on human skeletal alkaline phosphatase activity in vitro.”, *Calcif. Tissue Int.*, vol. 64, p. 163–72, 1999.
- [57] M. Rauwolf, A. Turyanskaya, D. Ingerle, N. Szoboszlai, I. Pape, A. W. Mandain, O. J. L. Fox, L. Hahn, K. J. S. Sawhney, and C. Streli, “Characterization of a submicro-X-ray fluorescence setup on the B16 beamline at Diamond Light Source”, *Journal of Synchrotron Radiation*, vol. 25, p. 1189–1195, 2018.
- [58] M. Ugarte, K. Geraki, and G. Jeffery, “Iron accumulates in the primate choroid of the eye with aging as revealed with synchrotron x-ray fluorescence microscopy”, *Metallomics*, vol. 8, p. 1071–1080, 2016.
- [59] V. G. Mihucz, F. Meirer, Z. Polgári, A. Réti, G. Pepponi, D. Ingerle, N. Szoboszlai, and C. Streli, “Iron overload of human colon adenocarcinoma cells studied by synchrotron-based x-ray techniques”, *JBIC Journal of Biological Inorganic Chemistry*, vol. 21, p. 241–249, 2016.
- [60] National Institute of Standards & Technology, “Certificate of analysis”, *Standard Reference Material® 2783 - Air Particulate on Filter Media*, 2011.
- [61] B. Laforce, S. Schmitz, B. Vekemans, J. Rudloff, J. Garrevoet, R. Tucoulou, F. E. Brenker, G. Martinez-Criado, and L. Vincze, “Nanosopic x-ray fluorescence imaging of meteoritic particles and diamond inclusions”, *Analytical Chemistry*, vol. 86, no. 24, p. 12369–12374, 2014. PMID: 25395119.
- [62] A. Gaál, G. Orgován, V. G. Mihucz, I. Pape, D. Ingerle, C. Streli, and N. Szoboszlai, “Metal transport capabilities of anticancer copper chelators”, *Journal of Trace Elements in Medicine and Biology*, vol. 47, p. 79–88, 2018.
- [63] A. Gaál, V. G. Mihucz, S. Bősze, I. Szabó, M. Baranyi, P. Horváth, C. Streli, and N. Szoboszlai, “Comparative in vitro investigation of anticancer copper chelating agents”, *Microchemical Journal*, vol. 136, no. Supplement C, p. 227 – 235, 2018. Pharmacological Research and Analytical Approaches.
- [64] M. Rauwolf, B. Pemmer, A. Roschger, A. Turyanskaya, S. Smolek, A. Maderitsch, P. Hischenhuber, M. Foelser, R. Simon, S. Lang, S. E. Puchner, R. Windhager, K. Klaushofer, P. Wobraschek, J. G. Hofstaetter, P. Roschger, and

- C. Streli, “Increased zinc accumulation in mineralized osteosarcoma tissue measured by confocal synchrotron radiation micro x-ray fluorescence analysis”, *X-Ray Spectrometry*, vol. 46, no. 1, p. 56–62, 2017.
- [65] S. Savage and L. Mirabello, “Using epidemiology and genomics to understand osteosarcoma etiology”, *Sarcoma*, 2011.
- [66] M. Kansara, M. W. Teng, M. J. Smyth, and D. M. Thomas, “Translational biology of osteosarcoma.”, *Nat. Rev. Cancer*, vol. 14, p. 722–35, 2014.
- [67] A. Sakamoto and Y. Iwamoto, “Current status and perspectives regarding the treatment of osteo-sarcoma: chemotherapy.”, *Rev. Recent Clin. Trials*, vol. 3, p. 228–31, 2008.
- [68] A. Luetke, P. A. Meyers, I. Lewis, and H. Juergens, “Osteosarcoma treatment - where do we stand? A state of the art review.”, *Cancer Treat. Rev.*, vol. 40, p. 523–32, 2014.
- [69] J. Gumulec, M. Masarik, V. Adam, T. Eckschlager, I. Provaznik, and R. Kizek, “Serum and tissue zinc in epithelial malignancies: a meta-analysis.”, *PLoS One*, vol. 9, p. e99790, 2014.
- [70] A. Hashimoto and T. Kambe, “Mg, Zn and Cu Transport Proteins : A Brief Overview from Physiological and Molecular Perspectives (Nutrition and Food for Longevity : For the Well-Being of All : Proceedings of the 12th Asian Congress of Nutrition)”, *J. Nutr. Sci. Vitaminol. (Tokyo)*., vol. 61, p. S116–118, 2015.
- [71] D. Riesop, A. V. Hirner, P. Rusch, and A. Bankfalvi, “Zinc distribution within breast cancer tissue: A possible marker for histological grading?”, *J. Cancer Res. Clin. Oncol.*, vol. 141, p. 1321–31, 2015.
- [72] H. Tashiro, T. Kawamoto, T. Okubo, and O. Koide, “Variation in the distribution of trace elements in hepatoma.”, *Biol. Trace Elem. Res.*, vol. 95, p. 49–63, 2003.
- [73] K. Garber, “Targeting copper to treat breast cancer”, *Science*, vol. 349, no. 6244, p. 128–129, 2015.

- [74] A. Al-Ebraheem, M. J. Farquharson, and E. Ryan, “The evaluation of biologically important trace metals in liver, kidney and breast tissue.”, *Appl. Radiat. Isot.*, vol. 67, p. 470–4, 2009.
- [75] S. Ferrari and M. Serra, “An update on chemotherapy for osteosarcoma”, 2015.
- [76] M. Salzer-Kuntschik, G. Dellling, G. Beron, and R. Sigmund, “Morphological grades of regression in osteosarcoma after polychemotherapy - study COSS 80.”, *J. Cancer Res. Clin. Oncol.*, vol. 106 Suppl, p. 21–4, 1983.
- [77] J. G. Hofstaetter, A. Roschger, S. E. Puchner, M. Dominkus, I. Sulzbacher, R. Windhager, K. Klaushofer, and P. Roschger, “Altered matrix mineralization in a case of a sclerosing osteosarcoma.”, *Bone*, vol. 53, p. 409–13, 2013.
- [78] K. J. Millman and M. Aivazis, “Python for Scientists and Engineers”, *Comput. Sci. Eng.*, vol. 13, p. 9–12, 2011.
- [79] S. van der Walt, S. C. Colbert, and G. Varoquaux, “The NumPy Array: A Structure for Efficient Numerical Computation”, *Comput. Sci. Eng.*, vol. 13, p. 22–30, 2011.
- [80] E. Jones, T. Oliphant, P. Peterson, *et al.*, “SciPy: Open source scientific tools for Python”, 2001–. [Online; accessed 2018-06-24].
- [81] J. D. Hunter, “Matplotlib: A 2D Graphics Environment”, *Comput. Sci. Eng.*, vol. 9, p. 90–95, 2007.
- [82] C. A. Schneider, W. S. Rasband, and K. W. Eliceiri, “NIH Image to ImageJ: 25 years of image analysis”, *Nat. Methods*, vol. 9, p. 671–675, 2012.
- [83] R. L. McCornack, “Extended Tables of the Wilcoxon Matched Pair Signed Rank Statistic”, *J. Am. Stat. Assoc.*, vol. 60, p. 864–871, 1965.
- [84] J. H. Laity, B. M. Lee, and P. E. Wright, “Zinc finger proteins: new insights into structural and functional diversity”, *Curr. Opin. Struct. Biol.*, vol. 11, p. 39–46, 2001.

- [85] J. E. Coleman, “Structure and mechanism of alkaline phosphatase.”, *Annu. Rev. Biophys. Biomol. Struct.*, vol. 21, p. 441–83, 1992.
- [86] S. M. Krane and M. Inada, “Matrix metalloproteinases and bone.”, *Bone*, vol. 43, p. 7–18, 2008.
- [87] R. Lappalainen, M. Knuuttila, S. Lammi, E. M. Alhava, and H. Olkkonen, “Zn and Cu Content in Human Cancellous Bone”, *Acta Orthop. Scand.*, vol. 53, p. 51–55, 1982.
- [88] Y. Tang, H. F. Chappell, M. T. Dove, R. J. Reeder, and Y. J. Lee, “Zinc incorporation into hydroxylapatite.”, *Biomaterials*, vol. 30, p. 2864–72, 2009.
- [89] K. Matsunaga, H. Murata, T. Mizoguchi, and A. Nakahira, “Mechanism of incorporation of zinc into hydroxyapatite.”, *Acta Biomater.*, vol. 6, p. 2289–93, 2010.
- [90] M. Uhl, U. Saueressig, G. Koehler, U. Kontny, C. Niemeyer, W. Reichardt, K. Ilyasof, T. Bley, and M. Langer, “Evaluation of tumour necrosis during chemotherapy with diffusion-weighted MR imaging: preliminary results in osteosarcomas.”, *Pediatr. Radiol.*, vol. 36, p. 1306–11, 2006.
- [91] J. Ambroszkiewicz, J. Gajewska, T. Klepacka, M. Chęłchowska, T. Laskowska-Klita, and W. Woźniak, “Clinical utility of biochemical bone turnover markers in children and adolescents with osteosarcoma”, *Adv. Med. Sci.*, vol. 55, no. 2, p. 266–272, 2010.
- [92] F. W. Bonner, L. J. King, and D. V. Parke, “Cadmium-induced reduction of bone alkaline phosphatase and its prevention by zinc”, *Chem. Biol. Interact.*, vol. 29, p. 369–372, 1980.
- [93] D. Breiter, R. Diasio, J. Neifeld, M. Roush, and S. Rosenberg, “Serum copper and zinc measurements in patients with osteogenic sarcoma”, *Cancer*, vol. 42, no. 2, p. 598–602, 1978.
- [94] C. Davidson-Pilon, J. Kalderstam, B. Kuhn, P. Zivich, A. Fiore-Gartland, L. Moneda, A. Parij, K. Stark, S. Anton, L. Besson, Jona, H. Gadgil, D. Golland, S. Hussey, J. Noorbakhsh, A. Klintberg, N. Evans, M. Braymer-Hayes,

- Lukasz, J. Séguin, J. Rose, I. Slavitt, E. Martin, E. Ochoa, D. Albrecht, dhuyinh, D. Zgonjanin, D. Chen, C. Fournier, and A. F. Rendeiro, “Camdavidsonpilon/lifelines: v0.14.6”, 2018.
- [95] W. H. Press and S. A. Teukolsky, “Savitzky-golay smoothing filters”, *Computers in Physics*, vol. 4, no. 6, p. 669–672, 1990.
- [96] A. Savitzky and M. J. E. Golay, “Smoothing and differentiation of data by simplified least squares procedures.”, *Analytical Chemistry*, vol. 36, no. 8, p. 1627–1639, 1964.
- [97] M. Pajek, A. Kubala-Kukuś, D. Banaś, J. Braziewicz, and U. Majewska, “Random left-censoring: a statistical approach accounting for detection limits in x-ray fluorescence analysis”, *X-Ray Spectrometry: An International Journal*, vol. 33, no. 4, p. 306–311, 2004.
- [98] L. J. A. Stalpers and E. L. Kaplan, “Edward l. kaplan and the kaplan-meier survival curve”, *BSHM Bulletin: Journal of the British Society for the History of Mathematics*, vol. 33, no. 2, p. 109–135, 2018.
- [99] E. L. Kaplan and P. Meier, “Nonparametric estimation from incomplete observations”, *Journal of the American statistical association*, vol. 53, no. 282, p. 457–481, 1958.
- [100] Y. Jiang, W.-b. Xia, X.-p. Xing, B. C. Silva, M. Li, O. Wang, H.-b. Zhang, F. Li, H.-l. Jing, D.-r. Zhong, J. Jin, P. Gao, L. Zhou, F. Qi, W. Yu, J. P. Bilezikian, and X.-w. Meng, “Tumor-induced osteomalacia: An important cause of adult-onset hypophosphatemic osteomalacia in china: Report of 39 cases and review of the literature”, *Journal of Bone and Mineral Research*, vol. 27, no. 9, p. 1967–1975, 2012.
- [101] M. K. Drezner, “Tumor-induced osteomalacia”, *Reviews in Endocrine and Metabolic disorders*, vol. 2, no. 2, p. 175–186, 2001.
- [102] C. Harinarayan, S. Gopal, C. Puttaswamygowda, K. P. Adnan, N. Ghosal, S. Roohi, A. Tandon, and P. GR, “Tumor-induced osteomalacia due to phosphaturic mesenchymal tumor, mixed cell type, of the sphenoid bone”, *AACE Clinical Case Reports*, vol. 2, no. 4, p. e290–e295, 2016.

- [103] F. Meirer, B. Pemmer, G. Peponi, N. Zoeger, P. Wobrauschek, S. Sprio, A. Tampieri, J. Goettlicher, R. Steininger, S. Mangold, P. Roschger, A. Berzlanovich, J. G. Hofstaetter, and C. Streli, “Assessment of chemical species of lead accumulated in tidemarks of human articular cartilage by X-ray absorption near-edge structure analysis”, *Journal of Synchrotron Radiation*, vol. 18, p. 238–244, 2011.
- [104] R. J. G. B. Campello, D. Moulavi, and J. Sander, “Density-based clustering based on hierarchical density estimates”, in *Advances in Knowledge Discovery and Data Mining* (J. Pei, V. S. Tseng, L. Cao, H. Motoda, and G. Xu, eds.), (Berlin, Heidelberg), p. 160–172, Springer Berlin Heidelberg, 2013.

Curriculum Vitæ

Employment

- 04/2015 - 05/2018 **Project Assistant (FWF)**, Atominstitut, TU Wien.
10/2013 - 09/2017 **Predoc Univ. Assistant**, Atominstitut, TU Wien.

Higher education

- since 09/2013 **Doctoral programme in Engineering Sciences: Technical Physics**, TU Wien.
10/2010 – 07/2013 **Technical Physics - Master's degree**, TU Wien.
2013 Master Thesis at the Atominstitut, TU Wien
10/2006 – 09/2010 **Technical Physics - Bachelor's degree**, TU Wien.

Additional Training

- 02/2016 **Training for radiation protection officers - sealed radioactive sources and industrial X-ray equipment**, Seibersdorf Laboratories - Seibersdorf Academy.
02/2015 **Basic training for radiation protection officers**, WIFI Wien.

International Experience

- since 2017 **Experiments at the European Synchrotron Radiation Facility (ESRF)**, Grenoble, FR.
since 2016 **Experiments at Synchrotron Radiation Facility ELETTRA**, Trieste, IT.
since 2016 **Experiments at Synchrotron Radiation Facility DIAMOND**, Oxfordshire, GB.
since 2015 **Experiments at Synchrotron Radiation Facility BESSY II**, Berlin, DE.
2012-2014 **Experiments at Synchrotron Radiation Facility ANKA**, Eggenstein-Leopoldshafen, DE.

Awards

- 02/2017 Award for the talk presented at the 26th Seminar Activation Analysis and Gamma Spectroscopy
08/2015, 08/2017 Best XRF Poster Award at the Annual Denver X-ray Conference

Memberships

- since 2015 ÖPG (Austrian Physical Society)

Scientific Community

- since 2017 Reviewer for Food Analytical Methods (Online ISSN: 1936-976X)
- since 2017 Vice-President of the committee „ÖPG Young Minds“ of both the Austrian physical society and the European physical society Young minds Project
- since 2016 Member of the the works council of the academic university personnel
- since 2016 Reviewer for X-ray Spectrometry (Online ISSN: 1097-4539)
- since 2016 Substitute member of the “Fakultätsrat” (advisory board to the dean of physics)
- 09/2016 - 02/2017 Member of the organizing team of the 26th Seminar Activation Analysis and Gamma Spectroscopy (a conference held in Vienna, Austria in February 2017)
- 2015 - 2016 Secretary of the committee „ÖPG Young Minds“ of both the Austrian physical society and the European physical society Young minds Project

Teaching

- since 2016 **Co-supervision of two master thesis** (A. Winkler, T. Bretschneider)
- since 2016 **Practical Course in X-Ray Analytical Methods**
- since 2015 **Methods and applications of radiation physics**
- 2015 - 2016 **Numerical exercises to physics lecture 1**
- since 2014 **Project Work in Electron- and X-Ray Physics** to date 9 students supervised

Outreach activities

- 04/2018 **Töchtertag 2018** - TU Wien, Atominstitut
Outreach program for female students aged between 11 and 16
- 03/2018 **Physik im Beisl**
Organization of physics talks in a pub (Stattbeisl, WUK) for the general public by the Young Minds section of the Austrian Physical Society (ÖPG)
- 09/2017 **LehrerInnentag 2017 der Österreichischen Physikalischen Gesellschaft**
Outreach program for students organized by the sections Young Minds and Physik & Schule (physics and school) of the Austrian Physical Society (ÖPG)
- 02/2017 **FIT 2017 - Frauen in die Technik**: TU Wien, Atominstitut
Outreach program for female students aged between 16 and 19
- 09/2016 **Young-Minds-Session during the ÖPG conference**
Outreach program for students organized by the Young Minds section of the Austrian Physical Society (ÖPG)
- 01/2016 **FIT 2016 - Frauen in die Technik**: TU Wien, Atominstitut
Outreach program for female students aged between 16 and 19
- 07/2014 **KinderuniWien 2014: TechNIKE** - Ein Mikroskop zum Selberbauen
Building microscopes with children aged between 7 and 12 in the scope of an outreach program of Viennese Universities

Publications

Articles in Peer-reviewed Scientific Journals

-
- 2018 A. Maderitsch, D. Ingerle, T. Bretschneider, M. Rauwolf, C. Pflumm, H. Buchholz, H. Borchert, C. Streli, J. Parisi: **Analysis of organic multilayer structures using a combined grazing incidence X-ray fluorescence/X-ray reflectometry approach**, Spectrochimica Acta Part B: Atomic Spectroscopy, accepted, <https://doi.org/10.1016/j.sab.2018.07.006>.
- 2018 M. Rauwolf, A. Turyanskaya, D. Ingerle, N. Szoboszlai, I. Pape, A.W. Malandain, O.J.L. Fox, L. Hahn, K.J.S. Sawhney and C. Streli: **Characterization of a submicro-XRF setup on the B16 beamline at the Diamond Light Source**, J. Synchrotron Rad. 25, <https://doi.org/10.1107/S1600577518006203>
- 2018 L. Perneczky, M. Rauwolf, D. Ingerle, D. Eichert, F. Brigidi, W. Jark, S. Bjeoumikhova, G. Pepponi, P. Wobrauschek, C. Streli and A. Turyanskaya: **Temporary implementation and testing of a confocal SR- μ XRF system for bone analysis at the X-Ray Fluorescence beamline at Elettra**, Nucl. Instrum. Methods A, 897, p. 114-119, <https://doi.org/10.1016/j.nima.2018.04.012>
- 2017 M. Rauwolf, B. Pemmer, A. Roschger, A. Turyanskaya, S. Smolek, A. Maderitsch, P. Hischenhuber, M. Foelser, R. Simon, S. Lang, S.E. Puchner, R. Windhager, K. Klaushofer, P. Wobrauschek, J.G. Hofstaetter, P. Roschger and C. Streli: **Increased zinc accumulation in mineralized osteosarcoma tissue measured by confocal synchrotron radiation micro X-ray fluorescence analysis**, X-ray Spectrometry, 46(1), p. 56-62, doi: 10.1002/xrs.2727
- 2017 M. Rauwolf, A. Turyanskaya, A. Roschger, J. Prost, R. Simon, O. Scharf, M. Radtke, T. Schoonjans, A. Guilherme Buzanich, K. Klaushofer, P. Wobrauschek, J. G. Hofstaetter, P. Roschger and C. Streli: **Synchrotron radiation micro X-ray fluorescence spectroscopy of thin structures in bone samples: comparison of confocal and color X-ray camera setups**, J. Synchrotron Rad., 24, p. 307-311, doi: 10.1107/S1600577516017057
- 2016 A. Turyanskaya, M. Rauwolf, T. A. Grünewald, M. Meischel, S. Stanzl-Tschegg, J. F. Löffler, P. Wobrauschek, A. M. Weinberg, H. C. Lichtenegger and C. Streli: **μ XRF Elemental Mapping of Bioresorbable Magnesium-Based Implants in Bone**, Materials, 9(10), 811, doi: 10.3390/ma9100811
- 2016 L. Borgese, F. Bilo, A. Zacco, E. Bontempi, M. Pasquali, S. Federici, J. Prost, M. Rauwolf, A. Turyanskaya, C. Streli, P. Kregsamer, P. Wobrauschek and L. E. Depero: **(Invited) ALD to Prevent Metal Transfer from Implants**, ECS Trans., volume 75, issue 6, p. 167 - 175, doi: 10.1149/07506.0167ecst

- 2015 F. Bilo, L. Borgese, J. Prost, M. Rauwolf, A. Turyanskaya, P. Wobrauschek, P. Kregsamer, C. Strelì, U. Pazzaglia and L. Depero: **Atomic layer deposition to prevent metal transfer from implants: an X-Ray Fluorescence study**, Applied Surface Science, 359, p. 215 - 220, doi: 10.1016/j.apsusc.2015.09.248
- 2014 M. Rauwolf, C. Vanhoof, K. Tirez, E. Maes, D. Ingerle, P. Wobrauschek and C. Strelì: **Total Reflection X-Ray Fluorescence Measurements of S and P in proteins using a vacuum chamber specially designed for low Z elements**, Spectrochim Acta B: Atomic Spectroscopy, 101, p. 118 - 122. doi: 10.1016/j.sab.2014.07.022
- 2014 N. L. Misra, B. Kanrar, S. K. Aggarwal, P. Wobrauschek, M. Rauwolf and C. Strelì: **A comparative study on total reflection X-ray fluorescence determination of low atomic number elements in air, helium and vacuum atmospheres using different excitation sources**, Spectrochim Acta B: Atomic Spectroscopy, 99, p. 129-132. doi: 10.1016/j.sab.2014.06.011

Academic Thesis

- 2013 M. Rauwolf
Bestimmung von Phosphor und Schwefel in Proteinen mit low Z Totalreflexionsröntgen-fluoreszenzanalyse
Master Thesis, Atominstitut, TU Wien

Conference contributions

Talks

- 2017 M. Rauwolf, B. Pemmer, A. Roschger, A. Turyanskaya, S. Smolek, A. Maderitsch, P. Hischenhuber, R. Simon, S. Lang, S. E. Puchner, R. Windhager, K. Klaushofer, J. G. Hofstaetter, P. Roschger and C. Strel: **Synchrotron Radiation Micro XRF Analysis of Zinc in Osteosarcoma Tissue**, Jahrestagung FG Nuklearchemie, GDCh Scientific Forum Chemistry 2017, Berlin, Germany, **Invited**
- 2017 M. Rauwolf, A. Turyanskaya, A. Roschger, I. Pape, K. Sawhney, P. Wobrauschek, P. Roschger, J.G. Hofstaetter and C. Strel: **Zinc (Zn) and Lead (Pb) Accumulation in the Tidemark of Articular Cartilage with High-resolution micro-XRF**, Annual Denver X-ray Conference 2017, Big Sky, USA
- 2017 A. Turyanskaya, M. Rauwolf, L. Perneczky, A. Svirikova, M. Bonta, A. Limbeck, M. Marchetti-Deschmann, A. Roschger, P. Roschger, P. Wobrauschek, C. Strel: **Multimodal Imaging of Biological Samples: Correlation of μ XRF with MALDI-MSI and with LA-ICP-MS**, Annual Denver X-ray Conference 2017, Big Sky, USA
- 2017 A. Turyanskaya, M. Rauwolf, P. Wobrauschek and C. Strel: **Elemental bioimaging in bone by μ XRF**, 16th International Symposium on Trace Elements in Man and Animal (TEMA-16), Saint Petersburg, Russia
- 2017 C. Strel, M. Rauwolf, A. Turyanskaya, B. Pemmer, D. Ingerle, P. Roschger, A. Roschger, J. Hofstätter and N. Szoboszlai: **Hard X-ray Spectroscopy of Biological Material using Synchrotron Radiation**, NESY winterschool (2017), Altaussee, Austria, **Invited**
- 2017 M. Rauwolf, B. Pemmer, A. Roschger, A. Turyanskaya, S. Smolek, A. Maderitsch, P. Hischenhuber, R. Simon, S. Lang, S. E. Puchner, R. Windhager, K. Klaushofer, J. G. Hofstaetter, P. Roschger and C. Strel: **Synchrotron radiation micro XRF analysis of zinc in osteosarcoma tissue**, 26th Seminar Activation Analysis and Gamma Spectroscopy, Vienna, Austria
- 2016 P. Wobrauschek, M. Rauwolf, A. Turyanskaya, J. Prost and C. Strel: **X-ray spectrometry with Synchrotron radiation**, Symposium: „Future Possible Use of Neutron and Synchrotron Sources by the Austrian User Community“, Graz, Austria
- 2016 A. Winkler, M. Rauwolf, A. Turyanskaya, J. Sterba, P. Wobrauschek and C. Strel: **Spurenelementanalyse mit Totalreflexionsröntgenfluoreszenz**, 66th Yearly Meeting of the Austrian Physical Society, Vienna, Austria

- 2016 M. Rauwolf, B. Pemmer, A. Roschger, A. Turyanskaya, S. Smolek, A. Maderitsch, P. Hischenhuber, C. Weixelbaumer, M. Foelser, R. Simon, S. Lang, S. E. Puchner, R. Windhager, K. Klaushofer, J. G. Hofstaetter, P. Roschger and C. Strelj: **Zinc accumulation in mineralized osteosarcoma tissue determined with confocal SR- μ XRF**, European Conference on X-ray Spectrometry (EXRS2016), Gothenburg, Sweden
- 2016 A. Turyanskaya, M. Rauwolf, A. Roschger, B. Pemmer, J. Prost, P. Hischenhuber, T. Landete-Castillejos, R. Simon, P. Wobrauschek, P. Roschger, J. G. Hofstaetter, T. Landete-Castillejos and C. Strelj: **Manganese distribution in antler and human bone by SR- μ XRF analysis**, European Conference on X-ray Spectrometry (EXRS2016), Gothenburg, Sweden
- 2015 M. Rauwolf, B. Pemmer, A. Roschger, A. Turyanskaya, R. Simon, R. Windhager, K. Klaushofer, J. G. Hofstaetter, P. Roschger and C. Strelj: **Distribution of Zinc in human high-grade osteosarcoma and healthy tissue determined with confocal synchrotron radiation micro X-ray Fluorescence analysis**, International Conference on Progress in Bone and Mineral Research 2015 and the Annual Autumn Conference of the Austrian Society for Bone and Mineral Research, Vienna, Austria
- 2015 A. Turyanskaya, M. Rauwolf, A. Roschger, B. Pemmer, J. Prost, R. Simon, P. Roschger, J. G. Hofstaetter, T. Landete-Castillejos and C. Strelj: **Synchrotron μ XRF analysis of Manganese distribution in antler and human bone**, International Conference on Progress in Bone and Mineral Research 2015 and the Annual Autumn Conference of the Austrian Society for Bone and Mineral Research, Vienna, Austria
- 2015 C. Strelj, P. Wobrauschek, D. Ingerle, M. Rauwolf and J. Prost: **Low Z TXRF**, Cooperation BARC, Mumbai, India
- 2015 C. Strelj, P. Wobrauschek, D. Ingerle, J. Prost, M. Rauwolf and A. Turyanskaya: **Synchrotron Radiation Induced X-ray spectrometry - special techniques and applications**, IAEA Technical Meeting on Developments in Instrumentation and Novel Techniques for X-Ray Spectrometry Applications (F1-TM-47480), IAEA Head Quarter, Vienna, Invited
- 2015 C. Strelj, M. Rauwolf, J. Prost, D. Ingerle and P. Wobrauschek: **TXRF of Low Z Elements: Developments and Applications - a review**, Keynote Lecture: TXRF 2015, Westminster, CO, USA
- 2013 B. Pemmer, S. Smolek, C. Weixelbaumer, M. Fölser, M. Rauwolf, A. Maderitsch, P. Wobrauschek, C. Strelj, A. Roschger, P. Roschger, K. Klaushofer, R. Simon, R. Windhager, S. Lang and J. Hofstätter: **Differential accumulation of S, Ca, Fe and Zn in human osteosarcoma tissue**, ICXOM 2013, Hamburg, Germany

- 2013 B. Pemmer, S. Smolek, C. Weixelbaumer, M. Fölser, M. Rauwolf, A. Maderitsch, P. Wobrauschek, C. Strelj, A. Roschger, P. Roschger, K. Klaushofer, R. Simon, R. Windhager, S. Lang and J. Hofstätter: **Distribution of S, Ca, Fe And Zn in Human Osteosarcoma Tissue Determined with Synchrotron and Laboratory μ XRF Analysis**, 8th European NESY Winter-School, Planneralp, Austria

Poster Presentations

- 2018 M. Rauwolf, A. Turyanskaya, D. Ingerle, N. Szoboszlai, I. Pape, A. W. Malandain, O. J. L. Fox, L. Hahn, K. Sawhney, and C. Strelj: **The submicro-X-ray fluorescence setup on the B16 beamline at Diamond Light Source**, Annual Denver X-ray Conference 2018, Westminster, Colorado, USA
- 2018 A. Turyanskaya, M. Rauwolf, V. Pichler, T. Grünwald, M. Burghammer, O. J. L. Fox, I. Pape, K. Sawhney, J.G. Hofstaetter, A. Roschger, P. Roschger, Peter Wobrauschek and C. Strelj: **Detection of Gadolinium accumulation in bone by XRF**, Annual Denver X-ray Conference 2018, Westminster, Colorado, USA
- 2018 M. Rauwolf, A. Turyanskaya, A. Roschger, I. Pape, K. Sawhney, P. Wobrauschek, P. Roschger, J. G. Hofstaetter, and C. Strelj: **Micro-XRF analysis of zinc and lead accumulation in the tide-mark of articular cartilage**, European Conference on X-Ray Spectrometry, Ljubljana, Slovenia
- 2018 A. Turyanskaya, M. Rauwolf, O.J.L. Fox, I. Pape, K. Sawhney, T. Grünwald, M. Burghammer, J.G. Hofstaetter, A. Roschger, P. Roschger, Peter Wobrauschek and C. Strelj: **Detection of Gadolinium accumulation in bone by XRF**, European Conference on X-Ray Spectrometry, Ljubljana, Slovenia
- 2017 A. Winkler, M. Rauwolf, A. Turyanskaya, J.H. Sterba and C. Strelj: **Trace elements analysis in tea and herbal infusions by means of TXRF**, 17th International Conference on Total Reflection X-Ray Fluorescence Analysis and Related Methods (TXRF2017), Brescia, Italy
- 2017 A. Maderitsch, D. Ingerle, M. Rauwolf, T. Bretschneider, C. Pflumm, H. Buchholz, H. Borchert, C. Strelj, J. Parisi: **Investigation of organic multilayer structures using a combined GIXRF/XRR approach**, 17th International Conference on Total Reflection X-Ray Fluorescence Analysis and Related Methods (TXRF2017), Brescia, Italy
- 2017 M. Rauwolf, A. Turyanskaya, A. Roschger, P. Wobrauschek, P. Roschger, J. G. Hofstaetter and C. Strelj: **Novel Clustering Approach for the Segmentation of Elemental Distributions in Human Bone**, Annual Denver X-ray Conference 2017, Big Sky, USA
- 2017 A. Turyanskaya, M. Rauwolf, T. Bretschneider, A. Roschger, J. G. Hofstaetter, P. Roschger, I. Zizak, P. Wobrauschek and C. Strelj: **Investigation of the Local Manganese Distribution in Bone in Female and Male Osteoporosis Compared to Healthy Controls**, Annual Denver X-ray Conference 2017, Big Sky, USA

- 2017 A. Turyanskaya, L. Perneczky, M. Rauwolf, D. Eichert, F. Brigidi, W. Jark, S. Bjeoumikhova, G. Pepponi, P. Roschger, P. Wobrauschek and C. Strel: **Implementation of a Confocal SR-microXRF System for Bone Analysis at the X-ray Fluorescence Beam Line at Elettra**, Annual Denver X-ray Conference 2017, Big Sky, USA
- 2017 A. Pejovic-Milic, D. Cardenas, A. Turyanskaya, M. Rauwolf, G. Wohl, C. Strel, P. Wobrauschek: **Elemental Mapping of Rat Bones Treated with Strontium Ranelate and Strontium Citrate using 2D μ XRF Imaging**, 16th International Symposium on Trace Elements in Man and Animal (TEMA-16), International Society for Trace Element Research in Humans (ISTERH 2017), Saint Petersburg, Russia
- 2017 A. Winkler, M. Rauwolf, A. Turyanskaya, J. Sterba and C. Strel: **Total X-ray reflection fluorescence spectrometry of black tea and herbal infusions**, 26th Seminar Activation Analysis and Gamma Spectroscopy, Vienna, Austria
- 2017 A. Turyanskaya, M. Rauwolf, L. Perneczky, T. A. Gruenewald, M. Meischel, H. C. Lichtenegger, S. E. Stanzl-Tschegg, A. M. Weinberg, P. Wobrauschek and C. Strel: **μ XRF spectrometer at Atomintitut for bio-imaging applications**, 26th Seminar Activation Analysis and Gamma Spectroscopy, Vienna, Austria
- 2017 T. Bretschneider, M. Rauwolf, P. Wobrauschek and C. Strel: **TXRF Messungen leichter Elemente mit einem neuen SDD Detektor**, 26th Seminar Activation Analysis and Gamma Spectroscopy, Vienna, Austria
- 2017 L. Perneczky, A. Turyanskaya, S. Smolek, M. Rauwolf, P. Wobrauschek and C. Strel: **Confocal μ XRF spectrometer for low to high Z element analysis**, 26th Seminar Activation Analysis and Gamma Spectroscopy, Vienna, Austria
- 2016 A. Winkler, M. Rauwolf, A. Turyanskaya, J. Sterba, P. Wobrauschek and C. Strel: **Total X-ray reflection fluorescence spectrometry analysis of trace elements in tea and herbal infusions**, 66th Yearly Meeting of the Austrian Physical Society, Vienna, Austria
- 2016 M. Rauwolf, B. Pemmer, A. Roschger, A. Turyanskaya, S. Smolek, A. Maderitsch, P. Hischenhuber, M. Foelser, R. Simon, S. Lang, S. E. Puchner, R. Windhager, K. Klaushofer, J. G. Hofstaetter, P. Roschger and C. Strel: **Confocal SR- μ XRF measurements of increased Zinc accumulation in mineralized osteosarcoma**, 66th Yearly Meeting of the Austrian Physical Society, Vienna, Austria
- 2016 L. Perneczky, A. Turyanskaya, S. Smolek, M. Rauwolf, P. Wobrauschek and C. Strel: **Confocal μ XRF spectrometer for analysis of 3-dimensional spatial distribution of low to high Z elements**, 66th Yearly Meeting of the Austrian Physical Society, Vienna, Austria

- 2016 M. Rauwolf, A. Turyanskaya, A. Roschger, J. Prost, R. Simon, I. Pape, M. Radtke, O. Scharf, T. Schoonjans, A. Guilherme Buzanich, K. Sawhney, P. Wobrauschek, P. Roschger, J.G. Hofstaetter and C. Strelt: **Zinc distribution in human bone: SR-micro X-ray fluorescence imaging of osteoporotic samples**, X-Ray Microscopy Conference (XRM2016), Oxford, UK
- 2016 A. Turyanskaya, M. Rauwolf, L. Perneczky, T.A. Gruenewald, M. Meischel, H. Lichtenegger, S.E. Stanzl-Tschegg, A.M. Weinberg, P. Wobrauschek and C. Strelt: **Exploitation of μ XRF spectrometer for Bio-Imaging**, X-Ray Microscopy Conference (XRM2016), Oxford, UK
- 2016 D. Ingerle, N. Szoboszlai, I. Papa, K. Sawhney, A. Turyanskaya, M. Rauwolf, and C. Strelt: **High resolution imaging of metal localization in cancer cells at the B16 beamline at Diamond**, X-Ray Microscopy Conference (XRM2016), Oxford, UK
- 2016 M. Rauwolf, B. Pemmer, A. Roschger, A. Turyanskaya, R. Simon, R. Windhager, K. Klaushofer, J. G. Hofstaetter, P. Roschger and C. Strelt: **Increased Zinc accumulation in mineralized osteosarcoma tissue measured by SR- μ XRF analysis**, 65nd Annual Denver X-ray Conference 2016, Chicago, USA
- 2016 M. Rauwolf, A. Turyanskaya, A. Roschger, B. Pemmer, J. Prost, R. Simon, I. Pape, K. Klaushofer, P. Wobrauschek, P. Roschger, J.G. Hofstaetter and C. Strelt: **Zn distribution in healing osteoporotic fractures measured by SR- μ XRF analysis**, 65nd Annual Denver X-ray Conference 2016, Chicago, USA
- 2016 A. Turyanskaya, T.A. Gruenewald, M. Meischel, M. Rauwolf, J. Prost, L. Perneczky, H. Lichtenegger, S.E. Stanzl-Tschegg, A.M. Weinberg, P. Wobrauschek and C. Strelt: **Elemental imaging on biodegradable orthopedic implants by μ XRF**, 65nd Annual Denver X-ray Conference 2016, Chicago, USA
- 2016 A. Turyanskaya, M. Rauwolf, A. Roschger, J. Prost, P. Hischenhuber, R. Simon, P. Roschger, J.G. Hofstaetter, K. Klaushofer, P. Wobrauschek, C. Strelt: **Manganese distribution in healthy and osteoporotic human bone**, 65nd Annual Denver X-ray Conference 2016, Chicago, USA
- 2016 A. Winkler, M. Rauwolf, A. Turyanskaya, J. Sterba and C. Strelt: **Total X-ray reflection spectrometry analysis of trace elements in tea and herbal infusions**, European Conference on X-ray Spectrometry (EXRS2016), Gothenburg, Sweden
- 2016 M. Rauwolf, A. Turyanskaya, A. Roschger, B. Pemmer, J. Prost, R. Simon, I. Pape, K. Sawhney, P. Wobrauschek, P. Roschger, J.G. Hofstaetter and C. Strelt: **SR- μ XRF analysis of the zinc distribution in healing osteoporotic fractures**, European Conference on X-ray Spectrometry (EXRS2016), Gothenburg, Sweden
- 2016 A. Turyanskaya, T.A. Gruenewald, M. Rauwolf, M. Meischel, J. Prost, L. Perneczky, H. Lichtenegger, S.E. Stanzl-Tschegg, A.M. Weinberg, P. Wobrauschek and C. Strelt: **Magnesium-based biodegradable orthopedic implants by μ XRF**, European Conference on X-ray Spectrometry (EXRS2016), Gothenburg, Sweden

- 2016 M. Rauwolf, B. Pemmer, A. Roschger, A. Turyanskaya, R. Simon, R. Windhager, K. Klaushofer, J. G. Hofstaetter, P. Roschger and C. Strelj: **Increased Zinc accumulation in mineralized osteosarcoma tissue**, 43rd Annual European Calcified Tissue Society Congress, Rom, Italy
- 2016 A. Turyanskaya, M. Rauwolf, A. Roschger, J. Prost, B. Pemmer, R. Simon, P. Roschger, J.G. Hofstaetter, T. Landete-Castillejos, P. Wobrauschek, C. Strelj: **Manganese distribution in bone tissue by SR- μ XRF**, 43rd Annual European Calcified Tissue Society Congress, Rom, Italy
- 2015 M. Rauwolf, A. Turyanskaya, A. Roschger, B. Pemmer, J. Prost, R. Simon, M. Radtke, T. Schoonjans, O. Scharf, A. Guilherme, P. Roschger, J.G. Hofstaetter, R. Windhager, K. Klaushofer, P. Wobrauschek and C. Strelj: **SR- μ XRF of bone samples - a comparison of a confocal and a CXC setup**, 64nd Annual Denver X-Ray Conference , Westminster, USA
- 2015 A. Turyanskaya, T.A. Gruenewald, M. Meischel, M. Rauwolf, J. Prost, H. Lichtenegger, S.E. Stanzl-Tschegg, A.M. Weinberg, P. Wobrauschek and C. Strelj: **Magnesium diffusion from implant into bone tissue observed by μ XRF imaging**, 64nd Annual Denver X-Ray Conference , Westminster, USA
- 2015 A. Turyanskaya, M. Rauwolf, A. Roschger, B. Pemmer, J. Prost, R. Simon, P. Roschger, J.G. Hofstaetter, T. Landete-Castillejos, K. Klaushofer, P. Wobrauschek and C. Strelj: **Spatially resolved manganese distribution in antler and human bone**, 64nd Annual Denver X-Ray Conference , Westminster, USA
- 2014 M. Rauwolf, B. Pemmer, D. Ingerle, P. Wobrauschek, C. Strelj and A. Pahlke: **Low Z TXRF measurements with a new SD detector with UTW**, EXRS 2014, Bologna, Italy
- 2014 M. Rauwolf, D. Ingerle, B. Pemmer, P. Wobrauschek and C. Strelj: **Low Z TXRF measurements with an SD detector with UTW**, 63nd Annual Denver X-Ray Conference , Montana, USA
- 2014 M. Rauwolf, C. Vanhoof, K. Tirez, P. Wobrauschek, D. Ingerle and C. Strelj: **TXRF measurements of S and P in proteins using a special TXRF vacuum chamber for low Z elements**, 63nd Annual Denver X-Ray Conference , Montana, USA
- 2013 M. Rauwolf, D. Ingerle, B. Pemmer, P. Wobrauschek and C. Strelj: **Low Z TXRF measurements with a new SDD detector**, 22nd International Congress on X-Ray Optics and Microanalysis (ICXOM), Hamburg, Deutschland
- 2013 M. Rauwolf, C. Vanhoof, K. Tirez, P. Wobrauschek, D. Ingerle and C. Strelj: **TXRF measurements of S and P in proteins using a special TXRF vacuum chamber for low Z elements**, 15th International Conference on Total Reflection X-Ray Fluorescence Analysis and Related Methods (TXRF2013), Osaka, Japan

- 2013 M. Rauwolf, D. Ingerle, B. Pemmer, P. Wobrauschek and C. Strelj: **Low Z TXRF measurements with an SDD detector with UTW**, 15th International Conference on Total Reflection X-Ray Fluorescence Analysis and Related Methods (TXRF2013), Osaka, Japan
- 2013 B. Pemmer, S. Smolek, C. Weixelbaumer, M. Fölser, M. Rauwolf, A. Maderitsch, P. Wobrauschek, C. Strelj, A. Roschger, P. Roschger, K. Klaushofer, R. Simon, R. Windhager, S. Lang and J. Hofstätter: **Distribution of S, Ca, Fe and Zn in human osteosarcoma tissue determined with synchrotron and laboratory μ -XRF Analysis**, Denver X-Ray Conference 2013, Westminster, CO, USA